Universidade de Aveiro
2022

Departamento de Engenharia
de Materiais e Cerâmica

Miguel Amado Vieira

Membranas cerâmicas hidrotermicamente ativadas para separação de oxigénio

Hydrothermally-activated ceramic membranes for oxygen separation

Universidade de Aveiro
2022

Departamento de Engenharia de Materiais e Cerâmica

Miguel Amado Vieira

Membranas cerâmicas hidrotermicamente ativadas para separação de oxigénio

Hydrothermally-activated ceramic membranes for oxygen separation

Dissertação apresentada à Universidade de Aveiro para cumprimento dos requisitos necessários à obtenção do grau de Mestre em Engenharia de Materiais, realizada sob a orientação científica do Doutor Andrei Kavaleuski, Investigador Principal do Departamento de Engenharia de Materiais e Cerâmica da Universidade de Aveiro e co-orientação do Doutor Aleksey Yaremchenko, Investigador Principal do Departamento de Engenharia de Materiais e Cerâmica da Universidade de Aveiro.

o júri
presidente

Prof. Doutora Paula Maria Lousada Silveirinha Vilarinho
Professora Doutora da Universidade de Aveiro

Doutor Aliaksandr Shaula
Investigador do Centro de Tecnologia Mecânica e Automação da Universidade de Aveiro

Doutor Andrei Kavaleuski
Investigador Principal do Departamento de Engenharia de Materiais e Cerâmica, CICECO da Universidade de Aveiro

acknowledgements

I would like to give a big thanks to my supervisors Doctor Andrei Kavaleuski and Doctor Aleksey Yaremchenko, by the continous dedication and support during the realization of this work. To my lab coworkers - “thank you all” for taking the time to help me with the use of equipment, sharing of knowledge, stories, and cheerful moments. I would like to express my gratitude to all the people of Department of Materials and Ceramics Engineering. I appreciate the accessibility to use the equipment and data analysis.
I’m grateful to my parents that accompanied and supported me in this arduous cycle and allowed me to have an academic degree.

keywords

SF7SA3, Perovskites, Oxygen nonstoichiometry, Hydrothermal activation, Activation layers, Praseodymium oxide, Oxygen permeation studies.

summary

The present work focuses on new strategies of the surface activation of ceramic membranes for oxygen separation involving hydrothermal processing. Such an approach is particularly relevant for membranes with complex shapes, for which the deposition of the surface activating agent by conventional methods might be complicated or even impossible. A model membrane material, $(SrFe)_{0.7}(SrAl_2)_{0.3}O_z$, consisting of two phases, the strontium-deficient perovskite $Sr(Fe,Al)O_{3-\delta}$ responsible for the ionic transport properties and the monoclinic $SrAl_2O_4$ phase responsible for adequate thermomechanical properties, was considered. The hydrothermal treatment was based on several top-down type and bottom-up type approaches, leading to controlled modification of the membrane surface. Following oxygen permeation studies under relevant operating conditions have shown that a significant enhancement of the oxygen flux through modified membranes can be achieved, providing a convincing proof-of-concept of the proposed strategies.

palavras-chave

SF7SA3, Perovskites, Não-estequiometria de oxigénio, Ativação Hidrotermal, Camadas de ativação, Óxido de Praseodímio, Estudos de permeação de oxigénio.

resumo

O presente trabalho foca-se em novas estratégias de ativação superficial em membranas cerâmicas para separação de oxigénio usando o processo hidrotermal. Esta abordagem é particularmente relevante para as membranas com geometrias complexas, no qual a deposição do agente ativador da superfície por métodos convencionais pode ser complicada ou mesmo impossível. O material modelo para a membrana, $(SrFe)_{0.7}(SrAl_2)_{0.3}O_z$, constituído por duas fases, a perovskita com deficiência de estrôncio $Sr(Fe,Al)O_{3-\delta}$ responsável pelas propriedades de transporte iónico e a fase monoclínica $SrAl_2O_4$ responsável por propriedades termomecânicas adequadas, foi considerado. O processo hidrotermal foi baseado em várias "top-down" e "bottom-up" abordagens, conduzidas a uma modificação controlada da superfície da membrana. Estudos de permeação de oxigénio sob condições operacionais mostraram que um aumento significativo do fluxo de oxigénio através das membranas modificadas pode ser alcançado, fornecendo uma prova de conceito convincente das estratégias propostas.

Index

Figure Index

Table Index

List of Abbreviations

	Name
BSCF	$Ba_{0.5}Sr_{0.5}Co_{0.8}Fe_{0.2}O_{3-\delta}$
CAC	Crude Argon Column
DC	Direct Current
EDS	Energy-Dispersive Spectroscopy
FCC	Face-Centered Cubic
HPC	High Pressure Column
ICDD	International Center for Diffraction Data
IP	Isostatic Pressure
LPC	Low Pressure Column
M	Molarity
MIEC	Mixed Ionic-Electronic Conducting
SEM	Scanning Electron Microscopy
SF7SA3	$(SrFe)_{0.7}(SrAl_2)_{0.3}O_y$ - $(0.7\ SrFeO_{3-\delta} \times 0.3\ SrAl_2O_4)$
SFA10	$SrFe_{0.9}Al_{0.1}O_y$
SFA30	$SrFe_{0.7}Al_{0.3}O_y$
TEC	Thermal Expansion Coefficient
SCF	$SrCo_{0.8}Fe_{0.2}O_{3-\delta}$
XRD	X-ray powder Diffraction
YSZ	Yttria-Stabilized Zirconia

List of Symbols

	Name	Unit
A	Cross-section area of the sample	cm^2
A_o	Pre-exponential factor	1/s
C_o	Volume concentration of oxygen anions	mol/cm^3
d	Distance between atomic planes	cm
D_s	Chemical diffusion coefficient of oxygen vacancies	cm^2/s
E_a	Activation energy	kJ/mol
e^-	Electron	-
F	Faraday's constant	C/ mol
$h^\bullet$	Electronic hole	-
$J_{ex}{}^o$	Surface exchange rate	mol $O_2/cm^2 \times s$
Jo_2	Oxygen permeation flux	$mol/cm^2 \times s$
k_s	Oxygen surface exchange coefficient	cm/s
L	Membrane thickness	cm
L_i	Distance between the inner electrodes	cm
L_c	Characteristic thickness of the membrane	cm
m	Mass	g
n	Diffraction order	-
$O_{(adsorbed)}$	Adsorbed oxygen	-
O_O^x	Oxygen ions occupying the oxygen lattice	-
Po_2	Oxygen partial pressure	Pa
$P'o_2$	Partial pressure of oxygen on the oxygen-rich side	Pa
$P''o_2$	Partial pressure of oxygen on the oxygen-lean side	Pa
ρ	Density	g/cm^3
R	Gas constant	J/mol K
R_t	Resistance	Ω
r_A	Ionic radius of the A cation	Å
r_B	Ionic radius of the B cation	Å
r_O	Radius of oxygen ions	Å
t	Tolerance factor	-
t_{el}	Oxygen electronic transfer number	-
t_{ion}	Oxygen ionic transfer number	-
$V_{cylinder}$	Volume of cylinder	cm^3
V_m	Perovskite molar volume	cm^3/mol
$V_O^{\bullet\bullet}$	Oxygen vacancies	-
Z_O^2	Valence charge of the oxygen anions	-
$\Delta\mu_{O_2}^{surf}$	Chemical potential gradient of oxygen through the surfaces of the membrane	J/mol
$\Delta\mu_{O_2}^{bulk}$	Chemical potential gradient of oxygen through the bulk of the membrane	J/mol
$\Delta\mu_{O_2}^{total}$	Chemical potential gradient of oxygen between both atmospheres	J/mol
δ	Oxygen nonstoichiometric constant	-
θ	Bragg's angle	°

λ	Incident radiation wavelength	Å
σ	Electrical conductivity	S/cm
σ_{ε}	Electronic conductivity	S/cm
σ_{i}	Oxygen ionic conductivity	S/cm
σ_{total}	Total conductivity	S/cm

1. Introduction

1. Introduction.

1.1. Evolution of oxygen separation technologies.

Oxygen is one of the main chemicals used in large quantities, indispensable in industrial processes, such as power generation and chemical industry. Production of pure oxygen is not an easy task, making this a large industry, where about 100 million tons of oxygen are produced each year. [1]

The most common and widespread processes to separate oxygen from air are the cryogenic process and the pressure swing adsorption method. However, they are not flawless and present some energetical downsides. The cryogenic process can be used only at a large industrial scale due to the need for operation at high pressures and low temperatures. This implies quite high production energy costs. While this process can produce oxygen with a purity of $\geq$99.5%, the pressure swing adsorption process is only able to reach oxygen purity of 90-95%, while being suitable for a small scale. [1][2]

In the cryogenic process, the first step is the filtration of air to remove dust particles, followed by compression and purification to remove contaminants such as carbon dioxide and water vapour. The purified air is then cooled to very low temperatures, promoting the liquefaction of the components. Oxygen and nitrogen have different boiling points and based on that the separation process will occur. The separation of air constituents takes place in a distillation column constituted by various sections with different pressures. [3][4]

A diagram of the cryogenic process of air is exemplified in Figure 1.

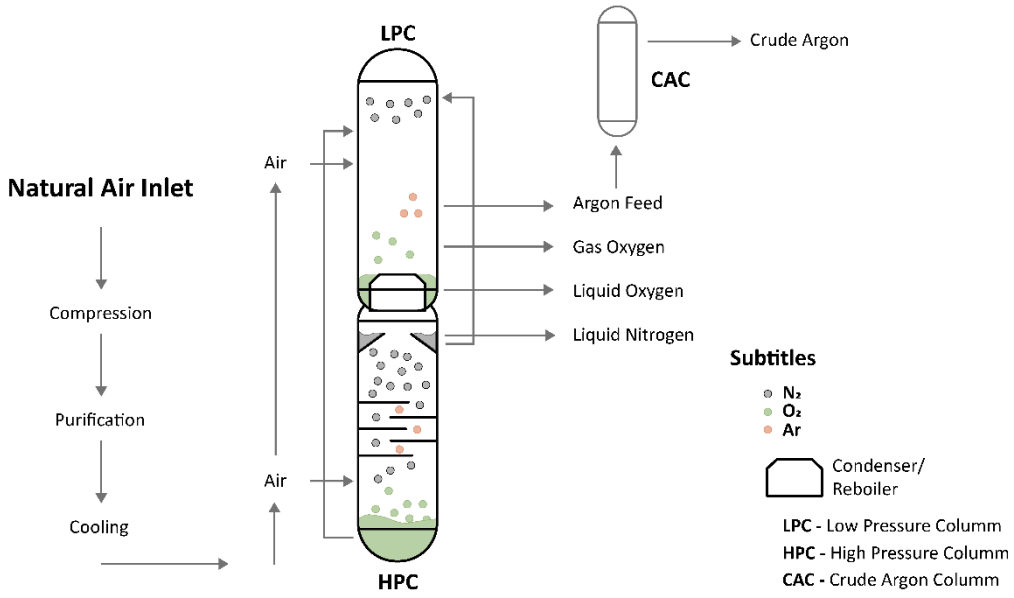

Figure 1 - Cryogenic air separation process. (Adapted from [4])

The facility includes a Low-Pressure Column, a High-Pressure Column, and a Crude Argon Column. Due to different boiling points of the components, liquid oxygen is placed in the bottom of the High-Pressure Column, where then it goes throw a heat exchanger and is introduced to the Low-Pressure Column for another distillation. A condenser-reboiler located between Low-Pressure Column and High-Pressure Column condenses the nitrogen from the High-Pressure Column and vaporizes the oxygen from the Low-Pressure Column. A part of this liquid nitrogen is introduced as reflux to the Low-Pressure Column. The oxygen is obtained in liquid form at the bottom of Low-Pressure Column and in gaseous form in the condenser/boiler, and the argon is separated in an additional column. [3][4]

The principles of pressure swing adsorption (PSA) process are described in Figure 2. The separation of oxygen from air is done by the compression of air under high pressure into molecular sieves adsorbers, where nitrogen will be selectively adsorbed in the pore structure of a zeolite, and consequently releasing the gas with a higher concentration of oxygen as a product gas. [2]

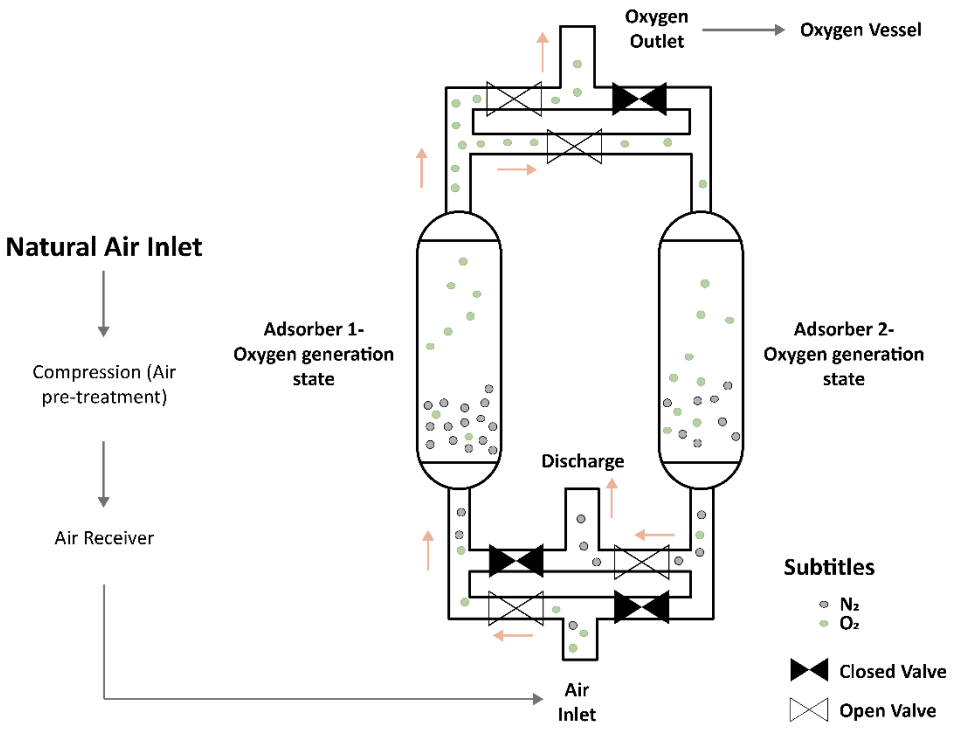

Figure 2 - Process flow diagram of the pressure swing adsorption process. (Adapted from [3])

When the adsorber reaches its full capacity, the process can be regenerated by reducing the pressure where desorption of the gas occurs from the adsorbent surface. In the meantime, the flow of air is directed to another chamber. This cycle can be repeated by the control of the pressure and a system of valves.

A relatively recent and increasingly attractive technique for the separation of oxygen from air is the dense ceramic membranes with mixed ionic-electronic conductivity (MIEC), which allows >99% of oxygen selectivity. Basically, in these membranes the oxygen is selectively transported through a membrane under a chemical driving force, and, in comparison to the processes mentioned above, it presents a viable economic potential, it is simpler and does not contribute to CO_2 emissions. [1]

These membranes can be applied in several industrial processes that require high purity of oxygen. This possibility of using pure oxygen in some processes instead of air, such as oxy-fuel combustion, consequently, allows the minimum prejudicial gas emissions, such as NO_x, due to the negligible content of nitrogen in the oxygen provided to the combustion. This use of oxygen allows a better process efficiency since the gaseous nitrogen is not present, and, consequently, the fuel consumption is reduced, which allows

a high flame temperature. This efficiency leads mainly to the formation of CO_2 and steam (H_2O), constituents of the flue gas, in which its possible to separate and store the CO_2 from the flue gas to use in chemical production. [1][2]

Also, the production of syngas is possible with these membranes if the supplied amount of oxygen does not permit the complete combustion of the fuel. In this case, the partial oxidation of methane occurs, forming the syngas. Syngas is usually used in chemical and fuel synthesis, like diesel and gasoline, and can be used to electricity generation. [1][5]

Table 1 demonstrates some particular advantages and disadvantages of the oxygen transport membranes compared to the other systems for oxygen separation.

Table 1 - Comparison of various processes for oxygen separation from air. [2]

Technique	Advantages	Disadvantages
Cryogenic Distillation	High purity of oxygen (99%)	Higher power consumption, capital cost and volume space than dense ceramic membranes
		Multiple stage separation process
		Lower efficiency comparable to dense ceramic membranes
Pressure Swing Adsorption	Efficient and not to expensive	Low purity of oxygen (90-95%)
		Not suitable for large scale applications
		Multiple stage separation process
Ceramic Dense Membranes	Lower power consumption, capital cost, and volume space than the cryogenic process	High temperatures needed for operation (>700°C)
	Efficient process with a high purity of oxygen (>99%)	Imperative to have chemical and mechanical stable materials to the reliable of the operation
	Single stage air separation process	

One of the main reasons driving the studies of MIEC membranes is the better integration possibility for these membranes in oxy-fuel combustion power plants or syngas generation facilities, due to the lower volume space and lower power consumption. However, the integration of these membrane in a wide commercial use is yet not possible, mainly due to their insufficient chemical stability in prospective operation conditions, leading to chemical expansion, stresses in the membrane and loss of the mechanical integrity. [2][6]

1.2. MIEC membrane concept.

1.2.1. General mechanism of oxygen transport.

Mixed ionic-electronic conducting (MIEC) membranes can effectively separate high purity oxygen (99.99%) from air at high temperatures (700-1000°C) and various pressures. This selective permeation is inherent to these dense ceramic membranes, provided by the diffusion of oxygen ions through the lattice vacancies or interstitial sites of the crystal structure. The driving force for this diffusion is a chemical potential gradient applied to the membrane, usually described as oxygen partial pressure difference between the feed and permeate side of the membrane. [5][7][8] Also this movement through the membrane involves an activation energy, which is the minimum amount of energy required to activate the molecules to initiate the flux across the membrane. This flux will be consequently dependent on the concentration of the molecules and the proportions of the activation energy to initiate the flux through the membrane.

As it follows from the name, simultaneous electronic and ionic transport occurs in the MIEC membranes, allowing them to operate without the need for additional electrodes or an external electrical source, making them especially attractive [5][7][9]. The oxygen transport mechanism through MIEC membranes involves several steps that are shown in Figure 3 and described below.

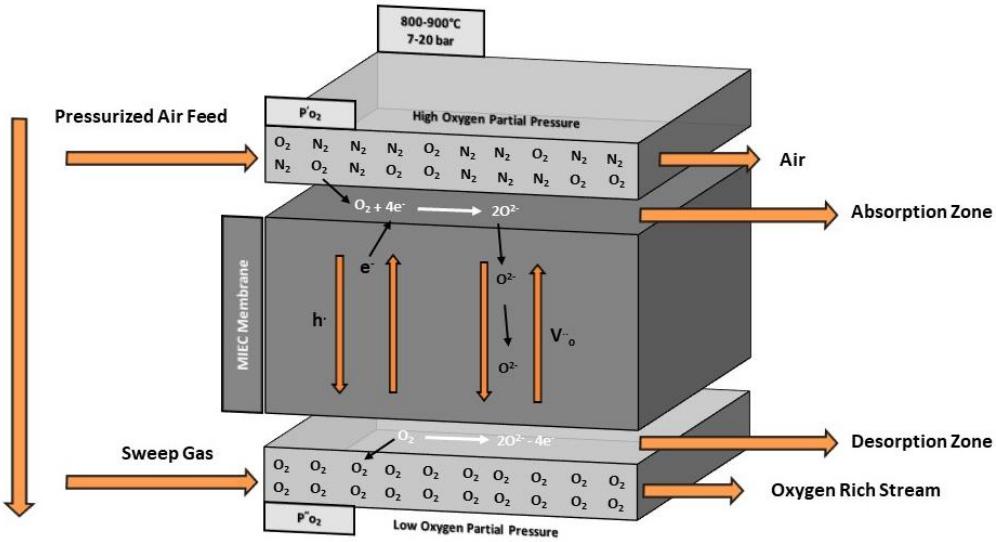

Figure 3 - Schematic representation of the associated steps in the permeation through MIEC dense ceramic membranes. (Adapted from [5][10])

In accordance with [1][2][10], these steps include:

(a) - O_2 diffusion from the feed side to the membrane surface.

(b) – Adsorption and surface exchange reaction: O_2 is adsorbed at the high oxygen pressure surface of the membrane and undergoes a reduction forming O^{2-}.

(Dissociation on high oxygen partial pressure side)

$$O_2 + 4e^- \rightarrow 2O^{2-} \quad (1)$$

(c) - Bulk Diffusion → The O^{2-} ions diffuse via the oxygen vacancies in the lattice due to the presence of the pressure gradient between both sides of the membrane. At the same time, electrons are carried in the opposite direction to compensate for the ionic flux, resulting in a conservation of electro-neutrality.

(d) – Surface exchange reaction and desorption: the O^{2-} ions on the low oxygen potential surface recombine to form oxygen molecules and desorb from the surface of the membrane.

(Recombination on low oxygen partial pressure side)

$$2O^{2-} \rightarrow O_2 + 4e^- \quad (2)$$

(e) - O_2 diffusion from the membrane surface to the permeate stream.

This oxygen transport mechanism through MIEC membranes occasionally can undergo a slight alteration if the membrane is not fully dense. The presence of closed pores in the dense membrane generates additional steps, such as an indirect pathway or the molecular gas diffusion through these pores, as is shown in Figure 4. [11]

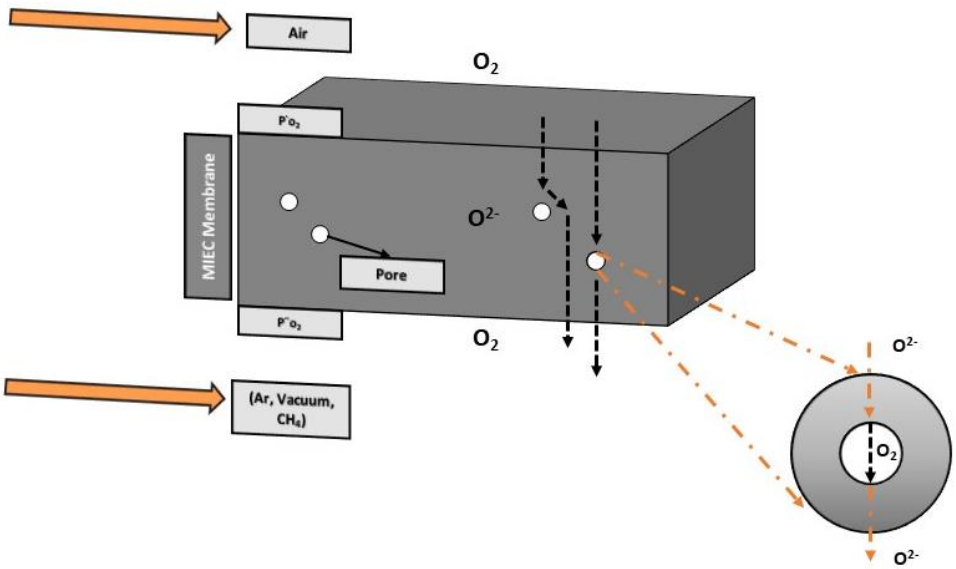

Figure 4 - Representation of bulk diffusion path of oxygen when the membrane presents closed pores. (Adapted from [12])

In fact, the appearance of such an additional mechanism might be even beneficial for oxygen transport through the membrane, especially for those based on materials with moderate or low oxygen-ionic conductivity. In this case, porosity decreases the effective membrane thickness, reducing the bulk diffusion limitations. The bulk ionic conductivity contribution to the overall oxygen permeation process and asymmetric concepts of the MIEC membranes, involving the porous layers, are discussed in the following sections.

1.2.2. Single-phase membranes.

The essential transport characteristics needed for MIEC membranes can be provided by single-phase materials or dual-phase composites. MIEC membranes constituted by one single phase are typically based on perovskites (ABO_3), fluorites (AO_2), brownmillerites ($A_2B_2O_5$), pyrochlores ($A_2B_2O_7$), and Ruddlesden-Popper series ($A_{n+1}B_nO_{3n+1}$). However, perovskites and fluorites families are the most researched, including various doping strategies, while the others structures still do not present sufficient performance. [12]

The oxygen permeation flux is directly related to the electronic and ionic conductivity. In a single-phase material (Figure 5), it is still challenging to achieve an appropriate level for both conductivities, simultaneously. Also, since relatively thin

membranes are required to provide a feasible oxygen flux, in a single-phase concept, it could be difficult to achieve the desired mechanical stability. [12]

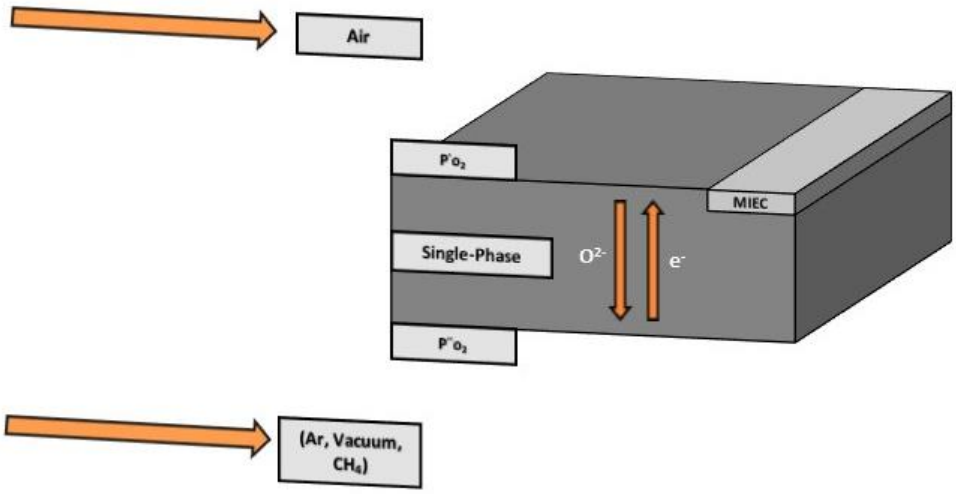

Figure 5 - Simplified scheme of a single-phase MIEC membrane.

The lack of sufficiently good oxygen permeation in single-phase materials forces the research to find out new possibilities. In particular, the composite materials containing both ionic and electronic conducting phases may present higher oxygen permeation, along with a better membrane thermal stability.

1.2.3. Dual-phase composite membranes.

These dual-phase composites can comprise two materials, each with its own goal. In particular, one may provide ionic conductivity and the other electronic conductivity, thus leading to an enhanced oxygen flux. Various composites can be considered, taking into account the conditions of structural and chemical stability, and the compatibility of the components at elevated temperatures. Generally a large variety of possible materials enable various membrane concepts, for example, a dispersion of a metallic phase in a ceramic phase or a ceramic phase in another ceramic phase. [10][11]

Figure 6 shows an illustrative representation of the microstructure and working principle on the dual-phase membranes.

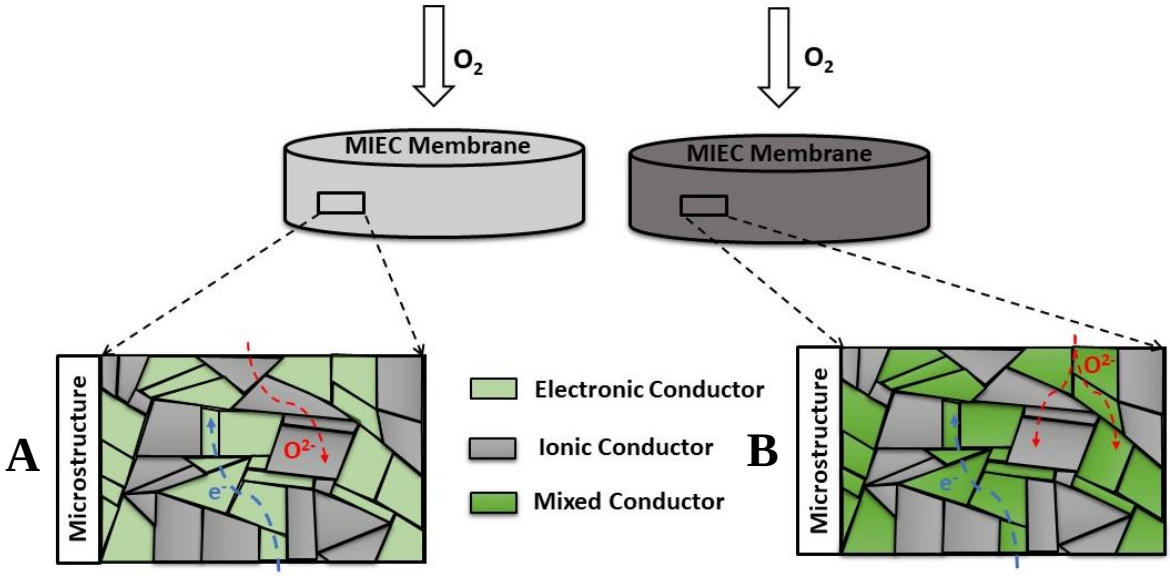

Figure 6 - Dual-phase membranes: (A) ionic-electronic conductor; (B) ionic-mixed conductor. (Adapted from [1])

In such structures, it is essential to optimize the ratio between both phases, so that each phase can be organized in a mixed continuous microstructure, providing a synchronized transport of oxygen ions and electrons. [7]

1.2.4. Pure ionic conductors.

In general, the MIEC membranes can be classified as passive or active, depending on the driving force for oxygen permeation process. [2] In active membranes, oxygen transport occurs due to the oxygen chemical potential difference between both sides. The passive membranes are those based on predominantly ionic conductors. When the membrane only presents the ionic conductivity, an external source and respective electrodes are needed to drive the oxygen ions and the electronic charge carriers. At the same time, such an approach gives better control of the amount of oxygen passing through the membrane. [2][12]

These types of membrane configurations (Figure 7) are usually used in oxygen pumps and fuel cell applications and present some difficulties regarding their use at a large scale due to significant electricity consumption. [12]

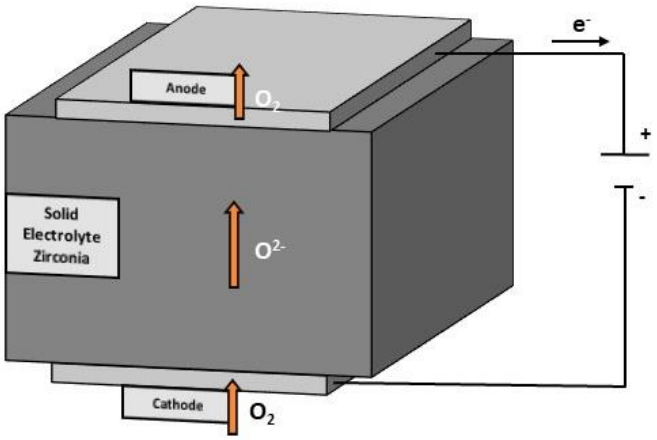

Figure 7 - The concept of an oxygen pump (electrolyte membrane). (Adapted from [13])

1.3. Factors affecting oxygen transport in MIEC membranes.

The rate of oxygen permeation through the membrane is affected by the surface exchange and bulk diffusion rates, membrane thickness, temperature, and the oxygen partial pressure gradient. While the bulk diffusion and surface exchange kinetics rely on the composition and microstructure of the membrane, the temperature and oxygen partial pressure gradient are determined by the operating conditions. [13][14] Consequently, the chosen materials and operating conditions, such as the oxygen partial pressure difference between the membrane sides, and employed gases, influence directly the performance of the membrane. [12]

Under given conditions (temperature, oxygen partial pressures), the oxygen transport through the membrane is limited either by bulk diffusion or surface exchange kinetics or by both factors.

These oxygen transport stages are interconnected (Figure 8), and sometimes it is difficult to separately identify their contributions, given that the slowest step is responsible for the rate of oxygen transport through the membrane. [14]

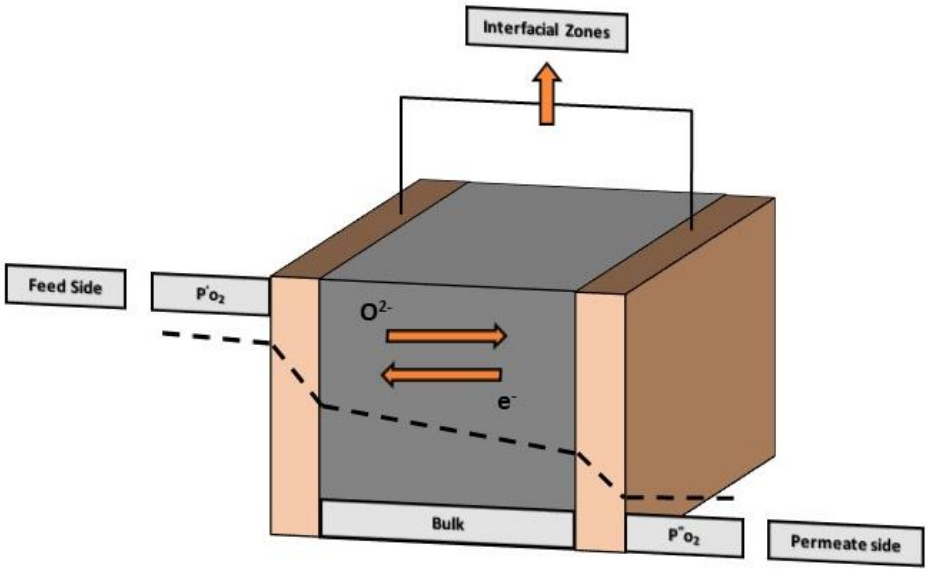

Figure 8 - Representation of the different steps during oxygen permeation through a MIEC membrane. (Adapted from [16])

1.3.1. Bulk diffusion.

The oxygen ions can move through the membrane via two different diffusion mechanisms: via the oxygen vacancies, usually taking place in ABO_3 perovskite oxides and fluorite oxides, and via the oxygen interstitial sites, as it happens in K_2NiF_4-type oxides. The latter presents a mixed diffusion mechanism involving both defects. [8]

Equation (3) describes the oxygen permeation across a MIEC membrane when the bulk diffusion controls the overall oxygen permeation, according to the Wagner model, assuming that the overall oxygen transport is not affected by the surface reactions at the interfaces of the membrane. [1][7][15][16]

$$J_{O_2} = \frac{R \times T}{16 \times F^2 \times L} \int_{P''(O_2)}^{P'(O_2)} \frac{\sigma_i \times \sigma_e}{\sigma_i + \sigma_e} \times \partial ln(PO_2) \qquad (3)$$

where J_{O_2} is the oxygen permeation flux, R is the gas constant, F is the Faraday's constant, T is the absolute temperature, L is the membrane thickness, σ_i is the oxygen ionic conductivity (S/m), σ_e is the electronic conductivity (S/m), $P'(O_2)$ and $P''(O_2)$ are the partial pressure of oxygen on the oxygen-rich side and on the oxygen-lean side, respectively. [7]

Assuming a perovskite structure, Figure 9 gives us an idea of how the bulk diffusion across the membrane occurs, namely, by a flux of oxygen ions O^{2-} hopping from an oxygen vacancy to the next. [1]

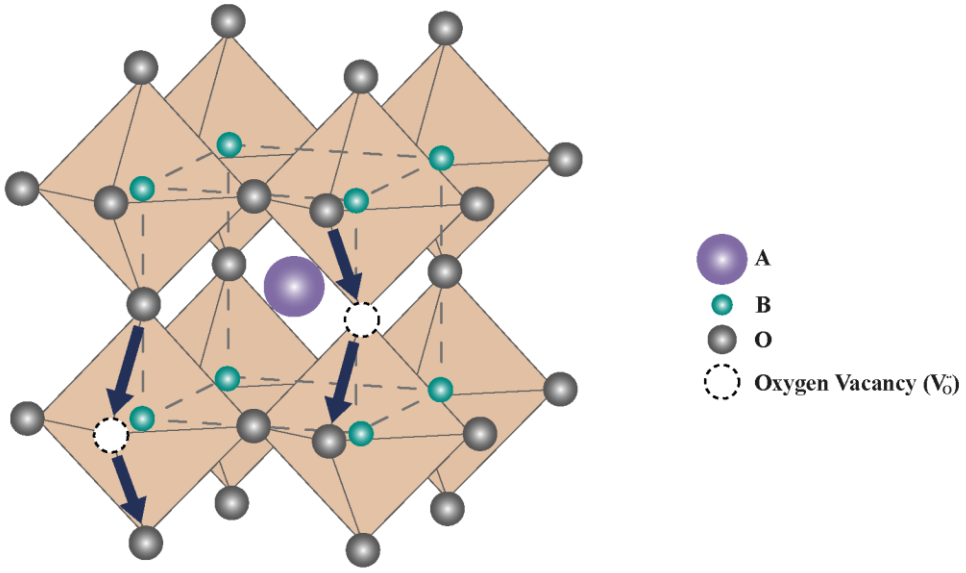

Figure 9 - Illustration of oxygen ionic conductivity mechanism in a perovskite structure. (Adapted from [1])

1.3.2. Surface oxygen exchange.

Contrarily to bulk diffusion, the general expression representing the oxygen kinetics at the membrane surface includes various parameters related to the mechanism of surface exchange reactions, as for example, the applied sweep gas (He, CH_4, CO_2, among others) that has a noticeable influence on this step. [1][12] Sometimes, more specific conditions must be considered for the surface exchange reactions, if, for example, the CO_2 is used as sweep gas, which can affect the absorption of O_2, on the membrane surface in different ways. [17]

In general, the oxygen flux limited by the surface exchange at the membrane surface, in conditions near to equilibrium, and taking in account the relation presented in Equation (4), can be described by the Onsager Equation (5): [1][18][19]

$$J_{ex^o} = ¼\, k_s \times C_o \quad (4)$$

$$J_{O_2} = J_{ex^o} \times \left(\frac{\Delta\mu_{O_2}^{surf}}{R \times T}\right) \quad (5)$$

where $\Delta\mu_{O_2}^{surf}$ is the oxygen chemical potential difference across the surface, and J_{ex^o}, represents the surface exchange rate in absence of the oxygen potential gradient. [1] The J_{ex^o} is dependent on the oxygen surface exchange coefficient, k_s, and C_o, the volume concentration of oxygen ions close to the surface of the membrane at equilibrium. [18][19]

The steps related to the surface exchange reactions take place at both sides of the membrane: at the feed side, prior to the bulk diffusion through the membrane, and at the permeate side, after the diffusion through the membrane bulk. These surface reactions include various processes like the adsorption and dissociation of O_2, so, the reactions in both sides of the membrane, in general, can be expressed in Equations (6) e (7). [10][16][20]

$$½\, O_2 \rightarrow O_{(adsorbed)}$$

$$O_{(adsorbed)} + 2e^- \rightarrow O^{2-}$$

$$O^{2-} + V_O^{\bullet\bullet} \rightarrow O_O^x$$

$$\Downarrow$$

$$\text{Feed Side: } ½\, O_2 + V_O^{\bullet\bullet} \rightarrow O_O^x + 2h^{\bullet\bullet} \quad (6)$$

- formation of a lattice oxygen and two electron holes due to the incorporation of molecular oxygen into the oxygen vacancies of the membrane.

$$\text{Permeate Side: } O_O^x + 2h^{\bullet} \rightarrow ½\, O_2 + V_O^{\bullet\bullet} \quad (7)$$

- formation of molecular oxygen and the release of one oxygen vacancy due to the recombination of lattice oxygen with the electron holes.

In these equations, $V_O^{\bullet\bullet}$ refers to oxygen vacancies, O_O^x to oxygen ions occupying the oxygen lattice and $h^{\bullet}$ represents an electronic hole, in accordance with Kröger–Vink formalism as is shown in Figure 10. [2][21]

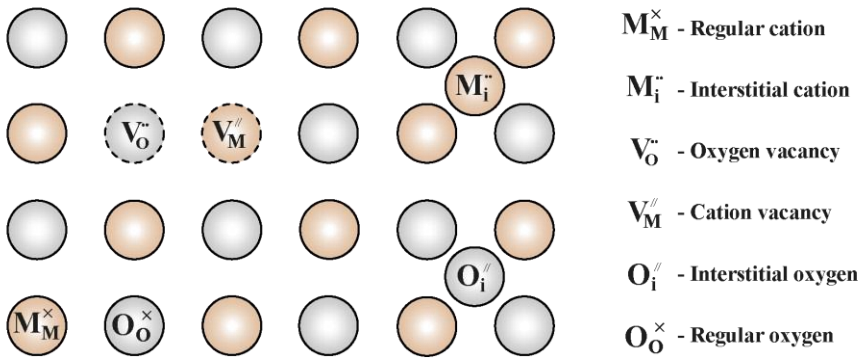

Figure 10 - Illustration of Kröger-Vink nomenclature of structure elements (Adapted from [22])

1.3.3. Effects of membrane thickness.

In order to distinguish the rate-determining steps in oxygen transport (bulk diffusion or surface exchange kinetics), a characteristic thickness of the membrane, L_c, was defined. [15][18] For instance, when the membrane is thicker than L_c, the permeation of oxygen through the membrane is controlled by the bulk diffusion, while, for a membrane thinner than L_c, the oxygen permeation though the membrane is controlled by the surface exchange kinetics, as is shown in Figure 11. [6][19]

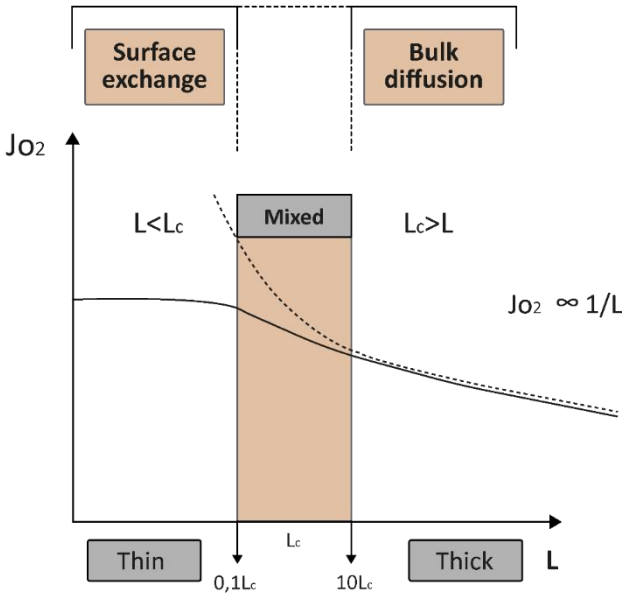

Figure 11 - Evolution of the rate-determining step of oxygen flux with the influence of the characteristic thickness L_c. (Adapted from [14])

Normally, the critical membrane thickness reported in the literature correspond to the values from 20 μm to 3 mm. However, these values are affected by different parameters such as temperature, oxygen partial pressure, membrane composition, and, consequently, they can vary significantly.[23][13] The characteristic membrane thickness L_c, considering some relations presented in Equation (8), can be elucidated in Equation (9): [18]

$$t_{el}t_{ion}\sigma_{total} \Leftrightarrow \frac{\sigma_i \times \sigma_e}{\sigma_i + \sigma_e} \; and \; \Delta\mu_{O_2}^{total} \Leftrightarrow \frac{\partial RTln\, P(O_2)}{\partial x} \quad (8)$$

$$L_c = \frac{R \times T}{16 \times F} \times \left(\frac{t_{el}t_{ion}\sigma_{total}}{J_{ex^o}}\right) \quad (9)$$

In the case when the membrane thickness value is very close to the L_c, a mixed mechanism occurs, and neither bulk diffusion nor surface exchanges dominates, in which the total driving force in oxygen permeation is shared. In other words, the drop of oxygen chemical potential is equal for both mechanisms, as is shown in Equation 10. [1][6][24]

$$½\Delta\mu_{O_2}^{total} = \Delta\mu_{O_2}^{surf} = \Delta\mu_{O_2}^{bulk} \quad (10)$$

where $\Delta\mu_{O_2}^{total}$ is the total oxygen chemical potential difference across the membrane. [1]

The flux in Equation (3) can be rewritten like Equation (11), assuming a small oxygen partial pressure gradient through the membrane, and now, considering the characteristic thickness. [14][18][24]

$$J_{O_2} = \frac{1}{1+(2Lc/L)} \times \left(\frac{t_{el}t_{ion}\sigma_{total}}{16 \times F^2}\right) \times \left(\frac{\Delta\mu_{O_2}^{total}}{L}\right) \quad (11)$$

When compared to Equation (3), it is perceived that the diffusion flux of oxygen across the membrane is reduced by the factor $1/\ 1 + (2Lc/L)$. This consideration represents the reduction ratio of the oxygen permeation flux, as the rate-determining step shifts from the total bulk diffusion limitation to the mixed control by both bulk diffusion and surface exchange. [8][18]

For the membranes based on the perovskites-type oxides, where the electronic conductivity dominates over ionic, the limitation for bulk diffusion is consequently established by the diffusion of oxygen ions involving oxygen vacancies. [14] Considering

purely anionic conductivity and taking in account the relation of Equation (12), Equation (13) can be described by the Nernst-Einstein. [8][14][19][25].

$$C_o = \frac{[V_O^{\cdot\cdot}]}{[V_m]} \tag{12}$$

$$\sigma_{ion} = C_o D_s Z_O^2 \times F^2 \times \frac{1}{RT} \tag{13}$$

where D_s is the chemical diffusion coefficient of oxygen vacancies and Z_O^2 is the valence charge of the oxygen anions. [6][14] Equation (9) can be more clarifying assuming the predominance of electronic conductivity ($\sigma_e = 1$), so using Equation (11) and Nernst-Einstein Equation (13), the characteristic thickness corresponds to: [2][13]

$$L_c = \frac{Ds}{K_s} \tag{14}$$

This equation is only applicable when the surface exchange rates are similar at the opposite interfaces of the membrane, under a small oxygen partial pressure gradient over the membrane. [14][19] The diffusion and surface exchange coefficients are significantly affected by temperature and oxygen partial pressure; therefore, L_c is also relatable to these parameters. [18]

1.4. Approaches for improving the oxygen exchange rate.

The oxygen permeation flux through a MIEC is dependent on numerous parameters, such as the membrane material dimensions, as well the operation conditions. So, the oxygen permeation flux can be improved by modifying these parameters to reach the best performance. While reducing the membrane thickness to the value of L_c is viable when the oxygen permeation rate is limited by bulk diffusion, reducing the membrane thickness when the flux is limited by the surface exchange reactions does not bring any improvements. Membrane thickness reduction only increases the oxygen permeation if the thickness of the membrane is larger than the characteristic thickness, L_c. [11]

1.4.1. Surface activation of the membranes.

When the limiting step is the surface exchange kinetics, it must be enhanced to improve the overall oxygen flux. A common practice towards improving the oxygen permeation flux is a membrane surface modification or treatment. A modification on the

surface of the membrane or the deposition of catalysts, can provide a higher effective surface area, increasing the surface exchange kinetics and consequently the oxygen permeation. [1][11] An increase of the surface area creates additional active sites on the surface of the membrane for the incorporation of O_2 molecules and will inevitably boost the thermodynamic process of oxygen permeation. [1][26]

Some of the strategies implemented for the modification of the surface of the membrane to enhance the surface area are based on the chemical etching in different acid solutions. This treatment helps to modify the chemical composition on the surface and membrane area, contributing to produce irregularities, thus increasing the effective surface area available for the oxygen exchange. Simple roughening or polishing of the membrane surface also increases the oxygen permeation. [9][27]

Another efficient approach to increase the surface area and enhance the surface exchange kinetics of the membrane is the deposition of a thin porous catalytic layer on the surface. [13][28] In this way, modification of the surface properties of the membrane by depositing catalytic species, like silver or platinum oxides, promotes the efficiency of oxygen dissociation and recombination, and the surface exchange kinetics can be considerably enhanced. [29][28] An addition of a catalytic layer (Figure 12) helps to achieve a higher reaction efficiency without increasing the temperature significantly. [26]

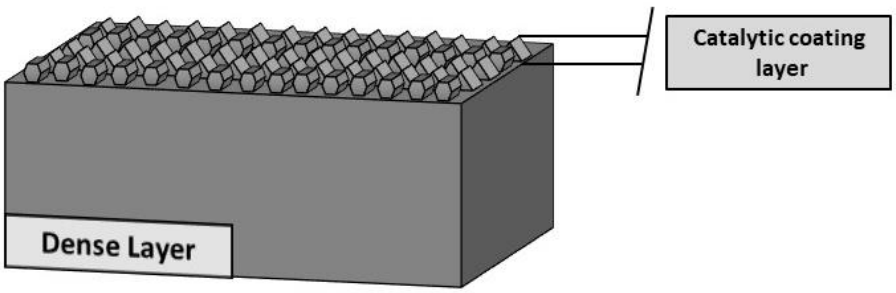

Figure 12 - Representation of a MIEC membrane with a catalytic layer. (Adapted from [14])

1.4.2. Membrane geometries with porous layers.

Assuming the presence of only bulk diffusion limitation to the overall oxygen transport, the reduction of the thickness of the membrane as much as possible is a feasible way to increase the oxygen flux. However, very thin membranes become brittle, and adequate mechanical stability is lost. [12][30]

The approach involving asymmetric membrane concepts helps to overcome the mechanical limitations, while ensuring high permeation fluxes. These membranes are constituted by the thin oxygen selective dense layer (MIEC membrane) supported by a thicker porous substrate (Figure 13). The mechanical insurance of the membrane is provided by the porous layer. [13][30][31]

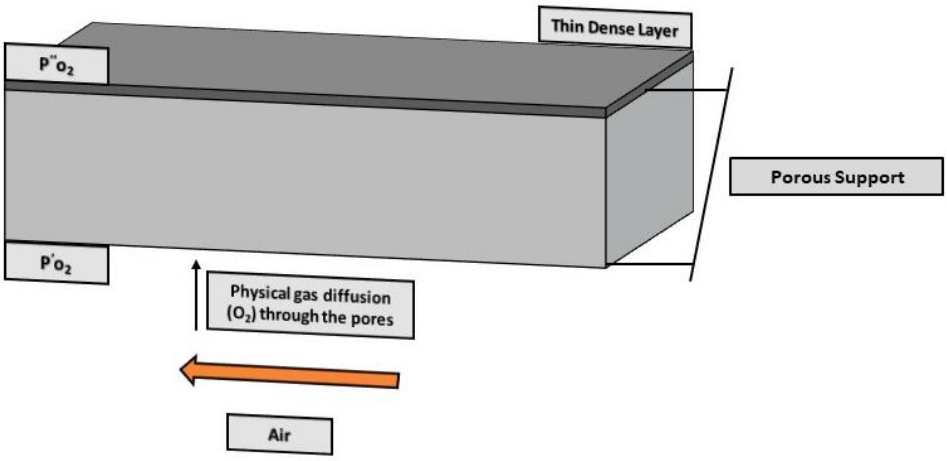

Figure 13 - Representation scheme of an asymmetric structure membrane (Adapted from [16])

Besides the mechanical support action, this layer can multiply the number of oxygen exchange sites, improving indirectly oxygen permeation through the membrane. [32] In order to have a good assembly between the porous support layer and the dense layer, the constituents of the asymmetric membranes, the chemical compatibility and thermal expansion between them need to be compatible. [13][29]

As the thicker porous supports are introduced to ensure the mechanical integrity of the membrane, new additional problems and/or new advantages can appear. If the materials of both layers differ considerably, thermal expansion and shrinkage could also

differ and may provoke significant mechanical stresses at high temperatures, where damage, such as cracks and detachment of fragments from the surface of the layers, can occur, affecting the performance of the membrane. [12] At the same time, porous support itself may act as an extension of the active membrane surface, boosting the oxygen flux. However, a careful design of the support porosity is required to decrease the diffusion resistance, allowing a better permeation through the membrane. In fact, insufficient porosity or porosity percolation in the porous layer may become an extra limiting step of the oxygen permeation through an asymmetric membrane. Thus, to benefit from the presence of the porous layer, it is important to develop the best porosity architecture to get the lowest gas flow resistance and to inhibit the possible accumulation of nitrogen in these pores. [30][33] The oxygen permeation can be limited by the exchange at the feed or permeate side, because the surface exchange rate depends on the oxygen concentration. So, it is important to place the porous support on the membrane side that is limiting the oxygen permeation flux, because the benefits of the porous support will increase the overall flux. [34]

1.5. Materials for MIEC membranes.

This section briefly reviews some promising materials for oxygen permeation membranes. As follows from Equation (3), in order to have a higher oxygen diffusion flux, a reasonable compromise between oxygen-ionic and electronic conductivities should be found. Therefore, mixed-conducting materials represent the best option for the membranes operating under gradient of the oxygen chemical potential.

1.5.1. Perovskites

The perovskite materials are characterized by the stoichiometry $ABO_{3-\delta}$, in which A is a large cation (1.10–1.80 Å), B a medium-size cation (0.62–1.00 Å) and O is a large-sized anion (1.40 Å). [14] The properties of the structure perovskite-type materials are directly related to the cations chosen to constitute the lattice and the oxygen deficiency. Commonly, rare-earth and alkaline-earth metal cations (La, Sr) occupy A sublattice, while transition cations (Fe, Ni, Co) constitute the B sublattice. [1][9][11][34]

Figure 14 exemplifies an ideal perovskite with a cubic structure, where A cation are positioned in the corners of the structure, the B cation occupies the central position and oxygen is presented in the center of the phase. [12]

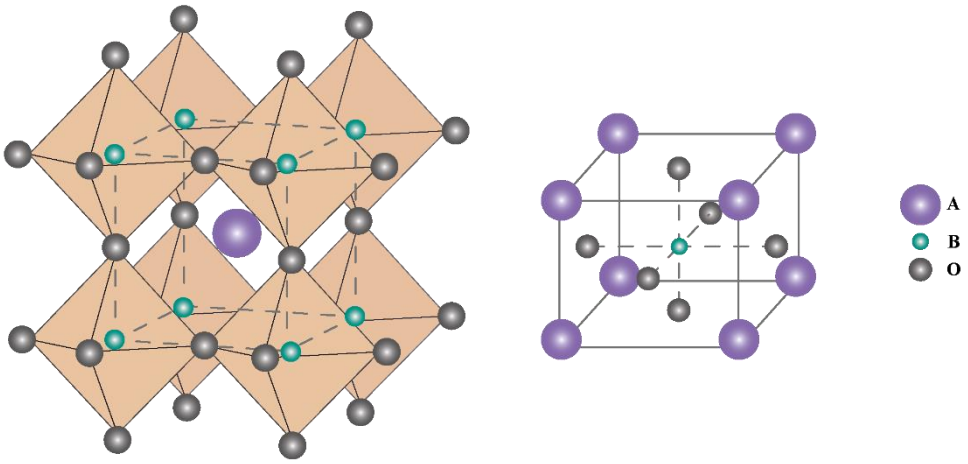

Figure 14 - Structural representation of an ideal perovskite. (Adapted from [12])

The B cation forms an octahedral geometry with the oxygen (BO_6), and the A cation forms a cuboctahedron with the respective oxygen ions. [14][35]

Usually the perovskite-type materials exhibit superior electronic conductivity as compared to ionic counterpart, making the latter a limiting factor for the respective oxygen permeation process. In order to significantly improve the ionic conductivity, some structural implications need to be considered, including the tolerance factor, the cation sizes and valences, and oxygen non-stoichiometry. [1]

The stability of the perovskite structure is established by the tolerance factor, presented by Goldschmidt in the following Equation (15). [10]

$$\text{Tolerance Factor (t)} = (r_A + r_O) / (\sqrt{2} \times (r_B + r_O)) \quad (15)$$

in which the r_A is the ionic radius of the A cation, r_B is the ionic radius of the B cation and r_O is the radius of oxygen ions. The sizes of A and B ions impose a major effect on the structure. In order to preserve the structure stability, the values of the tolerance factor

must be between 0.75 < t < 1. [7][34] If the tolerance factor deviates significantly from unity, due to the difference of dopant radius, an orthorhombic or rhombohedral distortion can appear. Typically, orthorhombic/rhombohedral structures can form for the values of t between 0,75 and 0,90, whereas the ideal cubic structure is preserved for values between 0.9 and 1.0. [11][36]

To improve the ionic conductivity, the formation of oxygen vacancies needs to be promoted. This could be achieved by substituting the A and B cations of the perovskite lattice with ions having different valences. [1] For example, partial substitution of the A-site cation by a cation with lower valence than the host A cation promotes the formation of oxygen vacancies as a result of charge compensation mechanism. This approach to create oxygen vacancies is called aliovalent substitution and is represented in Figure 15.

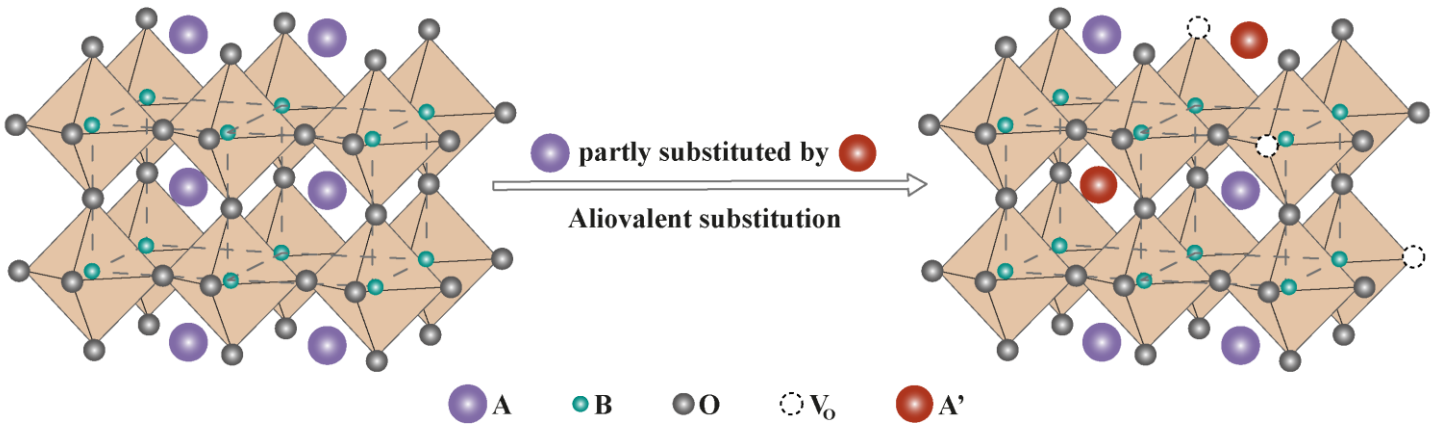

Figure 15 - Structural mechanism of aliovalent substitution. [37]

An isovalent substitution can be also used to generate oxygen vacancies. In the case of isovalent substitution, the partial substitution of A atoms with another atom with the same valence of A atoms occurs. The generation of oxygen vacancies is promoted by the difference in the ionic radius that induces strains distorting the structure and causing the appearance of more defects. [37]

The compensation mechanisms may involve a change of the oxidation state of B cations to maintain the charge neutrality. [2] This mechanism is possible due to the ability to form redox couples like $B^{4+/}B^{3+}$ (mixed valence), which consequently enhances the

electronic conductivity, whereas the creation of oxygen vacancies increases the ionic conductivity.

The perovskite structure is versatile and has a high potential to accommodate different cations. This makes it possible to obtain various compositions with different charge distributions, like, for example, $A^{1+}B^{5+}O_3$ or $A^{3+}B^{3+}O_3$, for which the perovskite structure is still maintained despite the different ionic sizes and oxidation states. [2][10][11] Replacing partially the A-site cations with others having a higher oxidation state can limit the formation of oxygen vacancies and jeopardize the overall conductivity. [9][11]

The substitution in perovskites can be generally represented as $A_xA'_{1-x}B_yB'_{1-y}O_{3-\delta}$, where δ is called oxygen nonstoichiometry and represents the number of vacancies per formula unit. The overall oxygen content, $3-\delta$, depends on many factors, including charge and size mismatch between the cations, and determines the overall ionic diffusion. [7]

Most common and studied perovskites for membrane applications are those based on SCF ($Sr(Co,Fe)O_{3-\delta}$) and BSCF ($Ba_{1-x}Sr_xCo_{1-y}Fe_yO_{3-\delta}$), provided by high oxygen permeation fluxes as compared to other materials. However, both of these perovskites present cobalt in their composition, resulting in several disadvantages like instability and degradation of the membrane in reducing environments. [38] Another issue is represented by the tendency to form carbonates in CO_2- containing environment, provided by the alkaline nature of alkaline-earth cations. [17][38][39] Other disadvantages of perovskite materials include unstable behaviour at various oxygen chemical potential gradients (air/CH_4), while a viable rate of oxygen permeation (1 cm^3 /cm^2. min) is still not achieved. [10]

1.5.1.1. Perovskites related phases (K_2NiF_4-type)

The K_2NiF_4-type structure belongs to the Ruddlesden-Popper type compounds and presents a stoichiometry of A_2BO_4, involving an alternating ABO_3 perovskite layer and a rock-salt-type layer (AO) (Figure 16). One typical example of this structure is the $La_2NiO_{4+\delta}$. [40][41] There is the possibility of excess oxygen incorporation between the AO planes and the ABO_3 layers, and oxygen interstices are positioned here, within the rock-salt-type layers. This creates an additional mechanism for oxygen transport through

these materials. Still, depending on the composition, substitution type/level and external conditions (temperature, oxygen partial pressure), these materials may possess a significant level of the oxygen nonstoichiometry in the perovskite layers. [42] Because of their specific properties, such as various possibilities for lattice distortions, the existence of different oxygen transport mechanisms and higher thermochemical stability as compared to perovskites, K_2NiF_4-type structures attract increasing attention as materials for MIEC membranes. [13][43]

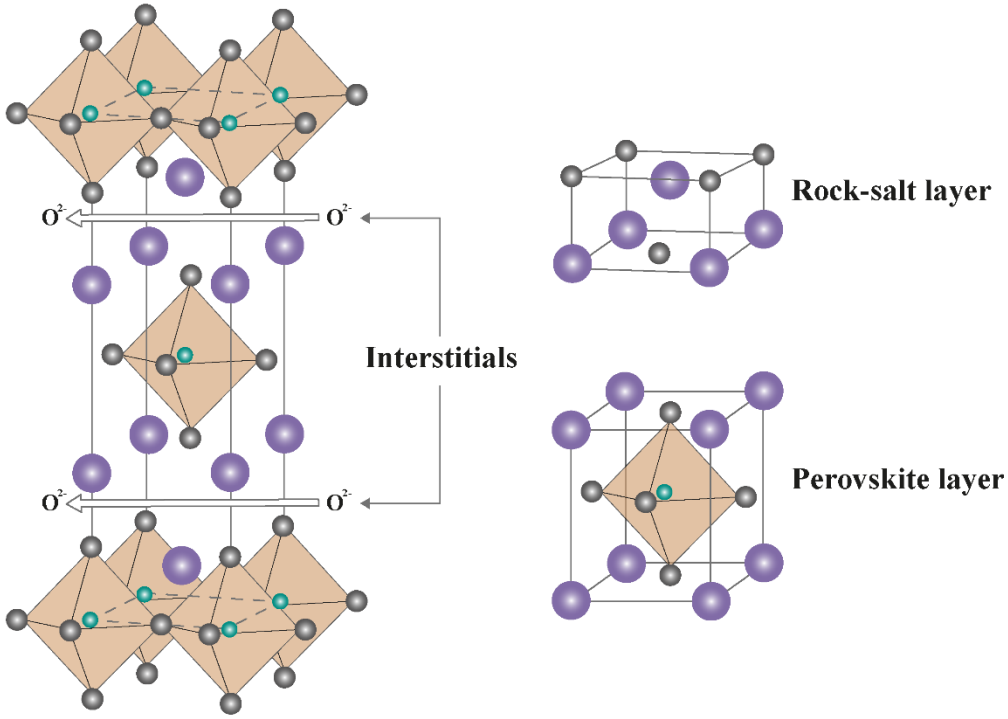

Figure 16 - Structural representations of the type perovskite material K_2NiF_4. [39][42]

1.5.2. Fluorites

Materials possessing fluorite-type structure usually exhibit rather poor electronic conductivity, along with attractive ionic conductivity. Consequently, they present relatively low oxygen permeation. [14][32] While perovskites present better oxygen flux as compared to fluorites, the latter materials present much better thermochemical stability. As an example, the fluorite structure is typically maintained under CO_2 and reducing environments. [1][12]

A general representation of the fluorite-type oxide structure is shown in Figure 17. It is usually represented by the formula MO_2. [12]

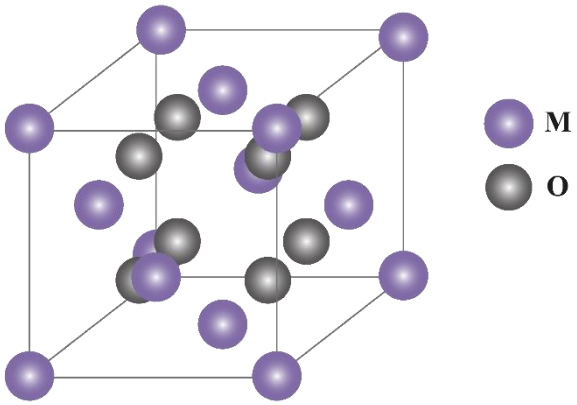

Figure 17 - Representation of a fluorite-type structure. [10]

The M cation can be represented, for example, by Zr^{4+} or Ce^{4+}. This structure consists of the anions forming a simple cubic packing, tetrahedrally coordinated to the metal cations, and the cations are presented in a face-centered cubic (FCC) arrangement. [9][12][44]

The most common fluorites-type ZrO_2, Bi_2O_3 and CeO_2-based phases exhibit good ionic conductivity and are consequently considered as potential materials for MIEC membranes. [7] The most typical applications of fluorite oxides are electrolytes in solid oxide fuel cells (SOFC) and oxygen sensors due to their suitable and predominant ionic conductivity. However, while having a good ionic conductivity, the fluorites show relatively low electronic conductivity. Similar to the perovskite structure, the incorporation of various dopants in the fluorite structure, e.g. alkaline and rare earth ions can lead to the formation of oxygen vacancies, raising the overall ionic conductivity while maintaining the structure stability. [1][32]

Fluorites materials become very interesting when the cations are substituted by species with lower valence creating anion-deficient phases, like $A^{4+}_{1-x}B^{3+}_{x}O_{2-x/2}$ or $A^{4+}_{1-x}B^{2+}_{x}O_{2-x}$, in which charge compensating vacancies are formed allowing an increase in mobility of the anions through the crystal, leading to an excellent ionic conductivity.

This happens in ZrO_2 when doped with trivalent cations, like Y^{3+}or Sc^{3+}. The ionic conductivity can be increased by the substitutions until a certain limit. For instance, in $Zr_{1-x}Y_xO_{2-x/2}$, increasing the value of x leads to the formation of vacancies and enhancement of ionic conductivity until a limit in ionic conductivity is reached. This limit occurs because of the size mismatch between host and dopant cations causing lattice strains and due to the formation of defect clusters confining the vacancies mobility. [45][46]

Fluorites are very suitable for various composite concepts of the MIEC membranes, where they provide high ionic conductivity, while the electronic counterpart is contributed by another phase (e.g., perovskite). [47]

1.6. Hydrothermal processing.

1.6.1. Basics.

The hydrothermal process is characterized by a heterogeneous or homogeneous reaction in ambient with aqueous or non-aqueous solvents in a closed system under high pressure and adequate temperature conditions to promote the chemical reactions to synthesize and crystalize powders. [48][49] This process normally occurs above 100°C and pressures above 1 bar, with an acceleration of heterogeneous reactions which also permits the dissolution or recrystallization of inorganic compounds that in normal conditions are insoluble. [50][51] The hydrothermal synthesis of inorganic crystalline compounds can be performed in various ways, including solvothermal and supercritical process. The solvothermal process corresponds to the case when the solvent is not water, and an organic solvent is used. In supercritical conditions, the solvent is above it´s critical point of pressure and temperature and exhibits ideal properties to high reaction rates and rapidly nucleation for inorganic materials formation. [49][50][52] With the hydrothermal process it is possible to prepare various advanced materials, whether in the form of bulk single crystals, fine particles/powders, or nanoparticles. The minimum variation in the different parameters of this technique, such as temperature, the solvent, reaction time, pH, precursor concentration allows the control, or significant changes in the morphology, composition, crystallinity, and size of the particle formed. [49][50]

The solvent is one of the most important parameters in the hydrothermal process and its role, along with the temperature and pressure, is to provide the proper atmosphere

to the unwind of reactions. In many cases, the solvent determines the impact on the particle shape and size, and depending on its nature the reactions can occur at lower temperatures. [49][50][51] During hydrothermal processing, the reactions always take place in a closed system, that, in this case, is called a pressure vessel (autoclave) (Figure 18). A suitable autoclave must present certain characteristics, such as the ability to endure relatively high temperatures and high pressures for a lot of experiments. Also, it must have the capability to sustain harsh chemical environments (inert material) such as acids, bases, and oxidizing agents, without leakage occurring in the vessel, while the assemble and disassemble procedures must be straightforward. [51]

In comparison to other advanced materials processing techniques, like mechanical milling, sol-gel, chemical and physical vapor deposition and laser ablation, hydrothermal processing presents various advantages, including lower capital and operating cost, lower energy consumption and better nucleation and shape control along with the process simplicity and faster reaction times. [49][51] In many cases, it is also characterized as a single-step process, in which the material generated does not present the need for a posterior treatment, such as annealing. Because the process is accomplished in a closed system, it does not directly result in any pollution and facilitates separation and recycling, if needed. [49][50]

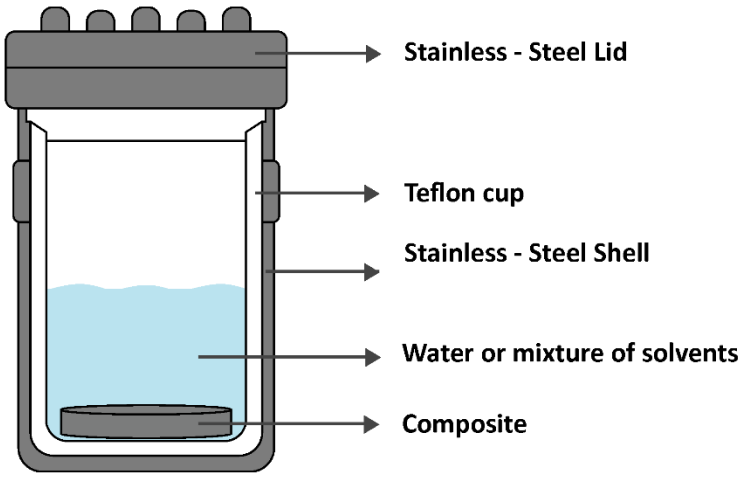

Figure 18 - Schematic diagram of the autoclave used in hydrothermal synthesis.

1.6.2. Current trends in hydrothermal processing technology.

The hydrothermal process can be performed using various techniques, which makes it more advanced compared to conventional processes. Some of those are hydrothermal synthesis, hydrothermal crystal growth, and, more recently, hydrothermal recrystallization, hydrothermal leaching, hydrothermal metal reduction and hydrothermal etching. [51] Today it is common to introduce external energy in the hydrothermal process, such as sonar energy, mechano-/electro-chemical energy and microwave energy, with more spotlight on the latter. The microwave hydrothermal process allows a higher heating rate to the desired temperature, allowing the improvement of the reaction kinetics (rapid crystallization), and, consequently, reducing the synthesis time. [49][51]

When it comes to nanotechnology, the hydrothermal process is also ahead of the conventional processing techniques, which is imperative, due to the unique properties of nanoparticles in comparison to particles with normal dimensions. This significantly extends the range of potential applications. With the careful control of the parameters of the hydrothermal process, it is possible to obtain rapidly different composites or metal oxide nanostructures with various morphologies like, for example, nanorods or nanowalls. Using the hydrothermal process, these nanostructures can be applied in a form of films/coatings with or without porosity on different substrates, increasing the surface area, surface topography, and improving the catalytic action on different applications. [49][51][53] In the present work, combined leaching and deposition techniques under hydrothermal conditions will be applied, for the first time, to activate the surface of the MIEC membranes towards oxygen exchange.

2. Experimental Procedure

2. Experimental Procedure

In this chapter, all the experimental procedures employed during the realization of this thesis will be presented. First, the procedures related to the processing of the samples is described, as well as the powder processing and shaping. Then, the techniques used for the physicochemical characterization of the samples are described. Basic aspects and common procedures involved in the techniques, will be detailed.

2.1. Material Synthesis

$(SrFe)_{0.7}(SrAl_2)_{0.3}O_x$ (0.7 $SrFe0_{3-\delta}$ × 0.3 $SrAl_2O_4$) - SF7SA3 composite powder was prepared via the glycine-nitrate process (GNP), a self-combustion technique, using nitrates of metal components as an oxidant, and glycine as fuel and chelating agent. The employed precursor powders to obtain the aimed composite, included strontium nitrate, iron nitrate nonahydrate and aluminium nitrate nonahydrate, shown in Table 2.

Table 2 - Characteristics of the reactant powders.

Composition	Name	Supplier	Degree of Purity (%)
$\mathbf{SrN_2O_6}$	Strontium Nitrate	Sigma-Aldrich	≥ 99
$\mathbf{AlN_3O_9.9H_2O}$	Aluminium nitrate nonahydrate	Sigma-Aldrich	≥ 98
$\mathbf{FeN_3O_9.9H_2O}$	Iron (III) nitrate nonahydrate	Sigma-Aldrich	≥ 98
$\mathbf{C_2H_5NO_2}$	Glycine	Sigma-Aldrich	99

With their appropriate stoichiometric ratios, these precursors powders were dissolved in distilled water in their respective beaker, and after total dissolution, were mixed together. Then, the glycine was added to the metal nitrates in the aqueous solution, acting as a complexing agent and fuel. The aqueous solution was then evaporated on a hot plate by heating up to 200°C to remove excess water, thickening and generating a viscous liquid. With increasing temperature, the spontaneous combustion of the viscous liquid occurred at hot-plate temperature of around 280°C, generating ash and powder of the oxide product, homogenized at the atomic scale. During burning the beaker was covered with a stainless-steel mesh to avoid abrupt releases of this ash. The overall GNP procedure is demonstrated in Figure 19.

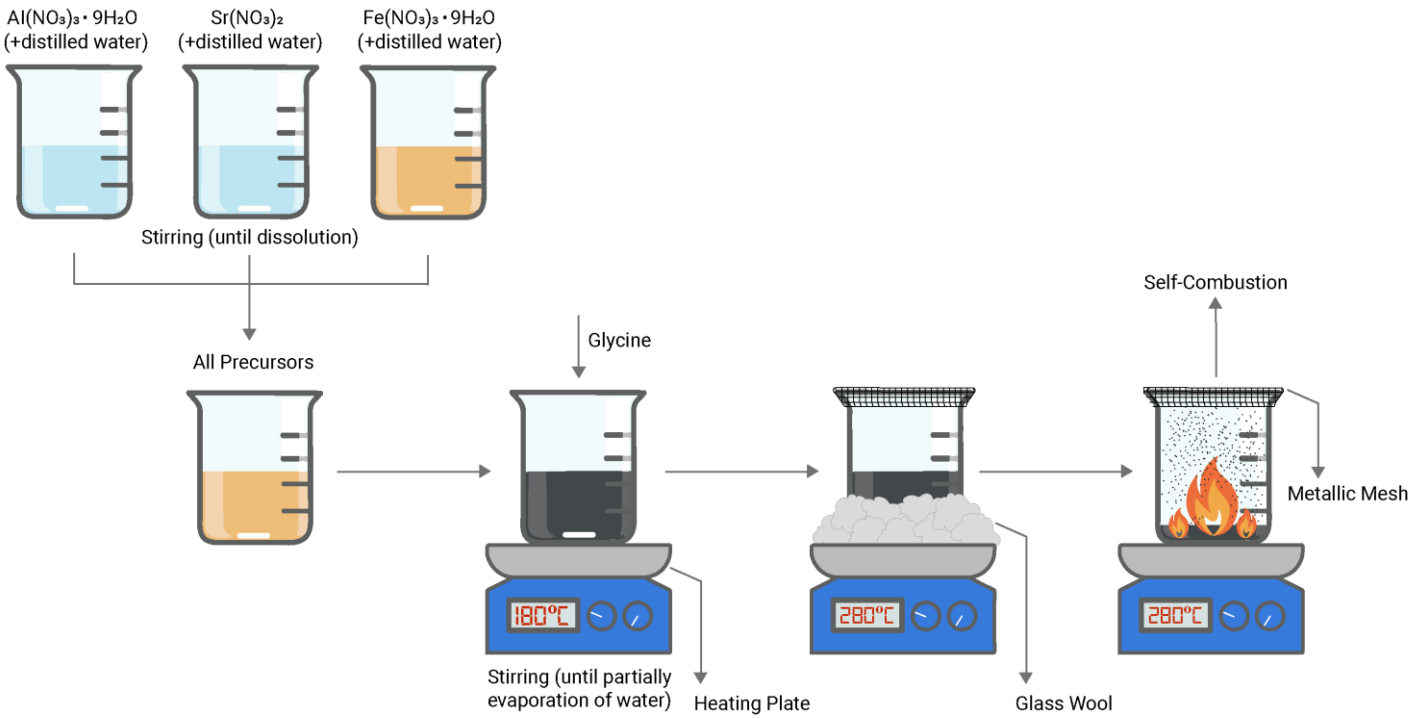

Figure 19 - Schematic representation of the glycine-nitrate combustion synthesis.

The obtained powder was then grinded with ethanol, to break some resultant agglomerates and obtain a good homogeneity, and then was dried in a drying furnace. The calcination at 900°C in the furnace "Nabertherm B150" was used to remove carbon residues still present in the powder, with the temperature profile demonstrated in Figure 20.

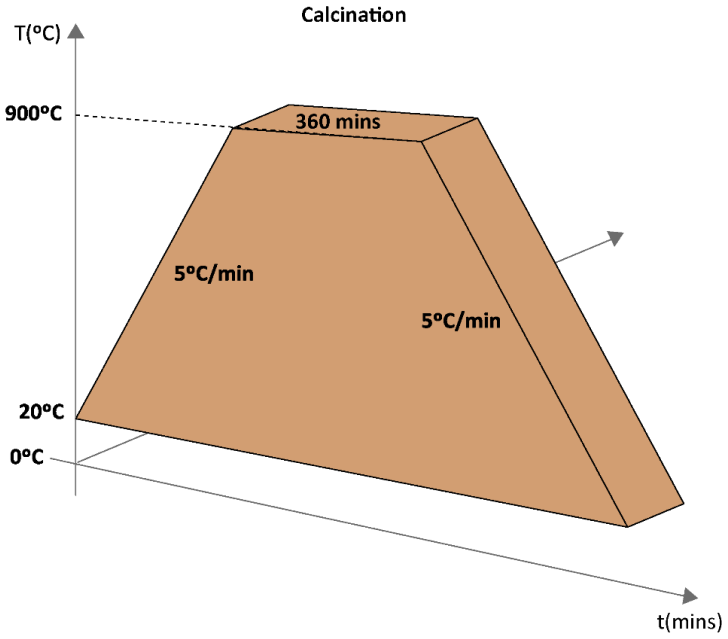

Figure 20 - Schematic representation of the calcination profile of the composite powder.

2.1.1. Sintering

The disc-shaped samples, further suitable for testing as oxygen permeation membranes, were prepared using an 18 mm diameter mould and a uniaxial pressing machine P/O/Weber" under pressure of ≈ 30 MPa during ≈ 60 s, followed by isostatic pressing (IP) in "Autoclave Engineers Inc" equipment at ≈ 196 MPa during ≈ 60 s. Prior to IP, the pressed pellets were placed in a rubber case, which was further vacuumized. After IP, the pellets were sintered in air atmosphere, using the thermal treatment shown in Figure 21.

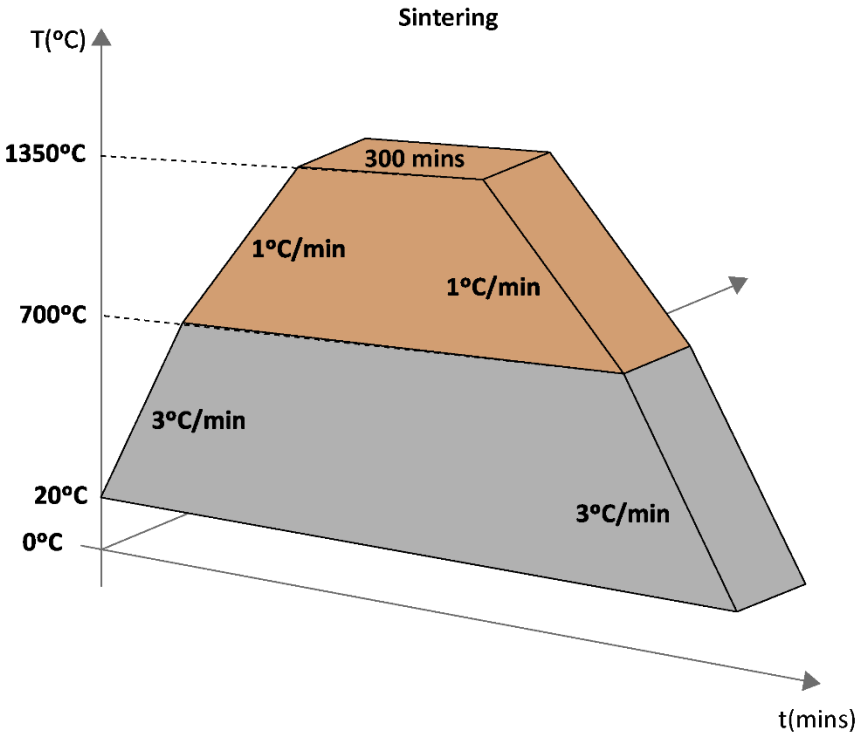

Figure 21 - Schematic representation of the sintering treatment of the pellets.

Sintering of dense and crack-free SF7SA3 samples was only possible involving very low heating and cooling rates, since strontium ferrites with small Al additions often present microcracks at the grain boundaries caused by the possibility of large changes in oxygen nonstoichiometry. [54]

2.1.2. Hydrothermal Treatment

The activation of the sintered and polished SF7SA3 layers was performed by hydrothermal synthesis. It was carried out in an autoclave, using different modifying chemical agents (NaOH and Praseodymium nitrate), concentrations (0.1M and 1M) and temperatures (120º, 150º during 24h), other alternatives were also tested. The autoclave was placed in the drying furnace "Venticell MMM Group" with a thermal treatment, represented in Figure 22 as an example.

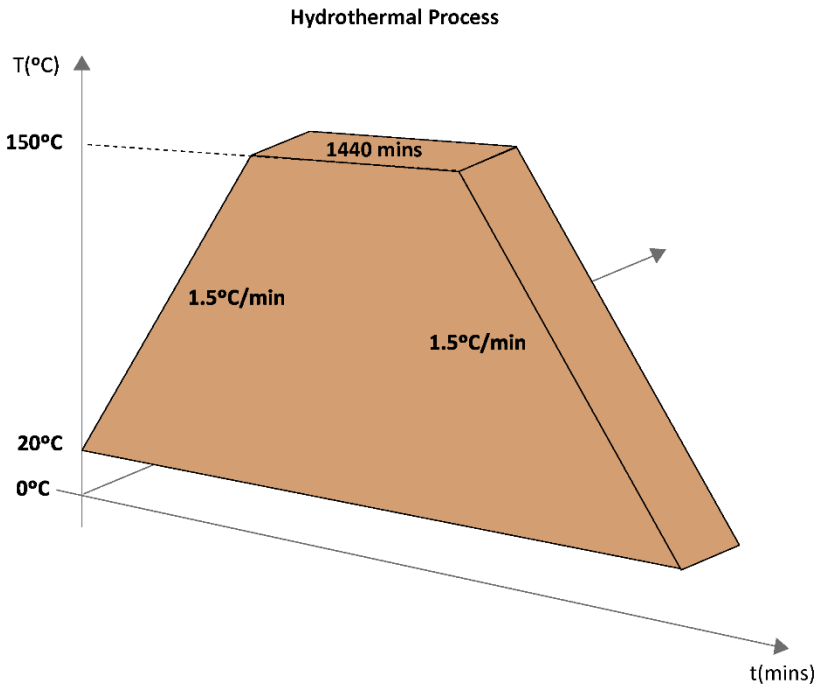

Figure 22 - Schematic representation of the hydrothermal treatment for the pellets.

The hydrothermal treatment often results in products possessing low crystallinity. Secondly, the final phase composition of the modifying layer of a membrane operating at elevated temperatures is expected to be notably different due to additional interdiffusion and interaction of the compounds formed under hydrothermal conditions. Thus, the surface-modifying layers posteriorly underwent a sintering process demonstrated in Figure 23.

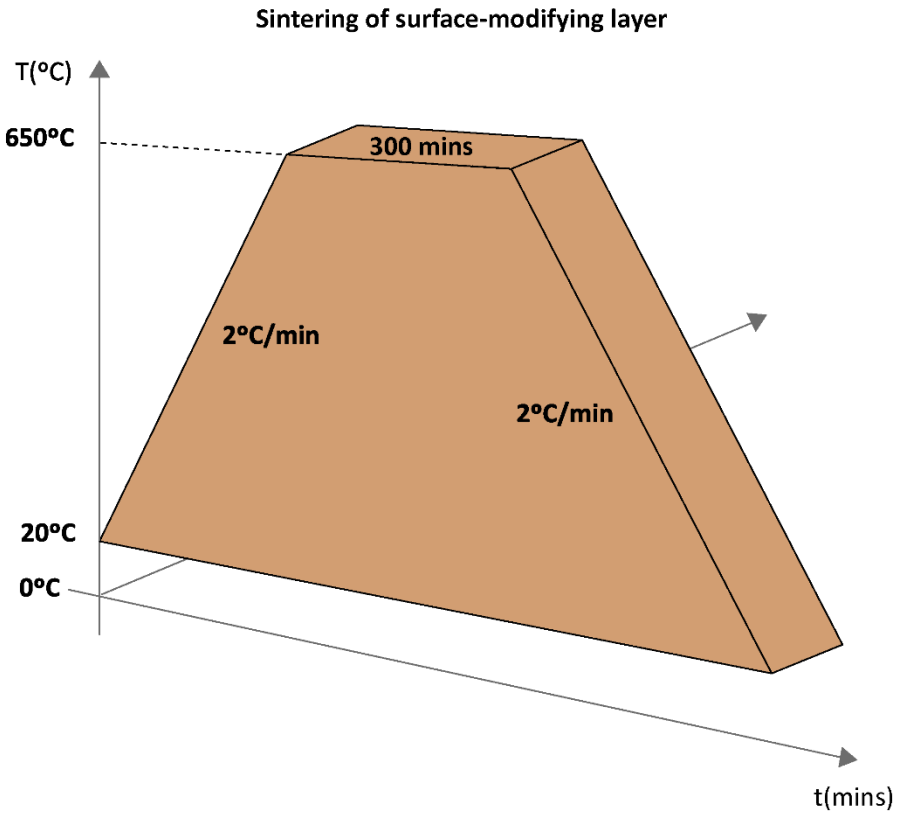

Figure 23 - Schematic representation of the thermal treatment used to equilibrate the phase composition of the surface-modifying layer.

2.2. Characterization Techniques

The sintered samples were cut and polished to have regular geometric shape of discs (diameter 13 mm, thickness 1 mm), appropriate for oxygen permeation studies and rectangular bars (2.5x2x12 mm^3) for dilatometric studies and electrical measurements. Experimental density was calculated from the weight and geometric dimensions of the samples. The powdered samples for X-ray diffraction were prepared by grinding the sintered ceramics. Also, XRD analysis were done in the top surface of the pellets after hydrothermal modification. In addition, prior to the oxygen permeation measurements, the pellets were tested for gas tightness.

2.2.1. Structural and microstructural characterization

X-ray diffraction is a non-destructive analytical technique used for the purpose to characterize a wide range of materials, obtaining their crystalline structure and phase composition. XRD measurements are based on the physical principle that a beam of X-rays with a wavelength λ bombards a crystalline material at a particular angle. XRD peaks are produced by constructive interference of the scattered X-rays beams at specific angles from each set of lattice planes in a sample. This phenomenon follows the conditions of Bragg's Law ($n\lambda = 2d\sin\theta$), obtaining a diffractogram of the sample with the representation of the intensity of the diffracted radiation as a function of the diffraction angle (2θ). This mathematical principle relates the wavelength of the electromagnetic radiation with the diffraction angle and lattice spacing present by the sample.

A diffractogram contains several characteristic peaks distinguish by their position, intensity, and shape. Each phase has a representative unique X-ray diffractogram, so the identification of the crystalline phases is done by comparing the diffractogram obtained with the standard diffractograms of the respective crystalline phases detected, using the software associated with the equipment. When analysing the diffractograms, it is essential to take in consideration three main factors: the number of existing peaks, the intensity, and respective position, since the combination of these factors corresponds to the unique characteristics of each crystalline substance.

The qualitative analysis of the crystalline phases was made by X-ray diffraction using a high-resolution diffractometer (Malvern PANalytical X'Pert) (Figure 24) with Cu Kα radiation (λ = 1.540598 Å). The data were acquired in a scanning range (2θ) from 5 to 90° with a step width of 0.0200° $2\theta \cdot s^{-1}$.

Figure 24 - High-resolution X-ray diffractometer “X'Pert PRO PANalytical”

The quantitative analysis of the crystalline phases was performed using the Rietveld refinement method (TOPAS Version 4.2, Bruker AXS, Karlsruhe, Germany). The selected ICDD numbers, for SF7SA3 composite were: #04-009-9992 for $SrAl_2O_4$ and #04-013-0199 for $SrFe_{0.9}Al_{0.1}O_{3-\delta}$.

The combined scanning electron microscopy (SEM) and energy dispersive spectroscopy (EDS) provides information on topography, morphology, and chemical composition of the analysed samples. This results from the detection of response signals from these samples, when subjected to the surface scanning process by a finely focused electronic beam with high kinetic energy. With the processing of this information, high-resolution images are obtained that allow the assessment of morphology aspects.

The EDS system integrated into the SEM system, uses an energy-dispersive detector to separate the characteristic x-rays of different elements into an energy spectrum. The energy of individual x-rays is then converted into electrical voltages, and analysed by the EDS system software, where it is possible to relate them to the characteristic x-rays of the element present and their respective abundance.

In this work, the combined SEM/EDS studies were performed using both powdered and fractured ceramic samples. The powdered samples were prepared by attaching a small amount of the powder to an aluminium holder with carbon tape. In the

case of ceramic samples, a carbon glue was used to fix fractured parts of the ceramic samples on the aluminium holder. After preparation, the aluminium holder with the samples was placed in an oven at ≈ 60°C for 24 hours and after subjected to deposition of carbon film (Carbon Evaporator K950) by a sputtering system. This deposition was done before microstructural analysis of the samples, to improve their surface electrical conductivity resulting in higher quality images. Finally, the morphology and microstructure of the various powders and pellets were evaluated by Scanning Electron Microscopy (SEM) "Hitachi SU-70" (Figure 25), as well as the chemical mapping by EDS, with an acceleration of 15 kV and different resolutions.

Figure 25 - Scanning electron microscope analysis (SU-70) used to collect the data.

2.2.2. Thermal and electrical characterization

Dimensional changes during heating and cooling of the oxygen membrane may significantly affect its mechanical integrity and compatibility with other construction materials in the reactor. A factor that might affect the mechanical integrity of the membrane subjected to a high oxygen chemical potential gradient during operation is the chemical expansion promoted by the changes in iron oxidation states.

In order to assess the thermomechanical behaviour, dilatometric studies were conducted in alumina vertical Linseis L75 instrument in different flowing air and argon mixed atmospheres and cycle durations, from 25–1100 °C, with a flow rate of 50 ml/min.

The temperature was controlled using a S-type thermocouple (Platinum Rhodium - 10% / Platinum) with accuracy of ± 1.5 °C.

Total electrical conductivity of the membrane material was also assessed, as an overall measure of ionic and electrical conductivity, which, in turn, determine the bulk ambipolar conductivity. The SF7SA3 samples were prepared by the following route. Sintered SF7SA3 pellet was polished and ultrasonically cleaned; then, the pellet was cut into a rectangular bar with dimensions of 2.55 × 2.0 × 11.93 mm^3 using a diamond disc saw. Two electrical contacts were fabricated by painting the bottom and the top ends of the sample with platinum paste to improve the electrical contact. Finally, two inner electrodes were implemented along the longitudinal axis in between the two end contacts by winding platinum wires around the sample, in a four-probe configuration. The electrical conductivity of this sample was tested using a four-point DC measurement based on the setup shown schematically in Figure 26. The equipment "Fluke 45 Dual Display Multimeter Keithley" was used to apply the current through the sample along its longitudinal axis and to record the voltage drop between the two inner electrodes. The four-point measurement was performed at 500 –1000 °C on cooling, to allow better sample equilibration with the atmosphere. The electrical conductivity σ was then calculated as $\sigma = \frac{L_i}{A \times R_t}$, where R_t is the resistance, A is the cross-section area of the sample, and L_i is the distance between the inner electrodes.

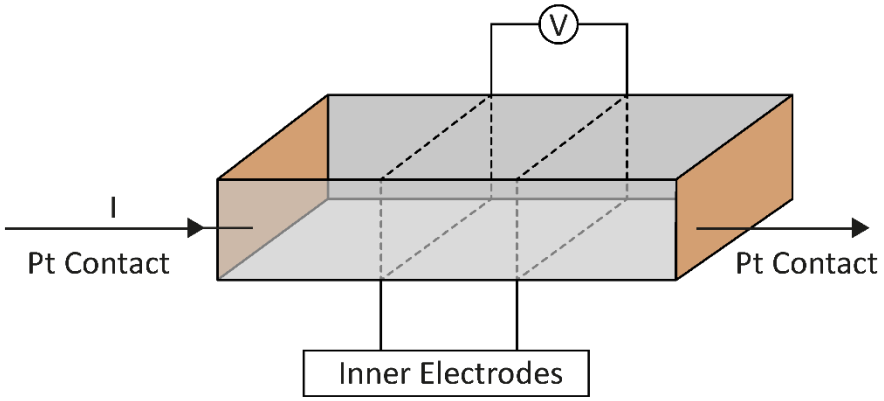

Figure 26 - Four-point measurement configuration with a standard sample.

2.2.3. Oxygen permeation and other relevant studies

Since the 100%-selective oxygen transport in ceramic membranes occurs through the crystal lattice, it is critically important to ensure the absence of leaks and throughout porosity in the samples used to measure oxygen permeation. Density (or porosity) represent the first suitable indicator allowing fast screening of the sintered ceramic membranes. The density was determined applying the geometric equation $\rho = \frac{m}{V_{Cylinder}}$, based on the measure of both the mass and dimensions of the pellet with the use of a precision scale and a micrometer, where ρ represents the pellet density, $V_{Cylinder}$ represents the volume of the pellet and m the pellet mass.

Still, even high-density values obtained for the ceramic membranes do not guarantee the absence of local macroscopic defects that may create a local pathway for physical gas diffusion. In order to verify the gas tightness of the composite membranes, proving their physical impermeability, a leak-proof test was carried out on the SF7SA3 composites. A pellet of SF7SA3 was glued to the end of a metal tube with a thermoplastic glue. Later on, a water droplet was placed to cover the entire membrane surface exposed to the visual observation, while compressed air was supplied to the tube interior (Figure 27). Absence of visual bubbles formation was taken as a criterion of physical gas tightness of the membrane. Gas-tight membranes were then used for oxygen permeation studies at high temperatures and hydrothermal modification.

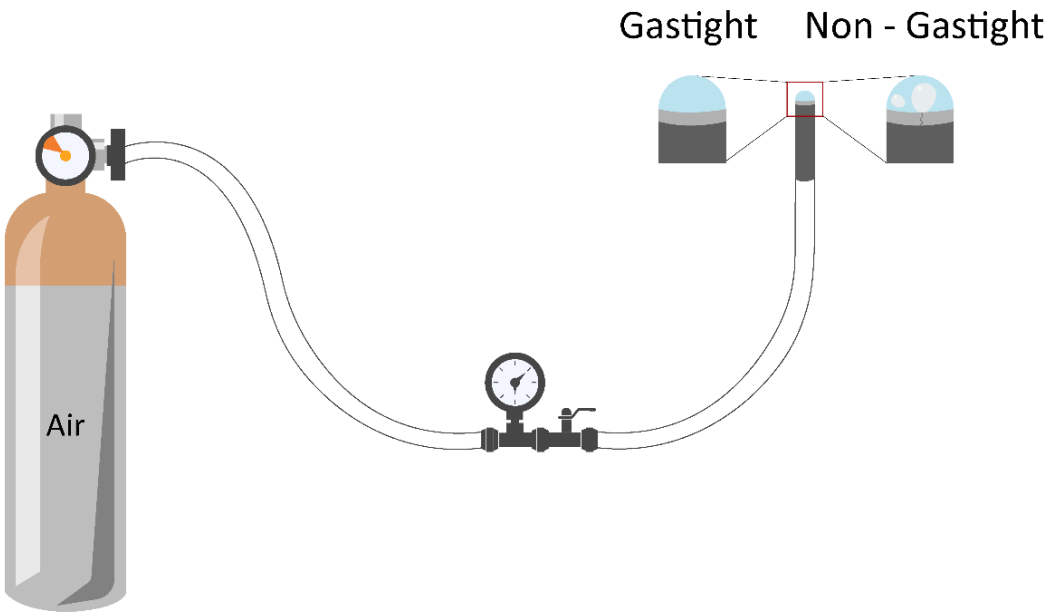

Figure 27 - Schematic representation of gas tightness tests.

Oxygen permeation studies were performed by two different homemade systems. In System 1 the quantification of oxygen potential gradient was performed using YSZ-based oxygen sensors, by calculation of the oxygen partial pressure from the sensor's EMF from the Nernst law. Two impermeable YSZ tubes with oxygen sensors were positioned in vertical position inside a tubular furnace allowing the application of various gases and their mixtures. In such setup, the oxygen chemical potential gradient is the driving source, forcing the molecular oxygen to permeate through the membrane towards air-exposed side. Therefore, during the oxygen permeability measurements, the feed side of the membrane was maintained at oxygen partial pressure of 21.2 kPa of oxygen partial pressure and the sweep side was maintained at lower oxygen partial pressure using an inert gas. [55]

The oxygen sensor allowed to directly calculate the oxygen partial pressure in the sweep gas, which was varied by changing the sweep rate and, thus, establishing various driving forces for oxygen permeation through the membrane. [56]

In System 2 as shown in Figure 28, the quantification basically was executed using an electrochemical cell made of yttria-stabilized zirconia (YSZ) employed with an oxygen pump and an alumina tube equipped with an oxygen sensor. In this setup the oxygen chemical potential gradient created by the electrochemical pump is the driving force to the movement of oxygen through the membrane, due to ionic transport.

Each of the outside and inside walls of the YSZ and alumina tube were coated with a small layer of platinum electrode paste welded with platinum wires connected to a voltage power. The oxygen sensor allowed the measurement of the oxygen partial pressure in the region surrounding the sample, and a thermocouple is placed close to the sample to record the exact temperature.

In both systems, the tested samples included gastight SF7SA3 disc-shaped non-activated and activated membranes with a diameter of ≈ 11 mm and thickness of = 1.00 mm. To avoid physical gas leaks during the measurements, these membranes were hermetically sealed onto the YSZ tube using a high-temperature glass based on silicates. Before the measurement, the sealing was heated up to 1120°C with a rate of 1°C per minute and remained for 10 mins at that temperature. Then it was cooled at the same temperature down to 950°C, where the permeability tests initiate.

The oxygen permeation data was obtained on cooling in the temperature range 750-950°C, with an interval of 50°C. To minimize the results error, each experiment was performed at least two times, where 1% was the estimated reproducibility error.

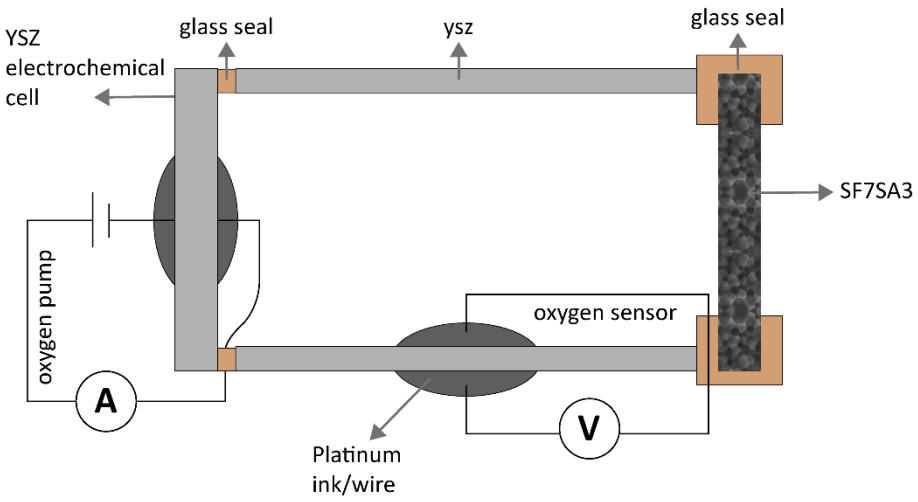

Figure 28 - Schematic representation of homemade System 2 for measurement of the oxygen permeability. [57]

3. Results and Discussion

3. Results and Discussion

3.1. Model Membrane material – selection and characterization

3.1.1. Justification of the selection

Since the proposed concept of the hydrothermal modification is new, a convenient model material should be selected for its proof. It implies that the oxygen permeation fluxes through corresponding membranes should be representative for applications, while the structural, electrical and transport properties must be well reproducible from sample to sample in various batches. Only in this way the eventual improvements or other changes provided by the hydrothermal modification can be easily detected and unambiguously interpreted. Ideally, the model material should also allow facile hydrothermal modification regarding the adherence of the modified surface layer and/or flexibility for using distinct approaches. In this respect, more information regarding material selection aspects is given in the Section 3.2.1. In the present work, the model material considered for hydrothermal modification, was the $(SrFe)_{0.7}(SrAl_2)_{0.3}O_x$ (0.7 $SrFeO_{3-\delta}$ × 0.3 $SrAl_2O_4$) – SF7SA3 dual-phase composite.

$SrFeO_{3-\delta}$ based perovskites are a promising family of mixed conductors, showing substantially high oxygen permeability. The high ionic conductivity exhibited by the strontium ferrite at elevated temperatures is provided by the high concentration of randomly distributed oxygen vacancies in the disordered cubic structure. However, due to associated large variations of oxygen non-stoichiometry, the variations of temperature and oxygen partial pressure provoke significant dimensional changes, decreasing the membrane robustness. In general, $SrFeO_{3-\delta}$ based membranes present insufficient mechanical strength.

One of the approaches to solve the above issues considers $(SrFe)_{1-x}(SrAl_2)_xO_z$ composites, constituted by strontium-deficient perovskite-like $Sr(Fe,Al)O_{3-\delta}$ possessing excellent ionic transport properties and $SrAl_2O_4$ phase, which is essentially low-conducting while having negligible chemical and relatively low thermal expansion. Such a composite structure can be naturally formed by conventional sintering of the powders prepared form single oxide precursors. Excellent chemical compatibility is provided by the presence of similar constituting cations. An incorporation of cations with stable oxidation state, such as Al, suppressing the oxygen nonstoichiometry variation, is

beneficial for reducing the excessive thermal expansion. The segregation of $SrAl_2O_4$ phase, improves the mechanical strength. Compared to single-phase $SrFe_{1-x}Al_xO_{3-\delta}$, $(SrFe)_{1-x}(SrAl_2)_xO_z$ composites exhibit similar oxygen permeability values with an enhancement of thermomechanical properties. [58]

Some other relevant parameters found in literature for SF7SA3 and $SrFe_{1-x}Al_xO_{3-\delta}$ phases are presented in Table 3, for better understanding of the following results presented.

Table 3 - Properties of SF7SA3 and $SrFe_{1-x}Al_xO_{3-\delta}$ composite ceramics. [22][59][60]

Composition	**Phases**	**Phase Composition**	**$T_{sintering}$, K**	**Vickers Hardness**, GPa	**Average TEC**	
					T, K	**$\alpha \times 10^6$ K^{-1}**
$(SrFe)_{0.7}(SrAl_2)_{0.3}O_x$ (SF7SA3)	$SrFe_{0.9}Al_{0.1}Oy$	Cubic Perovskite	1623	≈ 6,5	350-920	12,7
	$SrAl_2O_4$	Monoclinic			950-1230	25,2
$SrFe_{1-x}Al_xO_{3-\delta}$	$SrFe_{0.9}Al_{0.1}O_{3-\delta}$	Cubic Perovskite	1623	≈ 5	373 -823	16,4
					823 -1273	31,9

3.1.2. Structural and microstructural characterization

XRD studies of the powders prepared from sintered SF7SA3 show the formation of a dual-phase composite, composed of the strontium-deficient perovskite-like $Sr(Fe,Al)O_{3-\delta}$ phase, a cubic perovskite crystal system with space group Pm3m and the secondary $SrAl_2O_4$ phase with a monoclinic crystal system, as shown in the Figure 29.

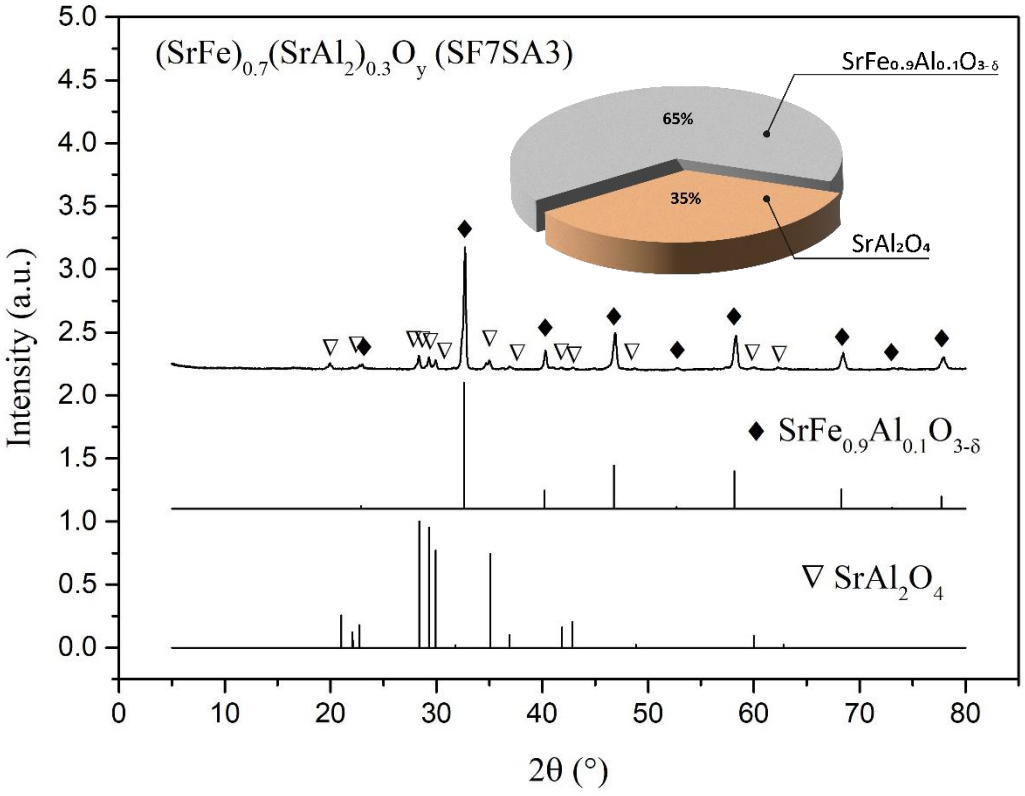

Figure 29 – XRD pattern of SF7SA composite after sintered in air atmosphere at 1623K for 5h.

For the sake of comparison, Figure 29 also shows the peaks associated to the expected composite components. No peaks suggesting the formation of additional phases were detected. The calculated density of SF7SA3 was ≈ 4,1 g/cm^3 very similar to the literature data. This indicates that the prepared membranes are expected to be relevant for further hydrothermal modification and oxygen permeation studies. [59]

The results of SEM analysis also confirmed the formation of the two phases as shown in Figure 30.

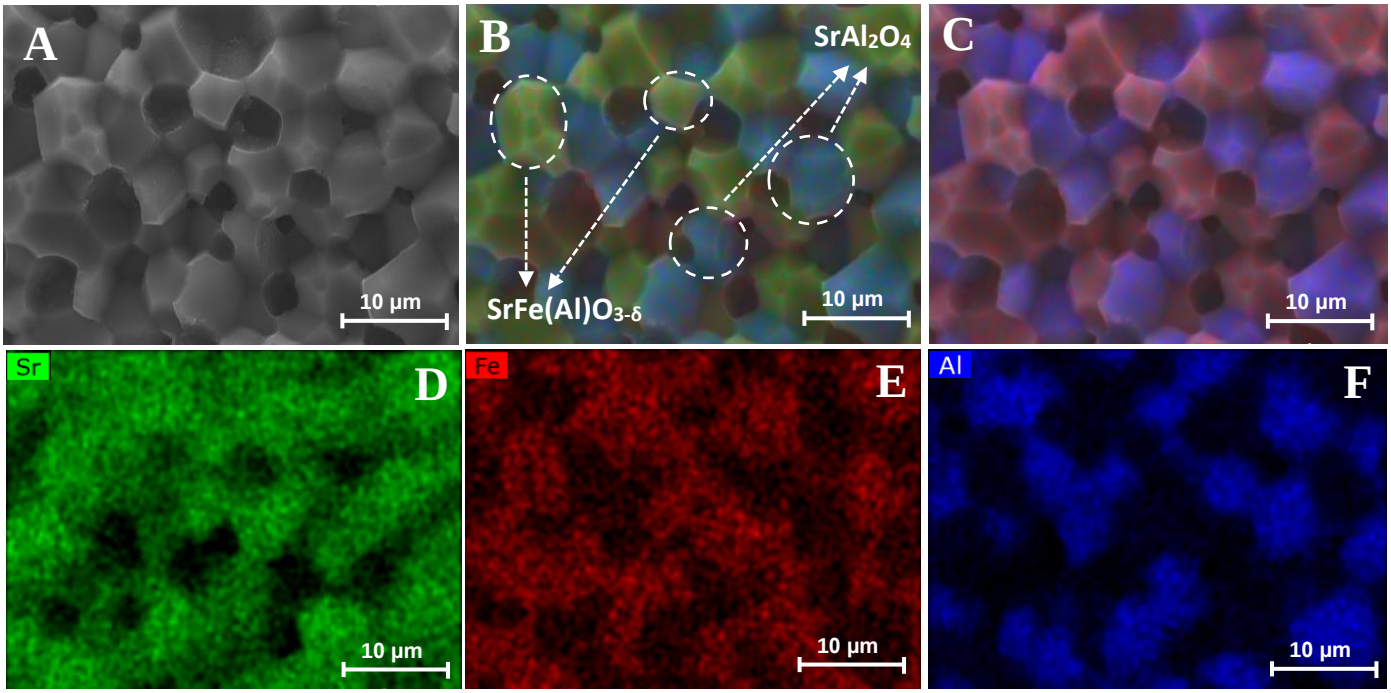

Figure 30 - SEM micrographs and EDS mapping results for sintered SF7SA3 composite membrane. (A) SEM SF7SA3, (B-F) EDS maps showing the distribution of various elements.

The expected phases are identified in Figure 30.B. Iron is present only in perovskite-type grains, facilitating the phase identification. Both phases are uniformly dispersed in the ceramic. Some areas in Figure 30.D suggest the apparent absence of strontium. The reason is the depth caused by detachment of some membrane grains through his grain boundary.

3.1.3. Thermal expansion

In the view to the applicability of the membranes in realistic industrial process conditions these membranes must have good mechanical stability, and consequently thermomechanical behavior should be studied. Since the application on these membranes in industrial oxygen separation processes involves the integration into multicomponent systems requiring attachments of the membrane to the other constituting parts made of ceramic or metallic materials, thermal stresses can be induced in the involved materials challenging configuration and the layout of the membrane device. Figure 31 shows the dilatometric curves of SF7SA3 ceramic in air.

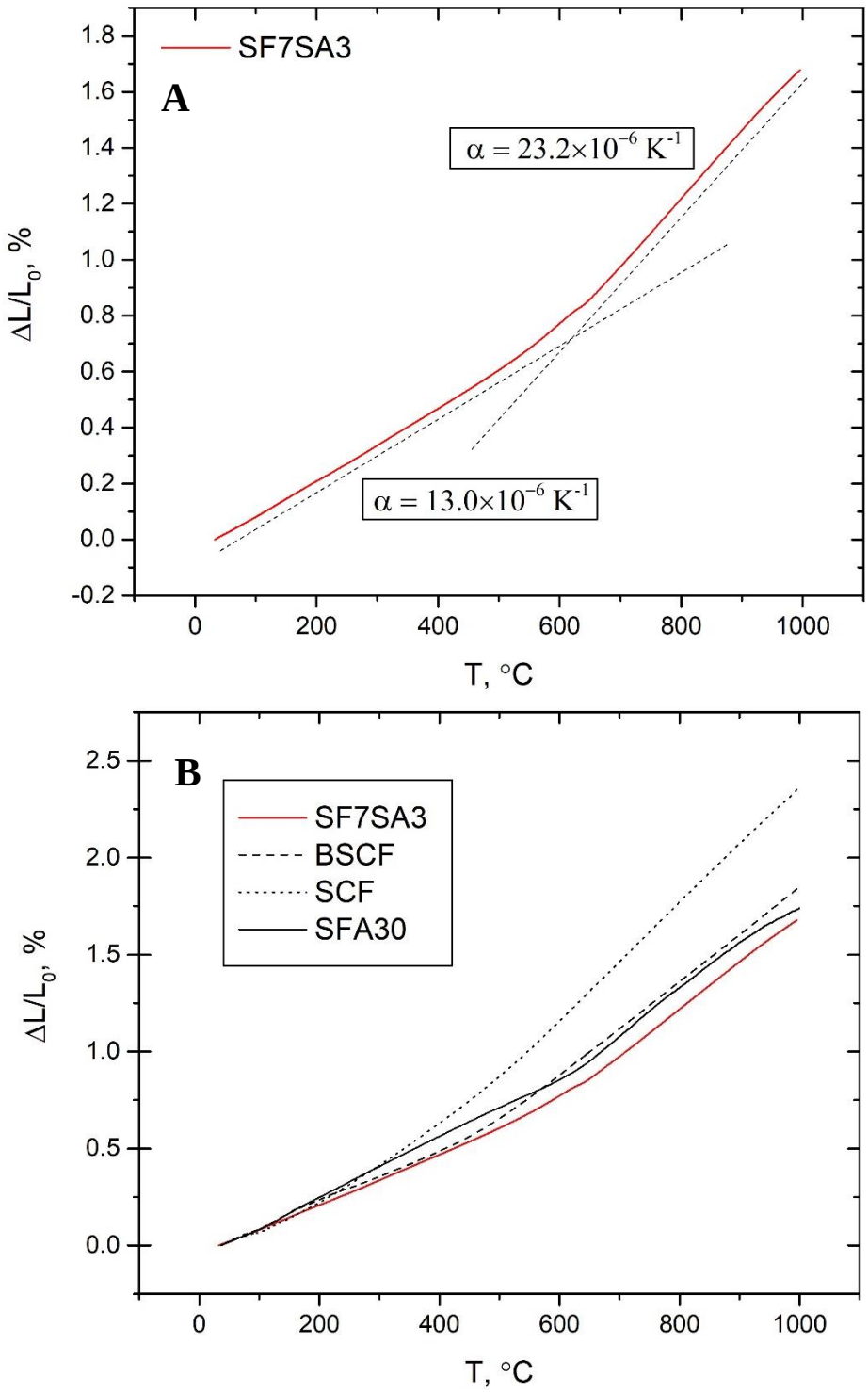

Figure 31 - (A) Dilatometric curve of SF7SA3 ceramics in air and illustration of calculations of average TEC values; (B) Comparison of thermal expansion of SF7SA3 ceramics with that of selected membrane materials: $Ba_{0.5}Sr_{0.5}Co_{0.8}Fe_{0.2}O_{3-\delta}$ (BSCF) [61], $SrFe_{0.7}Al_{0.3}O_{3-\delta}$ (SFA30) [54], $SrCo_{0.8}Fe_{0.2}O_{3-\delta}$ (SCF) [61]. L_0 is the sample length at room temperature in air.

SF7SA3 composite exhibits a non-linear thermal expansion behaviour upon heating in air to 1000 ºC (Figure 31.A). The dilatometric curve of SF7SA3 can be divided in two segments including the low-temperature range of 20-600 ºC and high-temperature range of 600-1000 ºC. The calculated average thermal expansion coefficients (TECs) correspond to 13.0×10^{-6} K^{-1} at lower temperatures and 23.2×10^{-6} K^{-1} in the high-temperature range.

The strong deviation from the linear expansion and change in the slope of dilatometric curve above ~600°C is due to contribution of chemical expansion originating from the changes in oxygen nonstoichiometry of the perovskite lattice. This reversible oxygen loss from the lattice at high temperatures are accompanied by the reduction of iron cations $Fe^{4+} \rightarrow Fe^{3+}$ inevitably causing an increase in their average ionic radius and additional chemically-induced expansion of the lattice seen above 600 ºC. [62] At lower temperatures, the oxygen content in the perovskite lattice is almost invariable, due to a frozen oxygen exchange, and the thermal expansion occurs solely due to anharmonicity of atomic vibrations.

As demonstrated in Figure 31.B the presence of the second phase $SrAl_2O_4$ with a moderate thermal expansion in the SF7SA3 composite favorably suppresses the thermal expansion compared to other membrane materials including single-phase SFA30 ($SrFe_{0.7}Al_{0.3}O_{3-\delta}$) perovskite-type ceramics. [63]

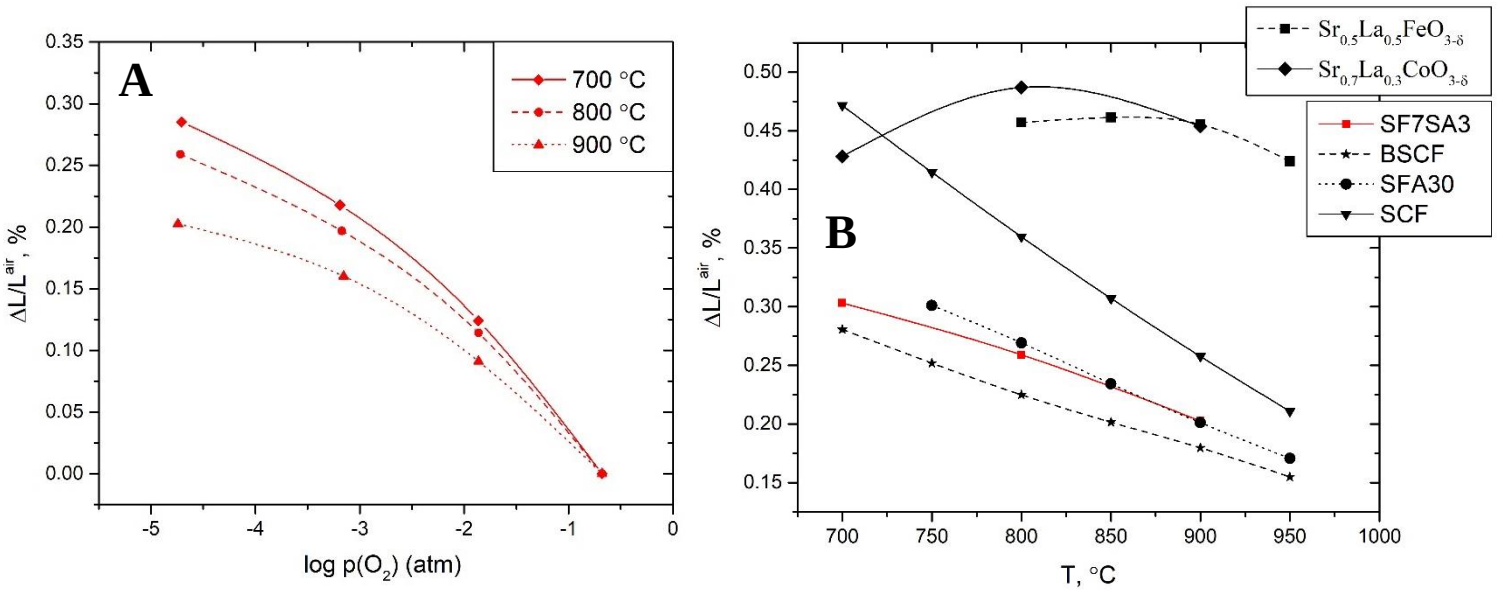

Figure 32 - (A) Chemical expansion of SF7SA3 on reducing oxygen partial pressure at 700-900 °C; (B) Comparison of chemical expansion of SF7SA3 on reducing $p(O_2)$ from atmospheric to ~5×10^{-5} atm with literature data for selected membrane materials under similar conditions. L^{air} is the sample length in air at given temperature. Literature data: $Ba_{0.5}Sr_{0.5}Co_{0.8}Fe_{0.2}O_{3-\delta}$ (BSCF) [61], $SrFe_{0.7}Al_{0.3}O_{3-\delta}$ (SFA30) [54], $SrCo_{0.8}Fe_{0.2}O_{3-\delta}$ (SCF) [61], $Sr_{0.5}La_{0.5}FeO_{3-\delta}$ [31] and $Sr_{0.7}La_{0.3}CoO_{3-\delta}$. [64]

Figure 32. A demonstrated chemical expansion of SF7SA3 composite on reducing oxygen partial pressure at 700-900 ºC. The chemically-induced expansion (or contraction) on $p(O_2)$ variations is a common phenomenon in perovskites and other oxide materials containing variable-valence cations. [61][65][66] Heating or reducing oxygen partial pressure at elevated temperatures causes reversible oxygen release from oxide lattice leading to the formation of oxygen vacancies. This is charge-compensated by the reduction of variable-valence cations (iron in the present case) with increase in their ionic radii. This leads to reversible lattice expansion on reduction and contraction on re-oxidation and may compromise the mechanical integrity of ceramics. Increasing temperature leads to a lower chemical expansion due to smaller variations in oxygen nonstoichiometry in the perovskite ferrite lattice at higher temperature. [62]

Figure 32.B compares the chemical expansion of SF7SA3 composite on reducing oxygen partial pressure from ambient to ~5×10^{-5} atm at 700-900 ºC with other potential membrane materials. The chemical expansion of SF7SA3 composite ceramics is

favorably lower compared to many single-phase ferrite and cobaltite perovskites. Furthermore, the presence of $SrAl_2O_4$, component with constant oxygen content makes it possible to suppress the chemical expansion of SF7SA3 compared to single-phase SFA30 ($SrFe_{0.7}Al_{0.3}O_{3-\delta}$) at 700-800 ºC.

Even though SF7SA3 exhibit a comparatively low chemical expansion, it is still challenging to use it in industrial processes. In this case any expansion is unpleasant since the sweep and feed side of the membrane will be under different atmospheres causing a different expansion and mechanical stresses across the membrane.

3.1.4. Electrical Conductivity

In MIEC membranes materials, total conductivity is defined as the sum of the ionic conductivity and electronic conductivity. These mixed conductors usually exhibit good electronic conductivity that typically exceeds the ionic conductivity by a few orders of magnitude. Although the level of the total conductivity should not be considered an indicator of potential oxygen permeability, it might give some additional helpful information about the membrane material as, for example, the presence or absence of percolation of conductive phase in composite samples. This, in turn, can affect the oxygen transport mechanism.

The total conductivity of SF7SA3 is predominantly p-type electronic. This is typical for perovskite-like ferrites, where the concentration of the charge carriers is strongly linked to the oxygen nonstoichiometry. [62] The latter can be represented by following reversible defect reaction, using a Kröger-Vink formalism. [21]

$$2Fe_{Fe}^{\bullet} + O_O^x \xrightarrow{heating} 2Fe_{Fe}^x + V_O^{\bullet\bullet} + 1/2O_2 \quad (16)$$

Where Fe_{Fe}^x and $Fe_{Fe}^{\bullet}$ denote Fe^{3+} and Fe^{4+}, correspondingly, and Fe^{4+} is equivalent to electron-hole localized on the iron cation. The oxygen diffusion, in turn, occurs due to the presence of oxygen vacancies $V_O^{\bullet\bullet}$. A gradual conductivity decrease with temperature increase originates from oxygen loss on heating accompanied by decreasing concentration of p-type charge carriers.

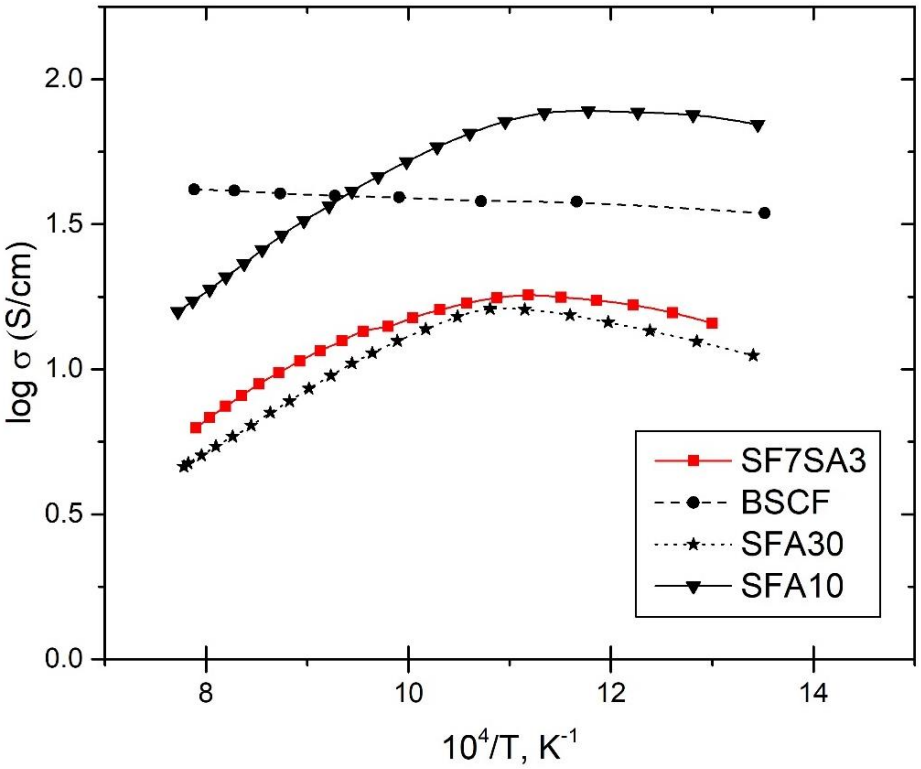

Figure 33 - Temperature dependence of total electrical conductivity of SF7SA3 composite. Literature data are shown for comparison: $Ba_{0.5}Sr_{0.5}Co_{0.8}Fe_{0.2}O_{3-\delta}$ (BSCF) [67], $SrFe_{0.7}Al_{0.3}O_{3-\delta}$ (SFA30) [54], $SrFe_{0.9}Al_{0.1}O_{3-\delta}$ (SFA10) [54].

Strontium aluminate exhibit predominant ionic conductivity with a minor contribution of p-type electronic conductivity under oxidizing conditions. [68] The total conductivity of $SrAl_2O_4$ is more than 4 orders of magnitude lower than that of SF7SA3 composite, which indicates that the total conductivity is dominated by the $SrFe(Al)O_{3-\delta}$ phase. [68] It is also evidenced by the fact that SF7SA3 composite exhibits total conductivity similar to single-phase $SrFe_{1-x}Al_xO_{3-\delta}$ perovskite. [58][59]

The behaviour of electrical conductivity of SF7SA3 composite is quite typical for perovskite-type including $SrFe_{1-x}Al_xO_{3-\delta}$ system. [62] The p-type electronic conductivity in these materials occurs by the small polaron hopping mechanism between iron cations. It shows semiconducting behaviour in the low-temperature range when the oxygen content in the perovskite lattice is fixed. In other words, electronic conductivity is thermally activated and increases on heating. An apparent transition to pseudometallic conductivity occurs on increasing temperature above ~620 °C. This happens due to oxygen losses from the lattice accompanied by a gradual decrease in the concentration of tetravalent iron cations and, therefore, p-type electronic charge carriers on heating, Equation (16).

Even though electronic transport dominates in SF7SA3, tuning the grain size can increase the contribution of the ionic conductivity. In particular larger grain size might have a positive effect on the ionic conductivity due to the lower concentration of grain boundaries, where the resistance to ionic transport may be higher than in the grain bulk. Thus, it is also important to adjust the procedure of glycine nitrate combustion in order to control the grain size.

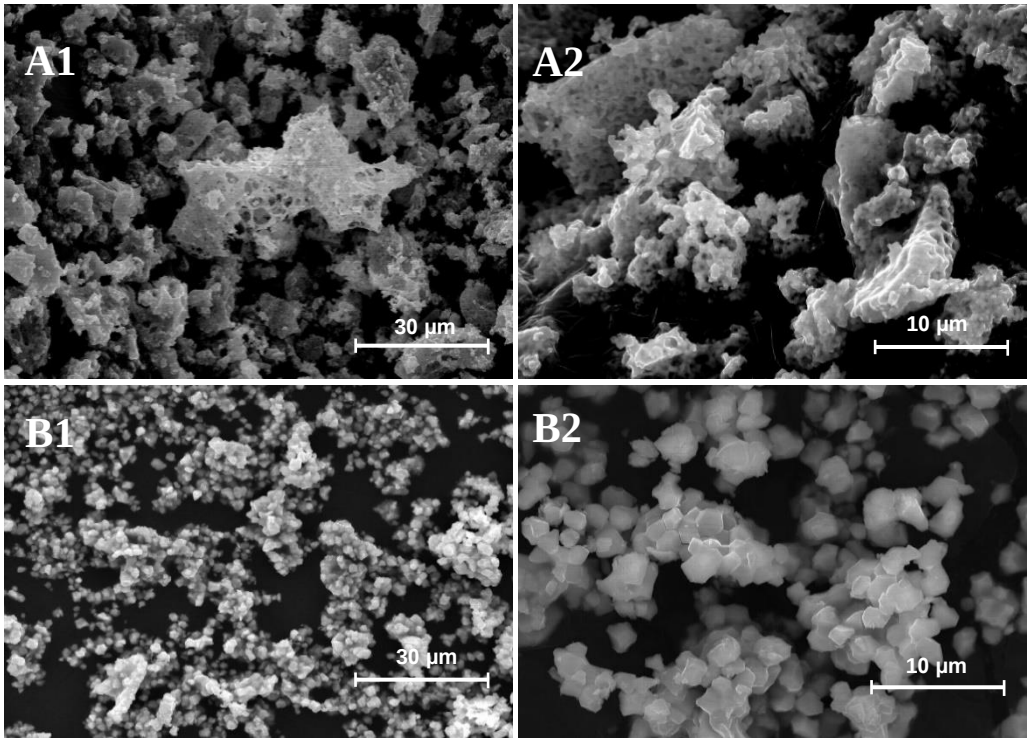

Figure 34 - SEM micrographs of the calcinated powder obtained after GNP synthesis (A1-A2); SEM micrographs of the obtained SF7SA3 powder from an annealed crashed pellet (B1-B2).

From Figure 34 is possible to see a drastic difference of the powder after annealing of the pellet. The calcinated powder obtained after GNP synthesis presents a porous grain with different grain sizes, contrary to the SF7SA3 powder generated by the annealed crashed pellet that presents a relatively uniform grain distribution size and grain size varying in the range 3–5 μm with established boundaries even though some agglomerates are present.

3.2. Hydrothermal processing

3.2.1. General aspects

The idea of this work considers the surface modification of the membrane to facilitate the oxygen exchange at the surface while not affecting the bulk ionic transport properties. As it was mentioned in the Section 3.1.1., an ideal model material to demonstrate the concept should allow attempting distinct modification approaches, providing more chances to succeed. This implies that the model material should withstand the hydrothermal conditions to permit the surface modification, and/or undergo a controlled reaction with the hydrothermal medium, desirably also leading to the favourable improvement of the surface exchange kinetics.

Figure 35 shows the Pourbaux diagrams for individual Sr-, Fe- and Al – water systems at 25º.

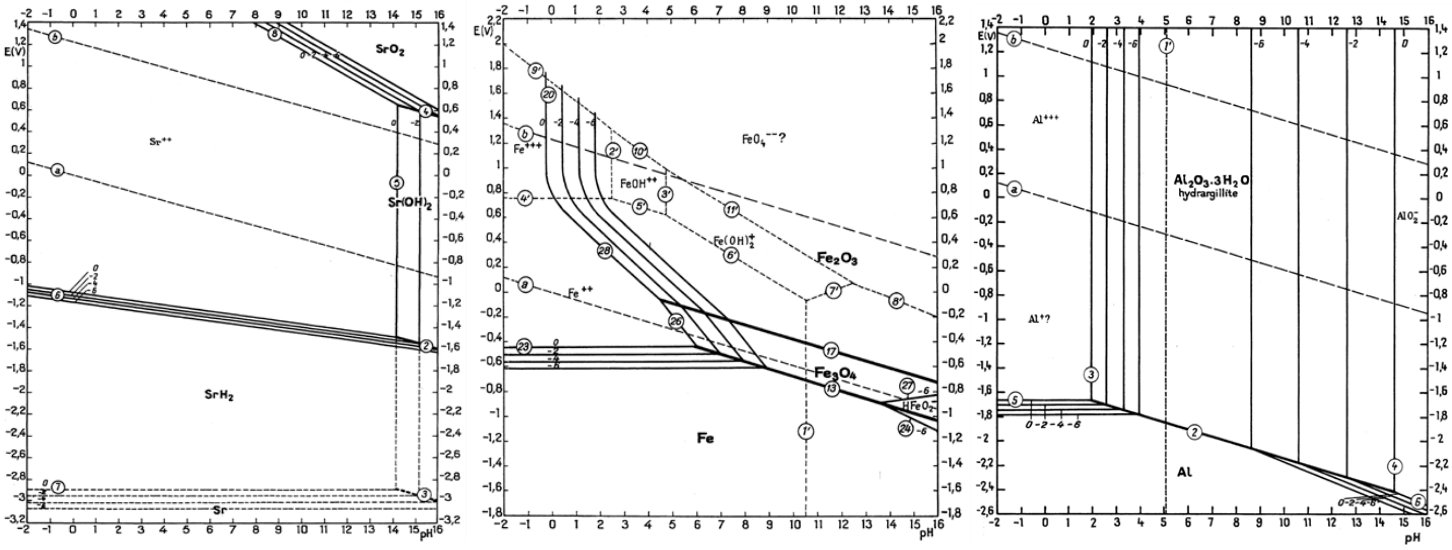

Figure 35 - Potential – pH equilibrium diagrams for strontium-water, iron-water, and aluminium-water systems at 25ºC. [69]

It should be noticed that these diagrams can provide only general guidelines regarding the aims of the present work, since they correspond to the ambient conditions, not taking into account the pressure and temperature in the hydrothermal reactor, and are related to thermodynamic equilibrium, while the effects to the interaction of membrane material with hydrothermal medium should be rather discussed in terms of kinetic mechanisms. Still, several important conclusions can be taken from these data. First,

complete membrane dissolution is expected under acidic conditions. Both Fe- and Al-containing solid species can be retained in the intermediate range of pH, while the significant dissolution of strontium can be only avoided under strongly alkaline conditions, which, in turn, are expected to lead to aluminium leaching. Thus, complete prevention of the interaction of the SF7SA3 membrane material with hydrothermal medium, especially at elevated temperatures, do not appear feasible. However, returning back to that discussed in the Section 3.1.1., the presence of aluminium is essential for good thermomechanical properties of the membrane, while also resulting in a moderate deterioration of the ionic transport properties. Thus, assuming that aluminium leaching would occur only at the membrane surface and the bulk integrity will be maintained, such leaching might be considered even as beneficial, since it might improve the ionic transport and, thus, oxygen surface properties. These arguments were used for the selection of the moderate and strongly alkaline conditions for hydrothermal processing. The selection of the temperature and treatment time range was made based on some preliminary tests and most common conditions used in conventional hydrothermal processing.

In the present work the hydrothermal treatment for surface activation was carried out using two approaches. A top-down type approach aimed at intentional partial leaching of the membrane surface in alkaline conditions to increase the surface area and to modify the chemical composition of the surface. In other words, the superficial dissolution of aluminium was expected to allow the formation of $SrFeO_{3-\delta}$ phase at the surface. The bottom-up type approach was focused on the deposition of praseodymium oxide on the membrane surface. This material is known for its high catalytic activity in electrochemical reactions involving molecular oxygen.[69] Both selected approaches are presented in Figure 36.

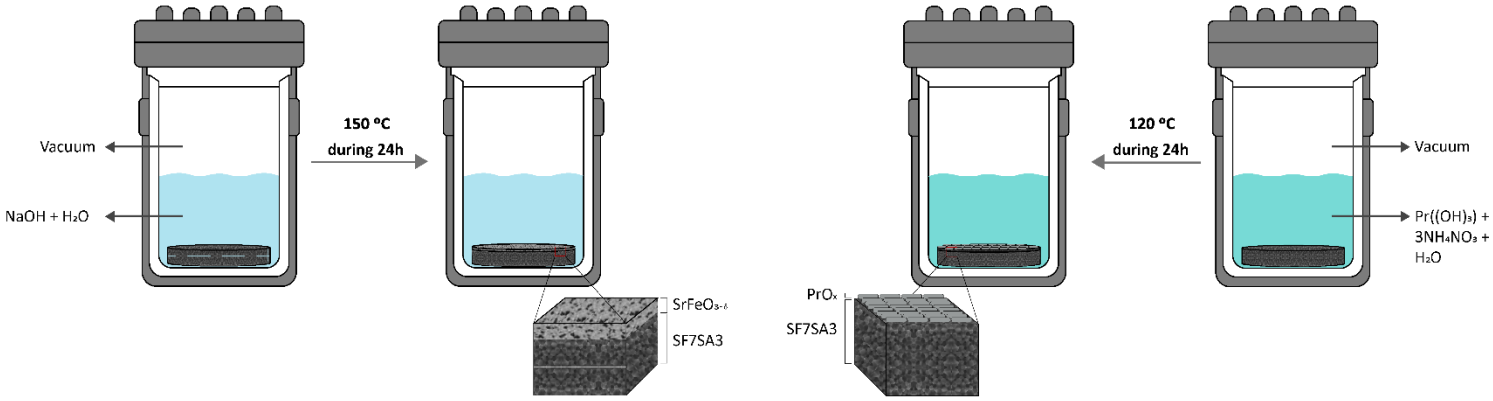

Figure 36 - Schematic Representations of the proposed surface modification approaches.

3.2.2. Top-down type approach

The effects provided by the hydrothermal treatment were studied as a function of molar alkali concentration, the temperature, and conditions of the final sintering step, which is required to transform the obtained surface layer, containing a significant fraction of the amorphous products, into a crystalline film with well-defined phase composition and favourable oxygen exchange kinetics. This step is unavoidable since MIEC membranes themselves are supposed to operate at high temperatures (i.e., above 600ºC).

The chemical mapping results for the membrane surface layer, obtained by hydrothermal treatment at 150ºC for 24h in 1 M NaOH, are shown in Fig. 37. It is clearly possible to see the formation of iron-enriched layer on the surface of SF7SA3 membrane due to almost complete etching of aluminium. This layer presents a thickness of ≈ 30 μm and is more porous that bulk SF7SA3, appearing promising for the surface activation while not compromising the integrity of the whole membrane.

Even though the etching appears successful, the formation of strontium-rich layer on the top of the modified layer is not expected to be favourable for the surface activation. Strontium is not a redox-active cation and thus, should rather block the oxygen transport and exchange. These species shown in Figure 37. (A,F) are likely formed due to remaining strontium hydroxide, which was not removed by the etching. Etching of Al from $SrFe(Al)O_{3-\delta}$ results in a shift of the A:B site ratio in perovskite ABO_3 lattice, namely, in strontium excess increasing on leaching. This Sr-reach species eventually form the surface layer on the top of the membrane, as shown in Figure 37. After contact with air atmosphere, this layer is immediately transformed in strontium carbonate.

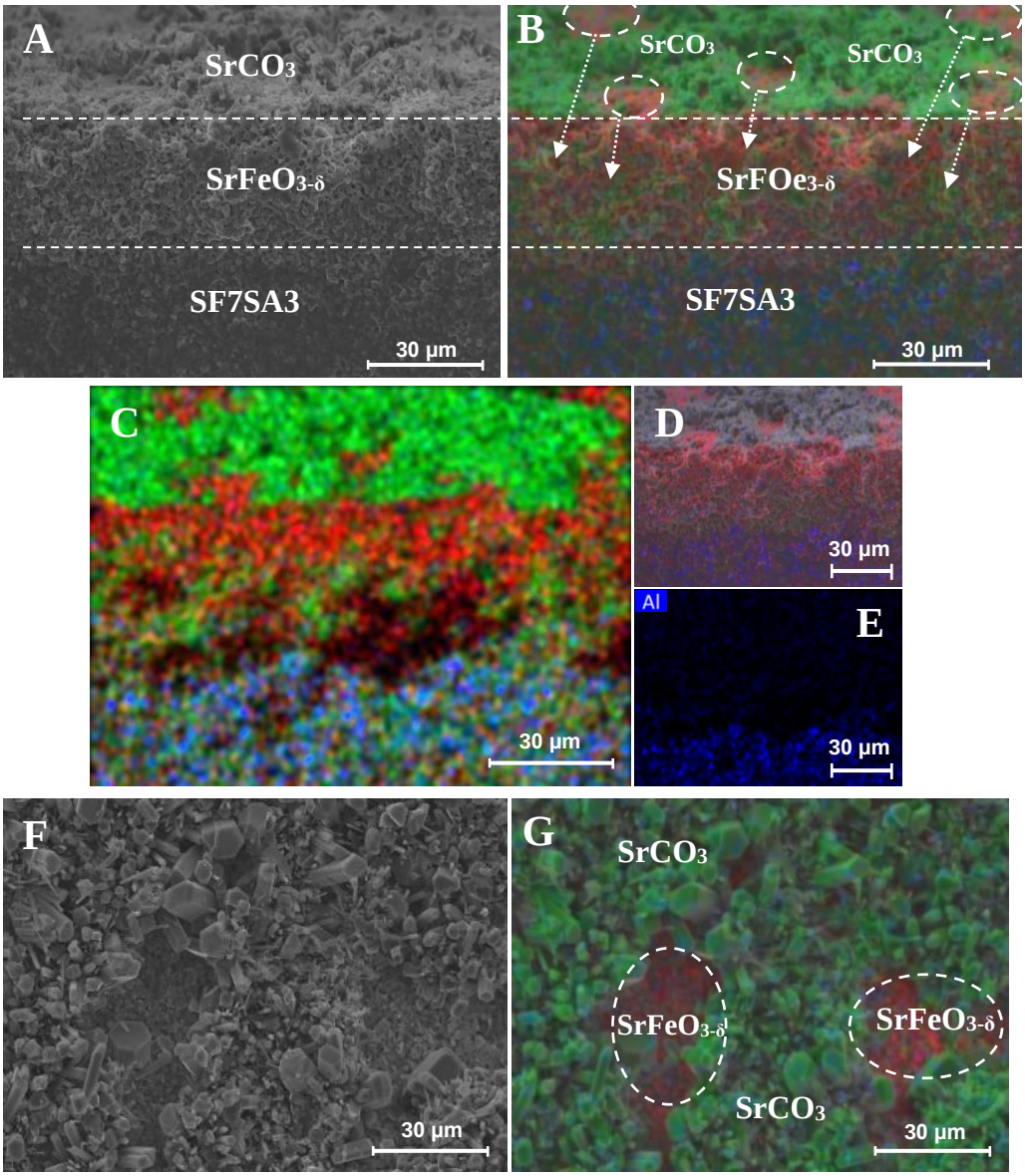

Figure 37 - SEM micrographs of SF7SA3 membrane after hydrothermal treatment with 1M NaOH at a temperature of 150ºC for 24 hours: (A) Cross-section (SEM), (B-E) Cross-section of EDS maps showing the distribution of various elements, (F) Surface view (SEM), (G) Surface view of EDS maps showing the distribution of various elements.

The images 37.F and 37.G clearly show how these species are blocking the membrane surface, leaving only some exposed iron-enriched islands, which look favourable for the surface activation. Still, one may assume that the Sr-enriched species might not impede completely the oxygen diffusion to/out from the surface, since they are quite porous. Corresponding analysis of the modified membranes after thermal post-

treatment at 650 ºC is shown in Figure 38. The surface structure, promoted by the hydrothermal processing, remains, together with Sr-enriched top layer. The results of the XRD analysis and semi-quantification of the phases (Fig. 38) give more guidelines about the surface composition.

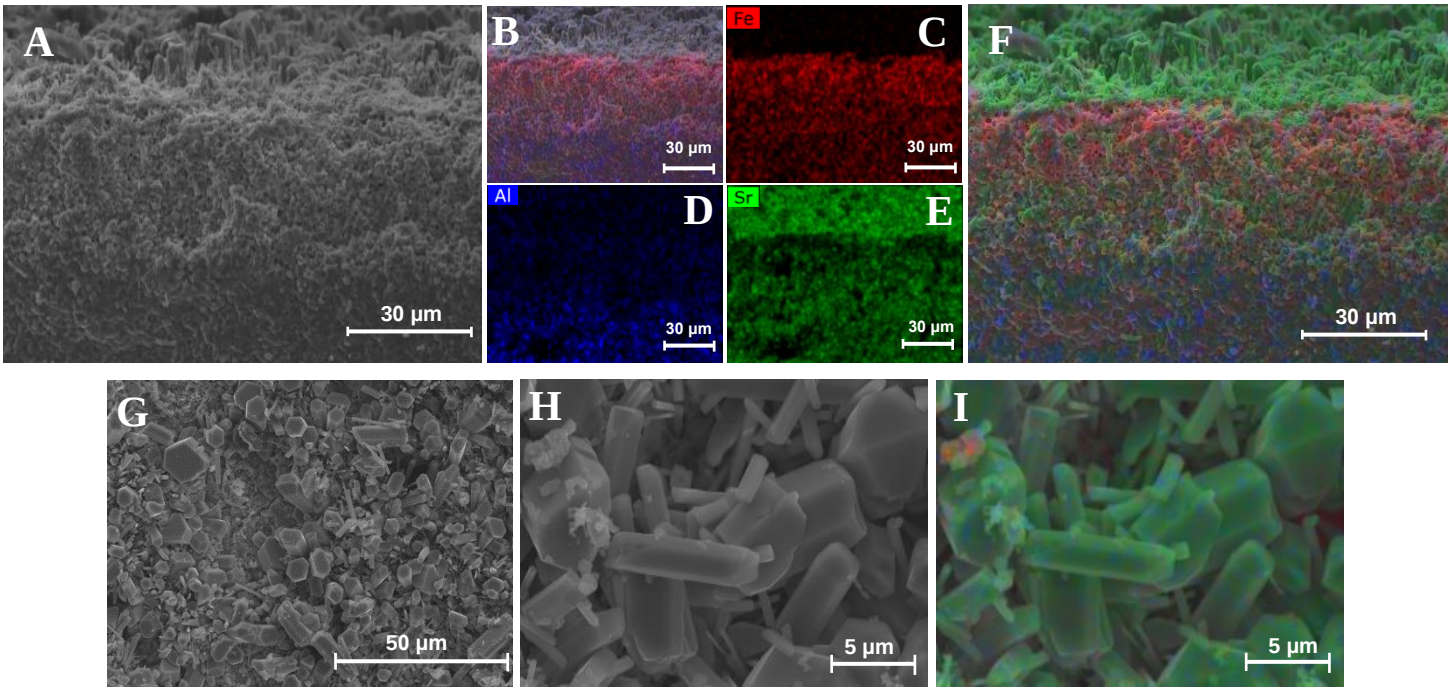

Figure 38 - SEM micrographs of SF7SA3 membrane after hydrothermal treatment with 1M NaOH at a temperature of 150ºC for 24 hours followed by an annealing of 650ºC: (A) Cross-section (SEM), (B-F) Cross-section of EDS maps showing the distribution of various elements, (G-H) Surface view (SEM), (I) Surface view of EDS maps showing the distribution of various elements.

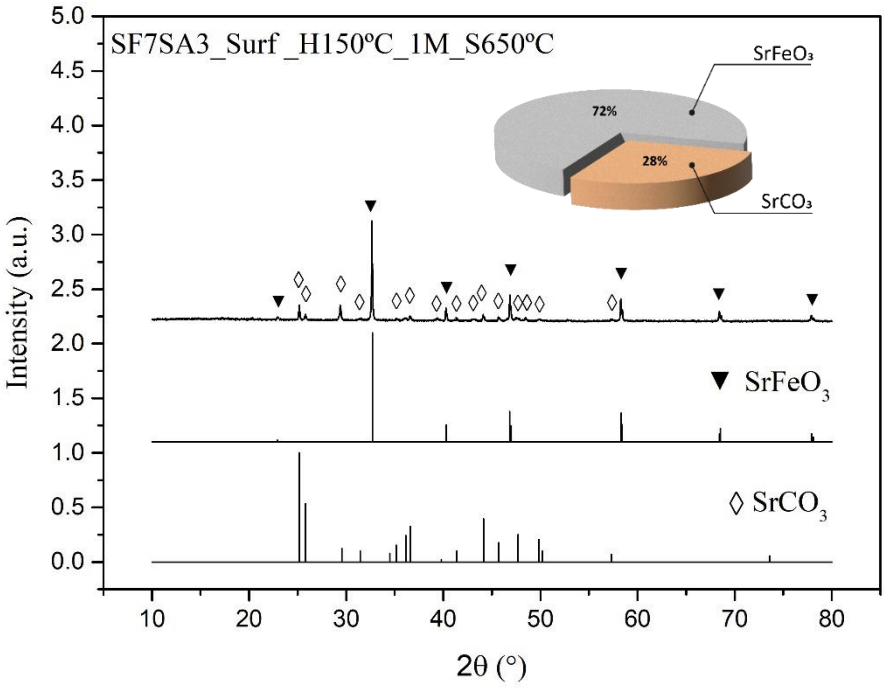

Figure 39 - XRD pattern of SF7SA3 surface and respective phases after hydrothermal treatment with 1M NaOH at a temperature of 150ºC for 24 hours followed by an annealing of 650ºC.

First, no peaks corresponding to $SrAl_2O_4$ phase were detected, confirming the XRD results are directly related to the layers produced by the hydrothermal treatment, but not to the membrane bulk. Secondly, the pattern shows that the surface is predominantly composed of $SrFeO_3$-based phase, probably still containing some amount of aluminium, but definitely less as compared to the $SrFe(Al)O_{3-\delta}$ grains in bulk, in accordance with the EDS mapping (Figure 38). This could be considered very relevant for further surface activation effect.

Decreasing pH is expected to facilitate the formation of soluble Sr-containing species, as suggested by the corresponding Pourbaux diagram (Figure 35). Thus, decreasing the molar NaOH concentration to 0.1 M was also attempted, assuming that the concomitant decrease in the aluminium etching rate will not be critical. Corresponding results are shown in Figure 40. The general mechanism appears essentially the same, leaving an etched iron-enriched layer covered with Sr-containing species. As it might be expected, the thickness of the iron rich layer has decreased to 15 μm, instead of 30 μm as seen for the preciously higher molar concentration. The Sr-rich particles appear larger, while been presented in smaller quantities, leaving a larger fraction of $SrFeO_{3-\delta}$ uncovered for oxygen activation.

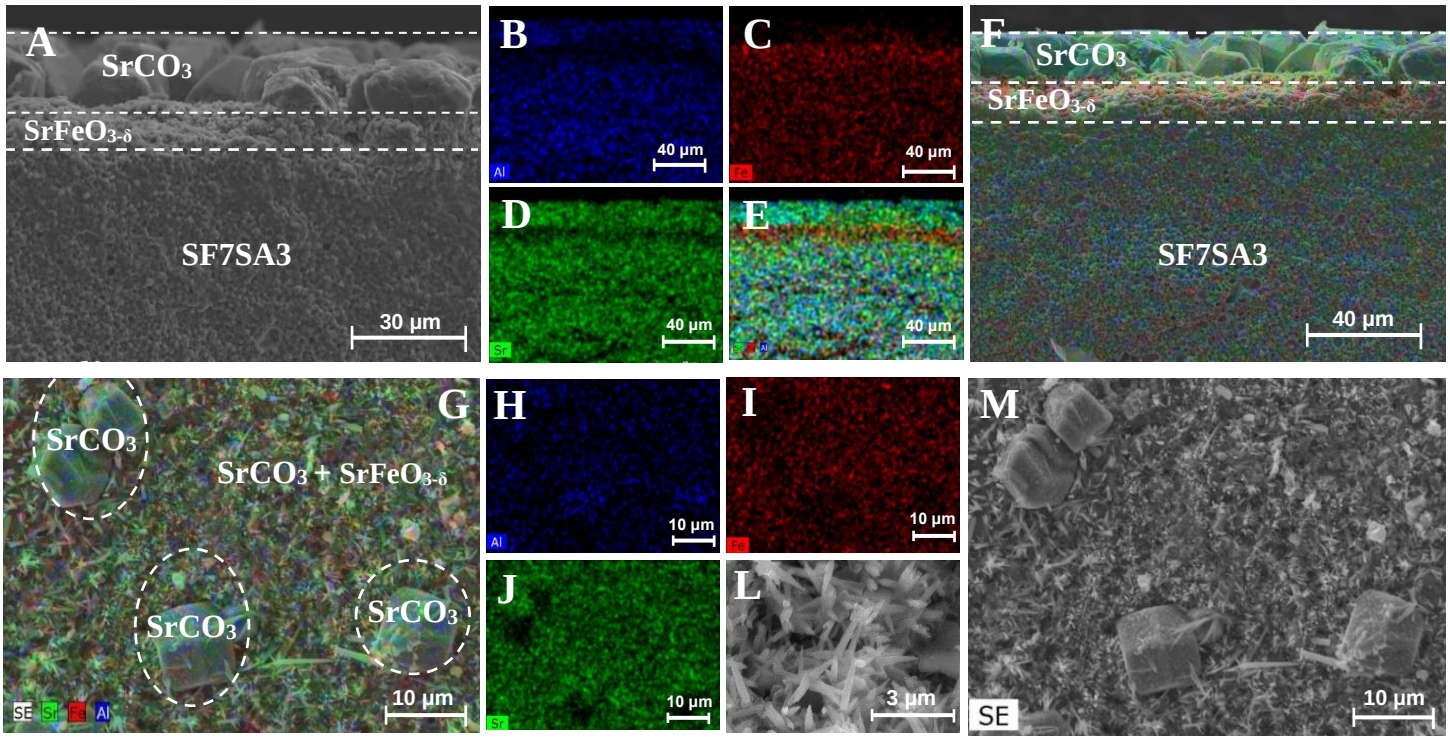

Figure 40 - SEM micrographs of SF7SA3 membrane after hydrothermal treatment with 0.1M NaOH at a temperature of 150ºC for 24 hours: (A) Cross-section (SEM), (B-F) Cross-section of EDS maps showing the distribution of various elements, (G-J) Surface view of EDS maps showing the distribution of various elements, (L-M) Surface view (SEM).

A quite similar situation is also observed after thermal post-treatment (Figure 41), resulting in well-defined $SrCO_3$ blocks which, however, appear less critical in terms of the surface blocking as compared to the above case of 1 M NaOH. In Figure 41.J, the mark of the tweezers on the membrane surface, left while handling the sample, is clearly seen that the created etched layer is very fragile, and a thermal post-treatment process is required to impart good adhesion with the SF7SA3.

Surprisingly, the XRD analysis of the membrane surface (Figure 42) reveals more $SrCO_3$ phase as compared to 1 M NaOH case.

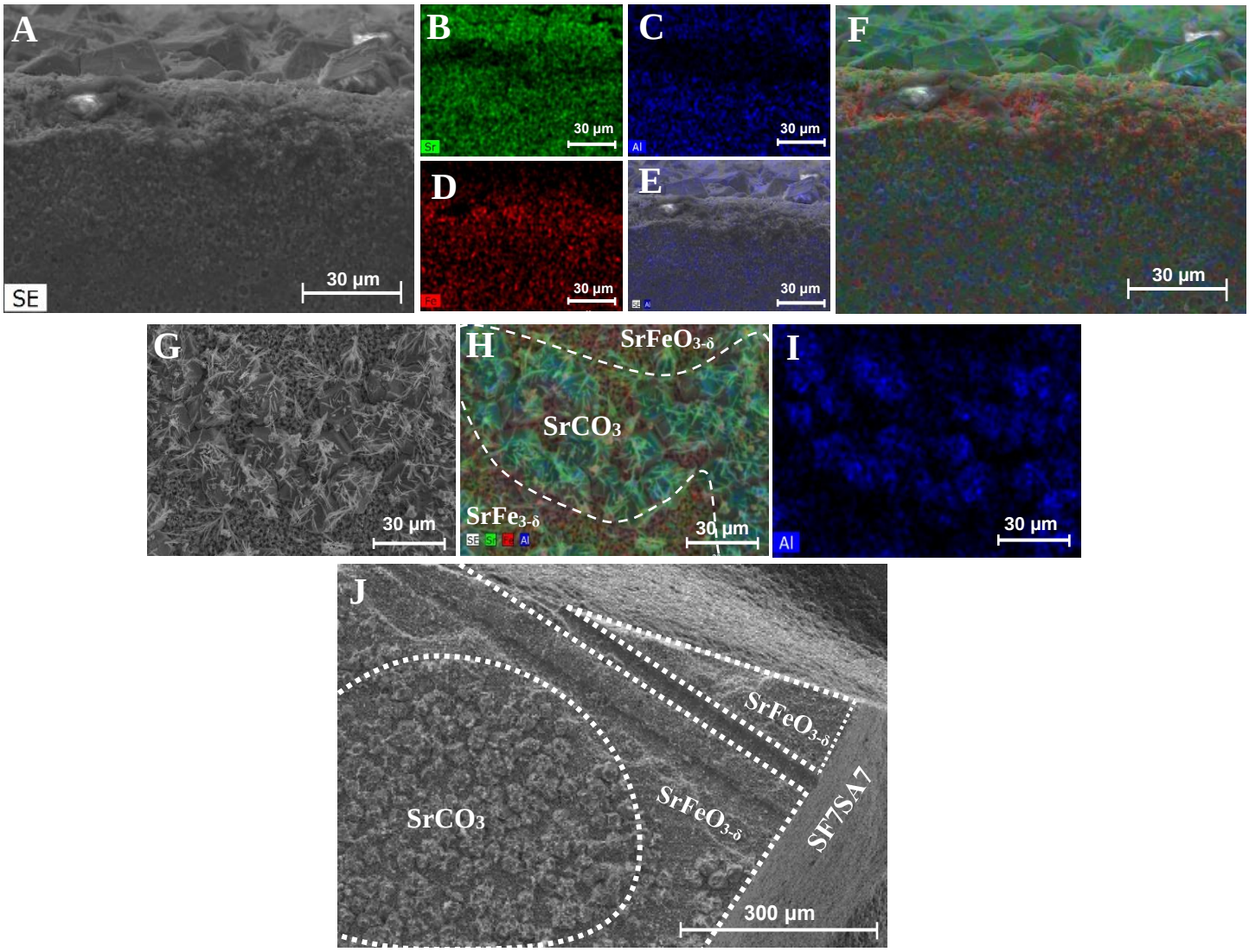

Figure 41 - SEM micrographs of SF7SA3 membrane after hydrothermal treatment with 0.1M NaOH at a temperature of 150ºC for 24 hours followed by an annealing of 650ºC: (A) Cross-section (SEM), (B-F) Cross-section of EDS maps showing the distribution of various elements, (G, J) Surface view (SEM), (H-I) Surface view of EDS maps showing the distribution of various elements.

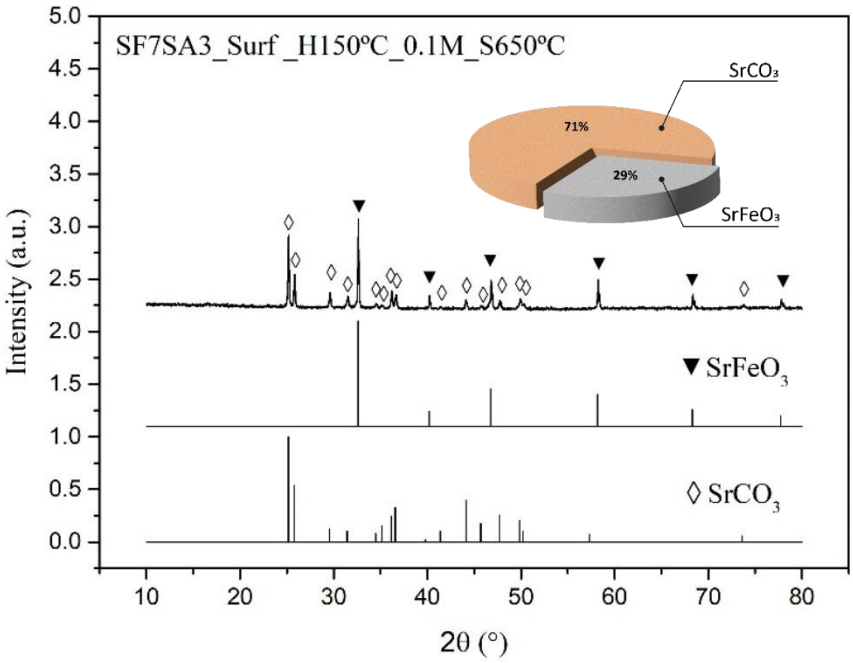

Figure 42 - XRD pattern of SF7SA surface and respective phases after hydrothermal treatment with 0.1M NaOH at a temperature of 150ºC for 24 hours followed by an annealing of 650ºC.

The reasons might be related to the presence of larger $SrCO_3$ particles and non-uniformity of the $SrCO_3$ covering layer.

Hydrothermal processing at higher temperature was also attempted, to assess the kinetic effects on the membrane modification. For this, the lowest 0.1 M NaOH concentration was used at 180ºC for 24 h. This increase intensified the appearance of $SrCO_3$ at the membrane surface. From Figure 43. (B, D), it can be seen that this layer is thicker and appears rather dense, with thin $SrCO_3$ nanorods well packed and blocking all the available surface. Corresponding XRD studies of the surface layer (Figure 43) also suggest the presence of a significant fraction of $SrCO_3$, along with desirable $SrFeO_3$.

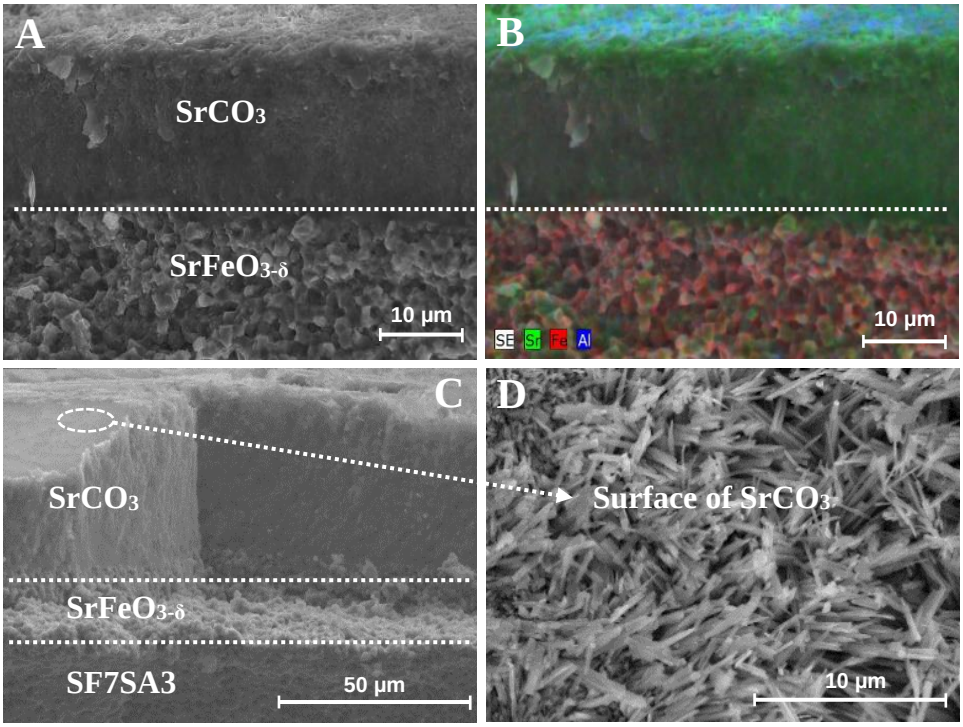

Figure 43 - SEM micrographs of SF7SA3 membrane after hydrothermal treatment with 0.1M NaOH at a temperature of 180ºC for 24 hours followed by an annealing of 650ºC: (A, C) Cross-section (SEM), (B) Cross-section of EDS maps showing the distribution of various elements, (G) Surface view (SEM).

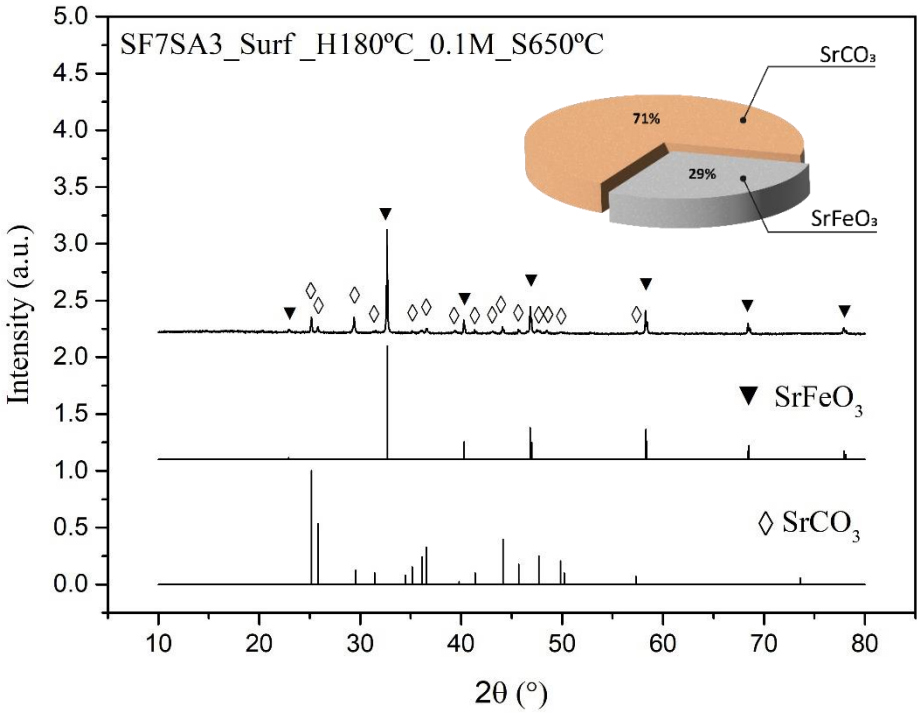

Figure 44 - XRD pattern of SF7SA surface and respective phases after hydrothermal treatment with 0.1M NaOH at a temperature of 180ºC for 24 hours followed by an annealing of 650ºC.

Time and thermal post-treatment conditions were also varied in the present work. However, these results are not presented since the corresponding effect on the composition and morphology of the surface layer was rather minor.

In general, the obtained results suggest that selective etching of aluminium from the surface layer under hydrothermal conditions is possible without compromising the integrity of the whole membrane. As a result, the $SrFeO_3$-based layer is formed after the thermal post-treatment, which is expected to boost the surface oxygen exchange. At the same time, the formation of Sr-rich species and their morphology depends on the hydrothermal conditions applied, as demonstrated in this section. Still, additional optimisation, preferably supported with the data on oxygen permeation, is required to assess how critical those species could be for the oxygen surface exchange process. Additional surface modification approaches described in the next section were attempted.

3.2.3. Additional surface modification approaches

Two strategies were attempted to improve the results of the top-down type approach, aiming either complete or partial removal of Sr-rich blocking species from the surface or transforming them into a material with a notable surface oxygen exchange activity.

The first strategy relied on treatment with a weak acid to dissolve $SrCO_3$, while leaving the $SrFeO_{3-\delta}$ layer more exposed. The idea is in accordance with that expected from Pourbaux diagram (Figure 35). Although such treatment may also result in partial leaching of iron, this is expected to be supressed by the fact that the $SrFeO_{3-\delta}$ layer, formed by etching of Al, is well attached to the SF7SA3 bulk and presents less porosity, while the surface Sr-rich layer is likely formed by the re-deposition process and is more porous and less mechanically strong. Thus, acetic acid (0.1 M) treatment was applied to the membrane right after hydrothermal treatment, as is demonstrated in Figure 45.

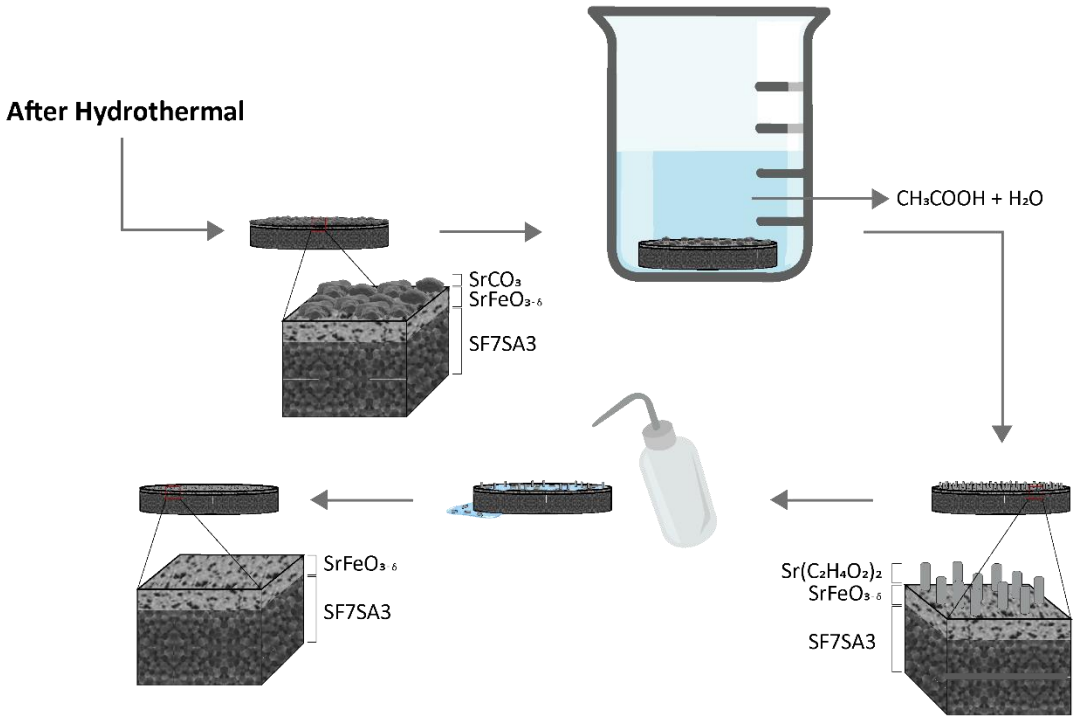

Figure 45 - Schematic representation of the acetic acid treatment.

The reactions that are expected to occur include:

$$SrCO_3 + 2CH_3COOH \rightarrow Sr(CH_3COO)_2 + CO2 + H_2O \quad (17)$$

$$Sr(OH)_2 + 2CH_3COOH \rightarrow Sr(CH_3COO)_2 + H_2O \quad (18)$$

The resultant strontium acetate is readily soluble and is expected to be easily removed by washing it with water.

Corresponding SEM micrographs and EDS mapping results are presented in Figure 46.

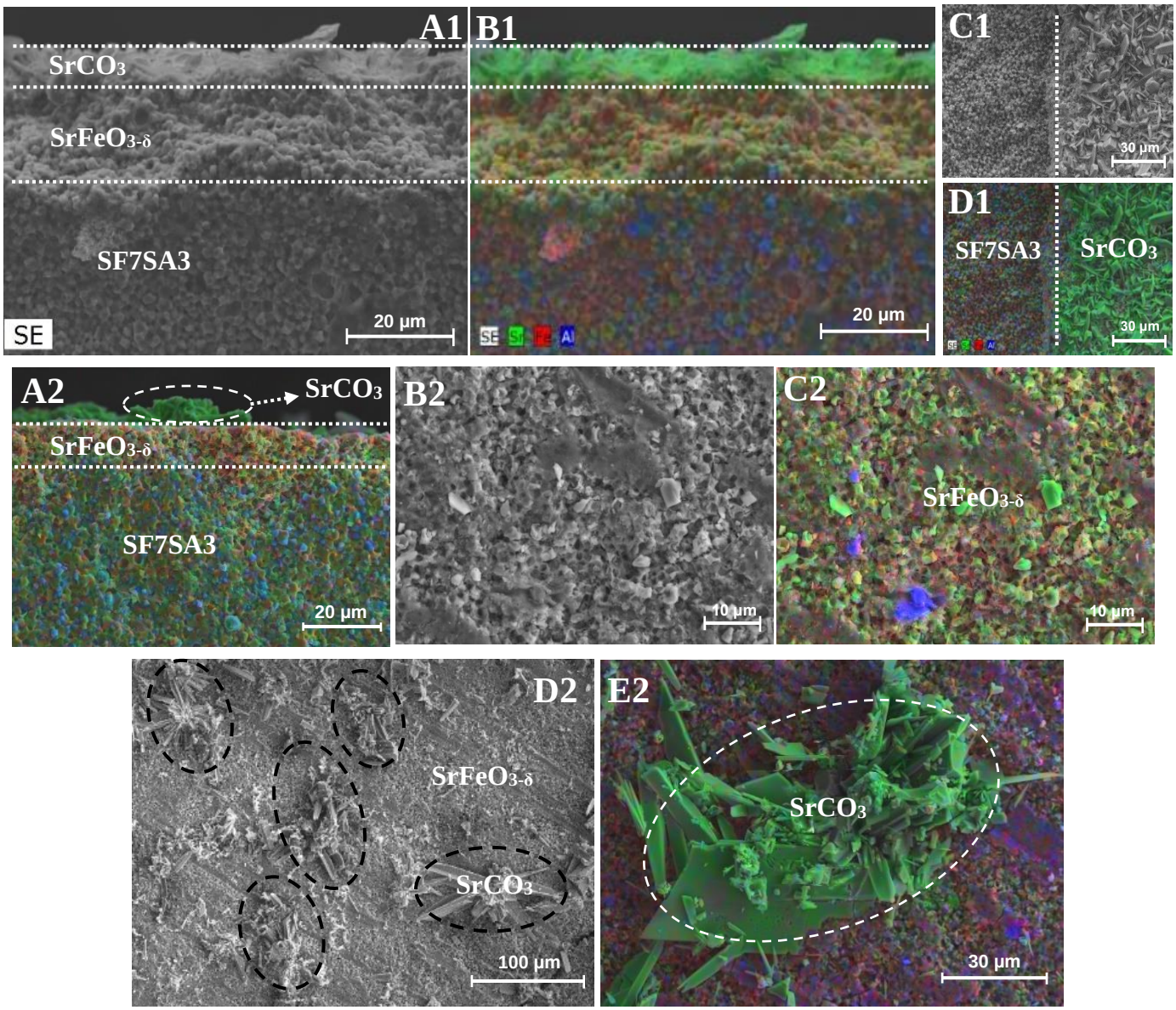

Figure 46 - SEM micrographs of SF7SA3 membrane - after hydrothermal treatment with (1) 0.1M NaOH and (2) 1M NaOH and at a temperature of 150ºC for 24 hours followed by an annealing of 650ºC with a posterior acetic acid treatment at the surface: (A1) Cross-section (SEM), (B1, A2) Cross-section of EDS maps showing the distribution of various elements, (C1, B2, D2) Surface view (SEM), (D1, C2, E2) Surface view of EDS maps showing the distribution of various elements.

The observed results unambiguously suggest at least partial removal of the Sr-rich species from the membrane surface. Although large $SrCO_3$ particle still remain at the surface, the removal readily progresses when the concentration of acetic acid is increased to 1 M (Figure 46 (C2, D2)). Again, more detailed optimisation of the additional treatment parameters is required if aiming at a complete $SrCO_3$ dissolution. Successful dissolution of the Sr-rich species is also validated by the XRD results shown in Figure 47, where essentially $SrFeO_{3-\delta}$ was found at the surface.

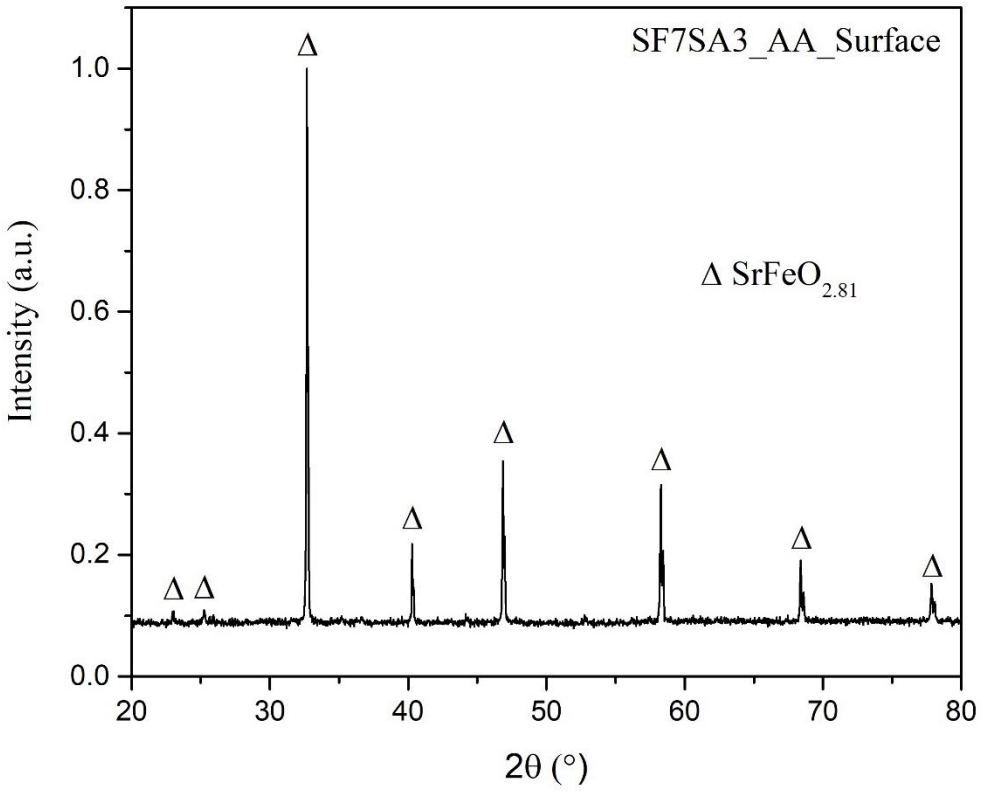

Figure 47 - XRD surface pattern of SF7SA3 membrane after hydrothermal and acetic acid treatments.

It is worth noticing that relatively small surface coverage with $SrCO_3$ is not expected to significantly affect oxygen transport. However, some reference values are required to quantify this contribution. A rough quantitative estimation of the $SrCO_3$ surface coverage has been done with "ImageJ" program by assuming one of the worst cases shown in the image Figure 46.D2 and the areas of the corresponding exposed $SrFeO_{3-\delta}$ and $SrCO_3$ zones. It shows that, in this particular case, $SrCO_3$ covers roughly 13% of the membrane surface, while actually less surface area might be blocked. The porosity and weak surface attachment of the $SrCO_3$ also facilitate oxygen diffusion and surface exchange.

Although the complete dissolution of $SrCO_3$ from the membrane surface by acetic acid post-treatment appears promising to improve the results of the top-down type approach, taking an opposite direction in this route is also possible. Another approach considered a possibility to compensate strontium excess at the surface is by combining it with iron, eventually forming $SrFeO_{3-\delta}$ after thermal post-treatment. For this, an introduction of iron nitrate $Fe(NO_3)_3.9H_2O$ precursor to the hydrothermal solution was attempted (Figure 48), aiming the formation of $Fe(OH)_3$ flakes at the surface, simultaneously with aluminium etching and formation of Sr-rich precipitates at the surface.

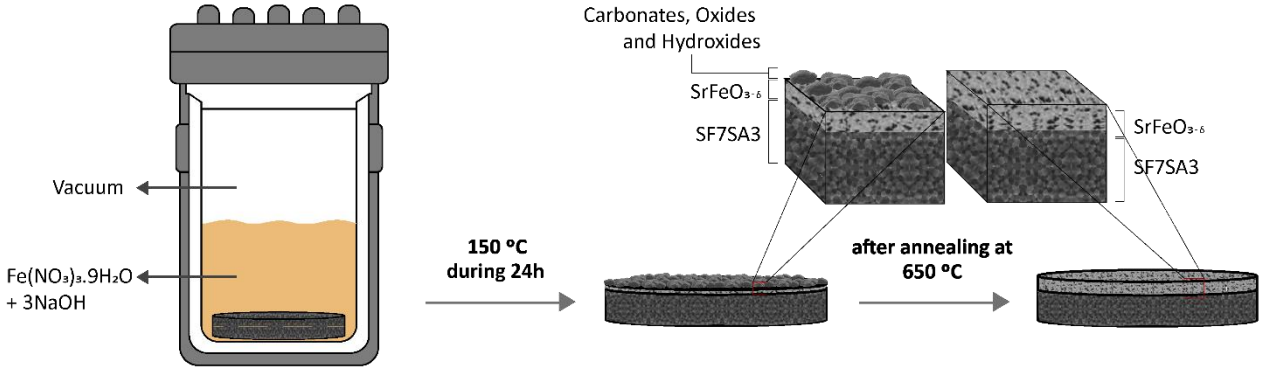

Figure 48 - Schematic representation of the iron nitrate introduction treatment.

Figure 49 shows the structure of the superficial layers formed after hydrothermal treatment at 150ºC using the addition of iron nitrate precursor, after applying thermal post-treatment at 650ºC. Although additional iron deposition at the membrane surface indeed proceeds, the iron-containing species are not well mixed strontium-containing counterpart, resulting in two separate $SrCO_3$ and Fe_2O_3 layers at the membrane surface.

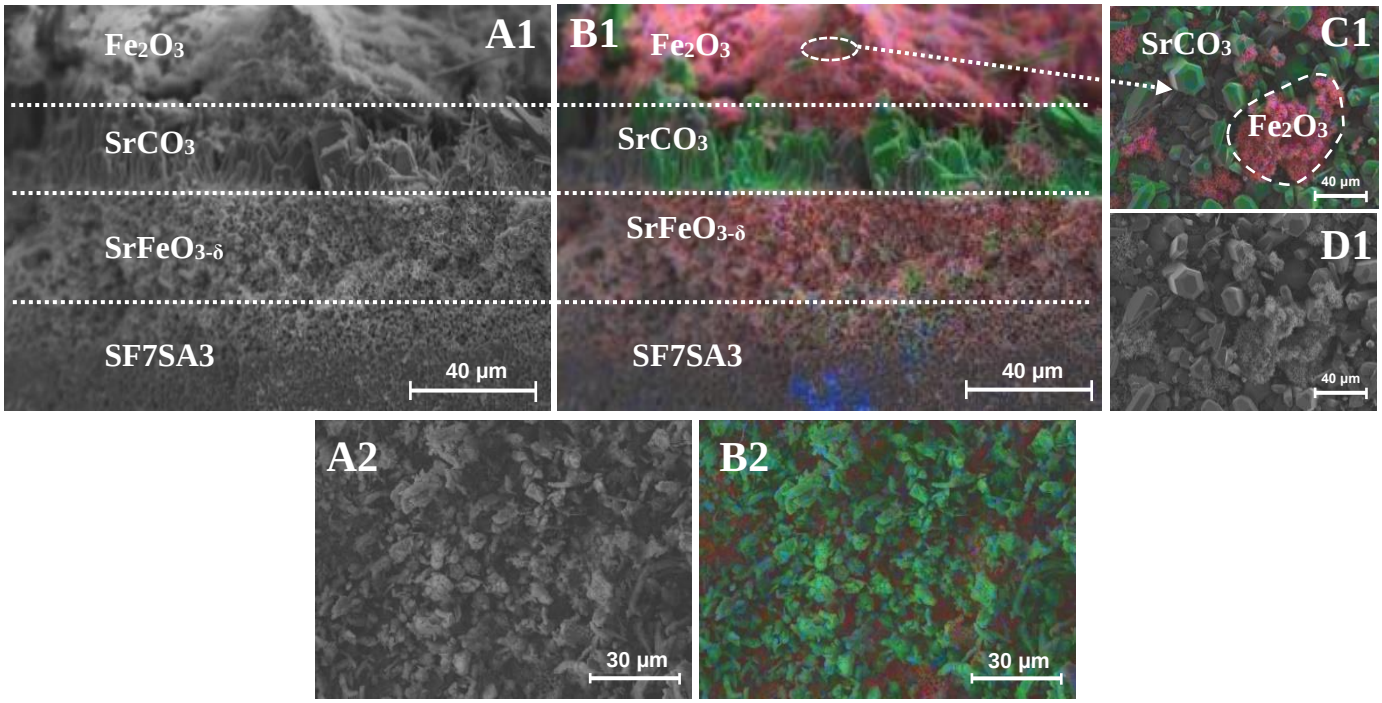

Figure 49 - 1) SEM micrographs of SF7SA3 membrane after hydrothermal treatment with 1M NaOH + $Fe(NO_3)_3.9H_2O$ at a temperature of 150ºC for 24 hours followed by an annealing of (1) 650 ºC and (2) 850 ºC : (A1) Cross-section (SEM), (B1) Cross-section of EDS maps showing the distribution of various elements, (D1, A2) Surface view (SEM), (B2) Surface view of EDS maps showing the distribution of various elements.

Absence of sufficient interaction is also confirmed by the results of the XRD analysis (Figure 50).

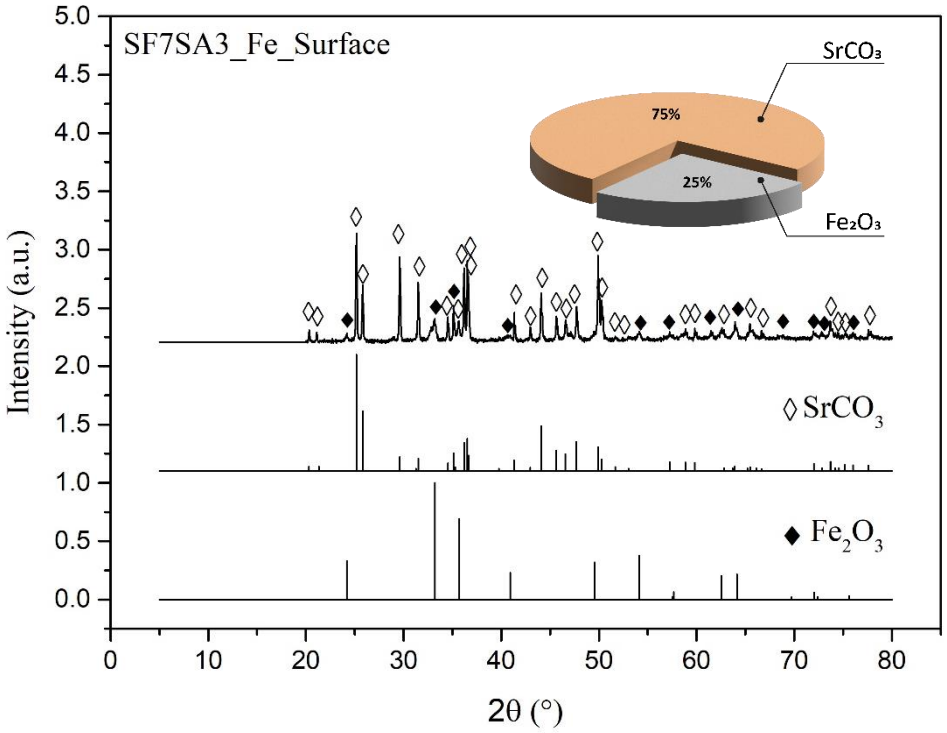

Figure 50 - XRD pattern of SF7SA surface and respective phases after hydrothermal treatment with 1M NaOH + $Fe(NO_3)_3.9H_2O$ at a temperature of 150ºC for 24 hours followed by an annealing of 650 ºC.

To promote the desired reaction, an attempt to increase the thermal post-treatment temperature up to 850 ºC was made. However, the following microstructural analysis (Figure 49. (A2, B2)) shows that the surface is still blocked with Sr-containing species, with likely negative effect on the oxygen permeation.

In general, although the approach of converting the Sr-rich species to the compounds that can activate the membrane surface towards oxygen exchange appears attractive, further optimisation is obviously needed. In particular, since the above results obtained after the thermal post-treatment at a higher temperature suggest the strontium excess is present and corresponding species are still blocking the surface, it might indicate that the amount of the deposited $Fe(OH)_3/Fe_2O_3$ is not sufficient to consume all $SrCO_3$.

A mechanical treatment with a small blade (Figure 51) was also made attempting a horizontally thinning on the surface of $SrCO_3$ to remove it and leave $SrFeO_3$, hopefully undamaged and uncovered for oxygen activation.

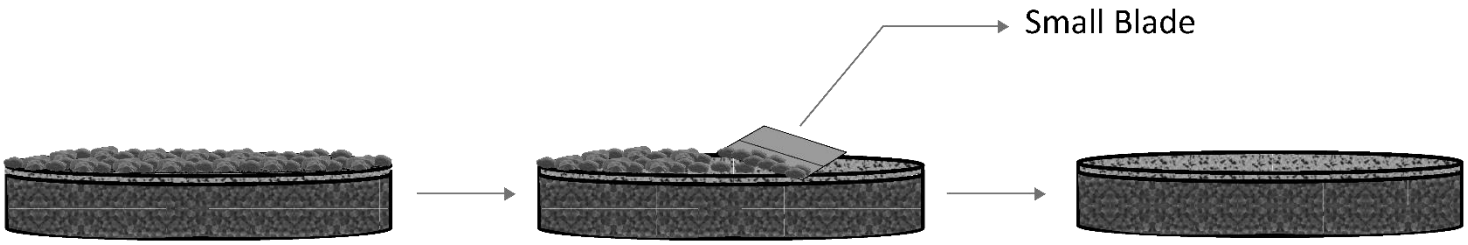

Figure 51 - Schematic representation of the mechanical treatment.

3.2.4. Bottom-Up type Approach

The bottom-up type approach implying the synthesis of catalytically active species at the membrane surface by hydrothermal treatment is expected to be somewhat universal for various membrane materials. Although the surface etching can still proceed, depending on the chemical properties of the membrane material and pH of the hydrothermal medium, the main effect here is expected from species synthesized on the surface. Praseodymium oxide (Pr_6O_{11}) is a good candidate for such modification .[70] The $Pr(NO_3)_3.9H_2O$ was the compound introduced in hydrothermal treatment in order to obtain a layer of praseodymium oxide on top of the membrane surface. After hydrothermal processing with Pr-containing species, the modified membrane was subjected to thermal post-treatment to form a mechanically and stable PrO_x layer for oxygen activation.

As a first approach, ammonium hydroxide was used as an alkaline medium to promote the deposition of PrO_x layer by a reaction with $Pr(NO_3)_3$. Corresponding procedures to synthesize praseodymium oxide and hydroxide nanoparticles with different shape are often described in the literature (e.g., [71]). As compared to strongly alkaline medium, NH_4OH is expected to be much less active towards etching the aluminium. The results of the microstructural characterization are shown on Figure 52. The results still suggest that some etching might occur and lead to the formation of Sr-rich surface layer. Surprisingly, this surface layer is also rich in aluminium, while also containing the desired PrO_x. The structure of the surface layer is better shown from the top (Figure 52. G). It is possible to see PrO_x particles and larger Sr-rich inclusion. In any case, the modification with praseodymium oxide is quite poor and non-uniform.

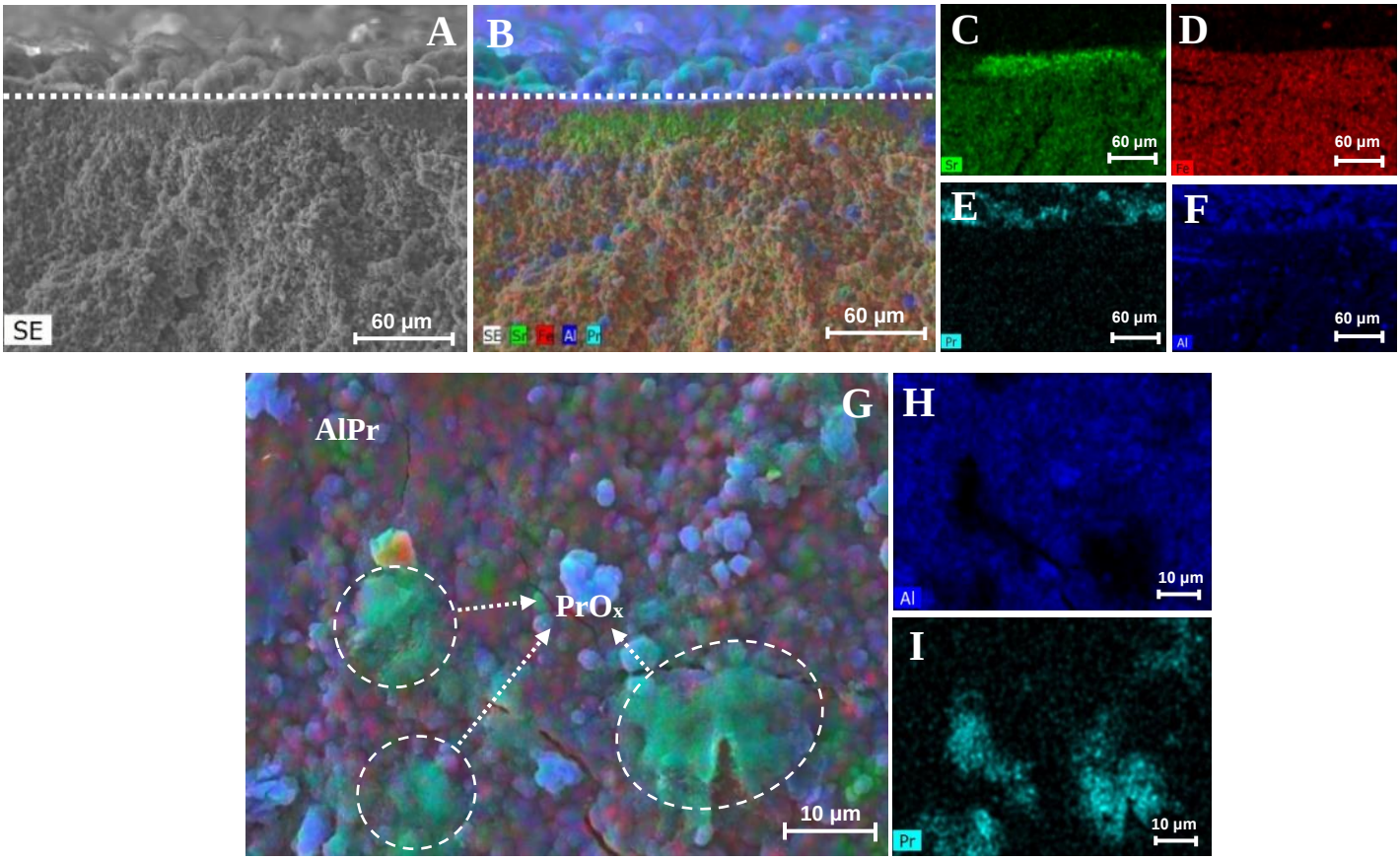

Figure 52 - SEM micrographs of SF7SA3 membrane after hydrothermal treatment with $Pr(NO_3)_3.9H_2O$ + NH_3 at a temperature of 120ºC for 24 hours followed by an annealing of 650ºC: (A) Cross-section (SEM), (B-F) Cross-section of EDS maps showing the distribution of various elements, (G-I) Surface view of EDS maps showing the distribution of various elements.

The accumulation of excessive aluminium is probably associated with "intermediate" alkaline conditions, which, while still promoting some aluminium etching from the membrane, are insufficient to promote its full dissolution and lead to $Al(OH)_3$ instead. Ammonia is also known as a strong complexing agent for transition metal cations, like Fe^{3+}. Thus, partial enrichment in aluminium might also be linked to the etching of the iron cations. Additional studies are required to establish the relevant mechanisms behind the observed microstructural evolution.

Based on these results, further modification with PrO_x was performed again using NaOH as the base for the hydrothermal processing. As compared to NH_4OH, NaOH is

expected to lead to more massive precipitation of $PrO_x/Pr(OH)_3$ species. Corresponding results are shown in Figure 53.

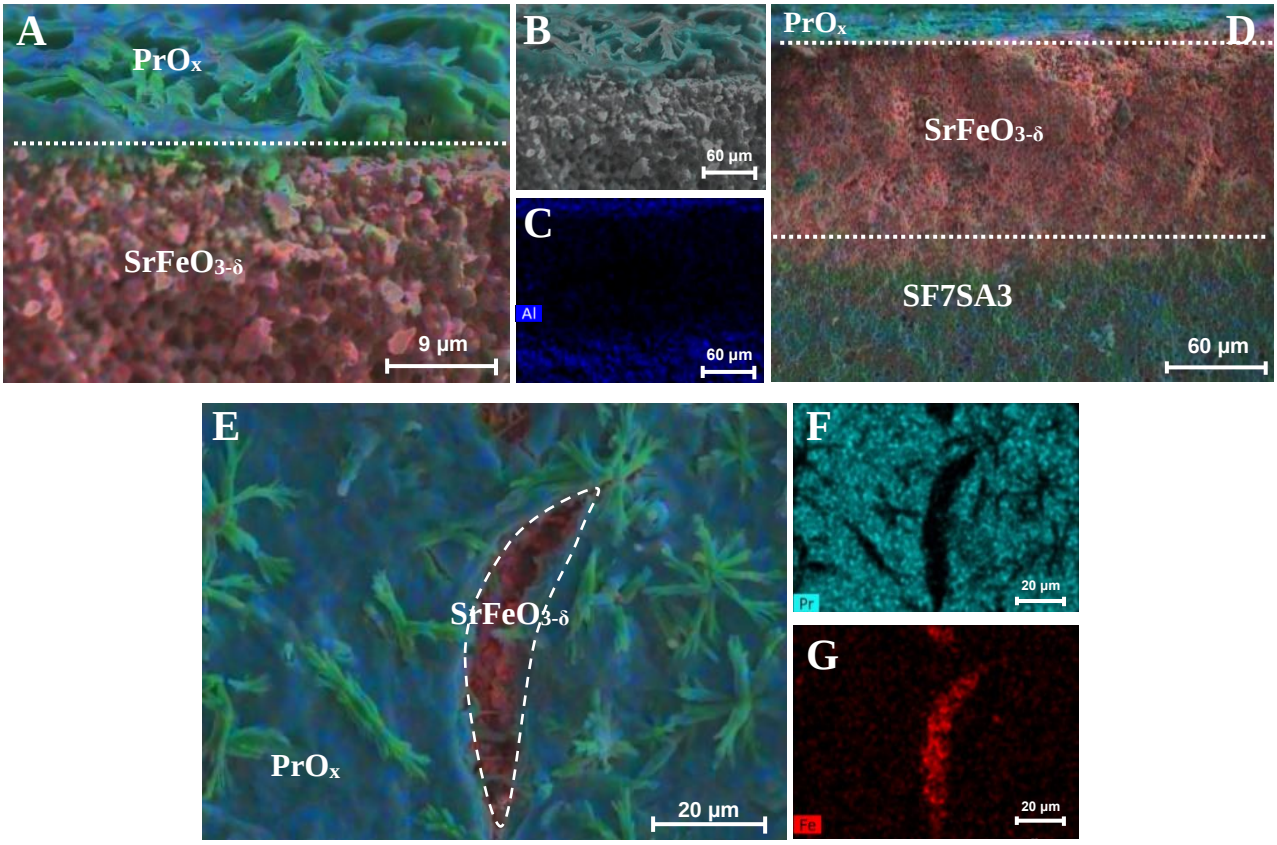

Figure 53 - SEM micrographs of SF7SA3 membrane after hydrothermal treatment with $Pr(NO_3)_3.9H_2O$ + NaOH at a temperature of 120ºC for 24 hours: (A-D) Cross-section of EDS maps showing the distribution of various elements, (E-G) Surface view of EDS maps showing the distribution of various elements.

The etching with NaOH again results in the formation of the porous $SrFeO_{3-\delta}$ layer due to aluminium etching. Simultaneously, the formation of PrO_x takes place at the surface, together with partial enrichment with strontium, for the reasons discussed in Section 3.2.2. The formed PrO_x layer appears to have good adhesion to the etched layer of $SrFeO_{3-\delta}$, which is expected to improve its durability and minimize the boundary resistance to ionic transport. Following the hydrothermal modification, thermal post-treatment was further applied.

Figure 54. (B, E, N, O) shows the microstructural evolution and drastic morphology changes after annealing at 900 ºC of the surface, highlighting the formation of the porous PrO_x layer. In general, besides some cracks, this layer presents some nanostructuring, favourable for surface activation. The pores are formed by the thermal decomposition of $Pr(OH)_3$ formed during hydrothermal processing and presumably having more dense structure (Figure 54). This outer layer contains a significant percentage of PrO_x (Figure 54 (A, F, G)) as suggested by the XRD results (Figure 55).

The analysis of the surface was performed in different areas of the membrane, and the presence of PrO_x layer was always detected. However, this layer it's not entirely uniform, due to the existence of two additional processes, the etching of the membrane and the growth of $SrCO_3$ blocks in the same places where the PrO_x layer is deposited (Figure 54. (B-D, G)). No significant diffusion into the bulk of SF7SA3 was observed (Figure 54. (P, T)).

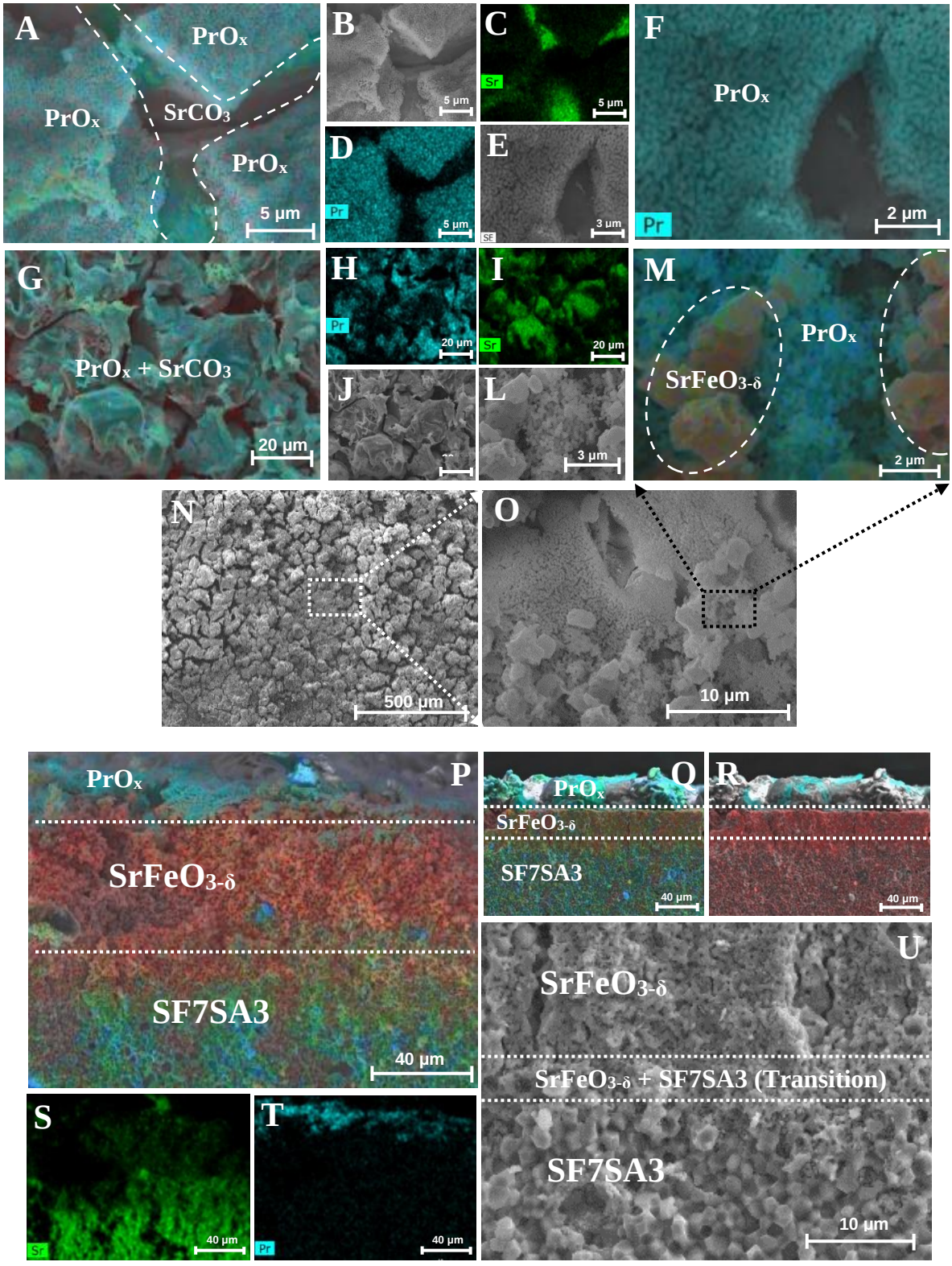

Figure 54 - SEM micrographs of SF7SA3 membrane after hydrothermal treatment with $Pr(NO_3)_3.9H_2O$ + NaOH at a temperature of 120 ºC for 24 hours followed by an annealing of 900 ºC: (A, C-D, F-I, M, P-T) Surface view of EDS maps showing the

distribution of various elements, (B, E, J-L, N-O) Surface view (SEM), (U) Cross-section (SEM).

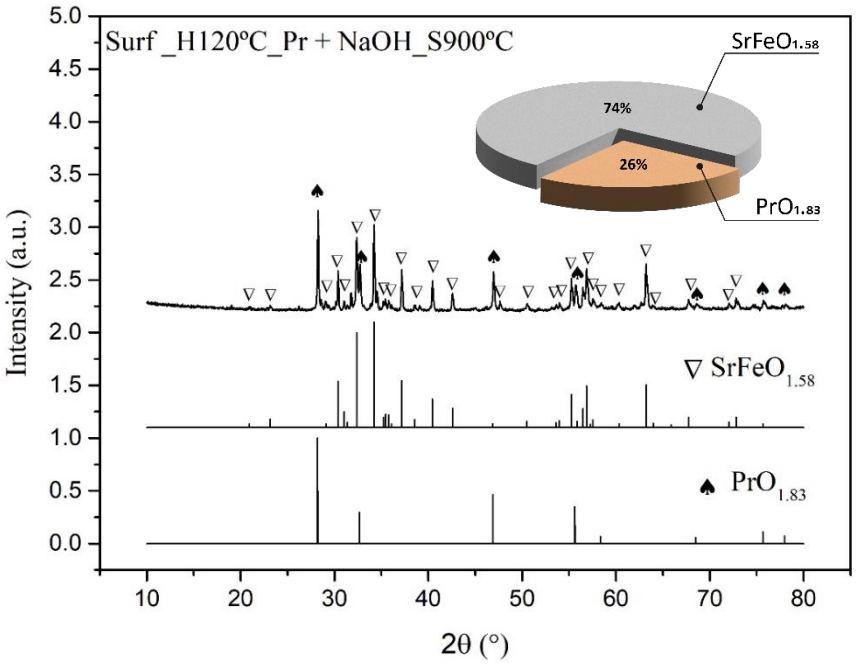

Figure 55 - XRD pattern of SF7SA surface and respective phases after hydrothermal treatment with $Pr(NO_3)_3.9H_2O$ + NaOH at a temperature of 120ºC for 24 hours followed by an annealing of 900 ºC.

Figure 56 shows more general micrographs of the cross-section of bulk SF7SA3 membrane after hydrothermal treatment at 120ºC, using NaOH and $Pr(NO_3)_3$. It should be noticed that, in the hydrothermal reactor, the membrane surfaces were not exposed in the same way to the medium. The membrane was placed over a zirconia ring. In such configuration, the membrane surface opposite to zirconia ring, was better exposed to the hydrothermal solution, also implying a faster diffusion of the species formed by different reactions. Accordingly, the surface in contact with the zirconia ring, was exposed to a rather static part of the solution.

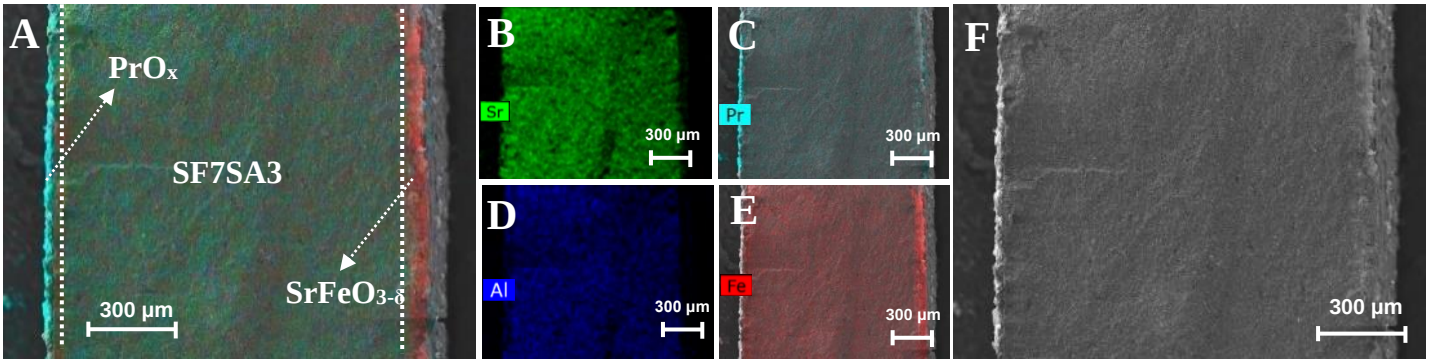

Figure 56 - SEM micrographs of fractured cross-section SF7SA3 bulk membrane after hydrothermal treatment with $Pr(NO_3)_3.9H_2O$ + NaOH at a temperature of 120ºC for 24 hours followed by an annealing of 650ºC: (A-E) Cross-section of EDS maps showing the distribution of various elements, (F) Cross-section (SEM).

According to Figure 57, more PrO_x is formed at the surface better exposed to the solution (left), while etching and formation of $SrFeO_{3-\delta}$ is more pronounced at the opposite side. It is possible to assume that the deposition of PrO_x blocks the surface towards the diffusion of alkaline medium, preventing excessive etching. On the contrary, less massive PrO_x formation on the opposite side allows etching to proceed deeper in the bulk. It should be noticed that both scenarios are expected to promote the surface oxygen exchange. Such a mixed activation mechanism, with a possibility to control the rate of each contributing process, might be useful for different activation of the feed and permeate sides of the membrane, where the surface exchange rate is affected by different oxygen partial pressure / atmosphere conditions.

This upper side layer of PrO_x was verified by the spectra of Figure 57. The spectra detected on this surface Pr species in high quantities while on the bulk material only elements of SF7SA3 were detected.

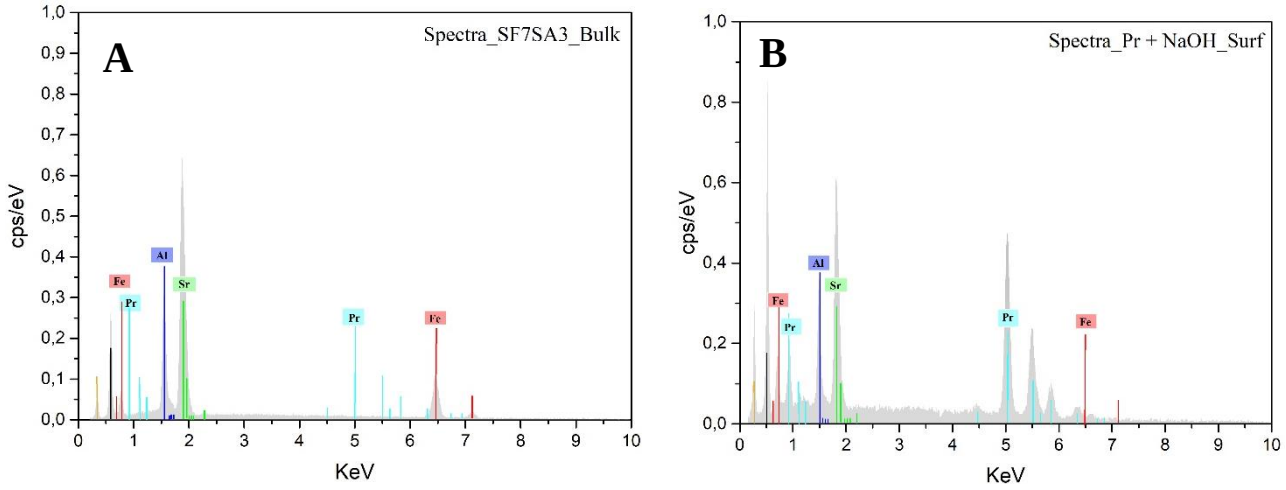

Figure 57 - EDS spectrum: Bulk material (A); Activation layer (B).

An increase of the temperature of hydrothermal processing up to 150ºC was also attempted but this resulted in less PrO_x deposition and more excessive etching with the formation of $SrFeO_{3-\delta}$ and surface enrichment with Sr (Figure 58. (A1, D1)).

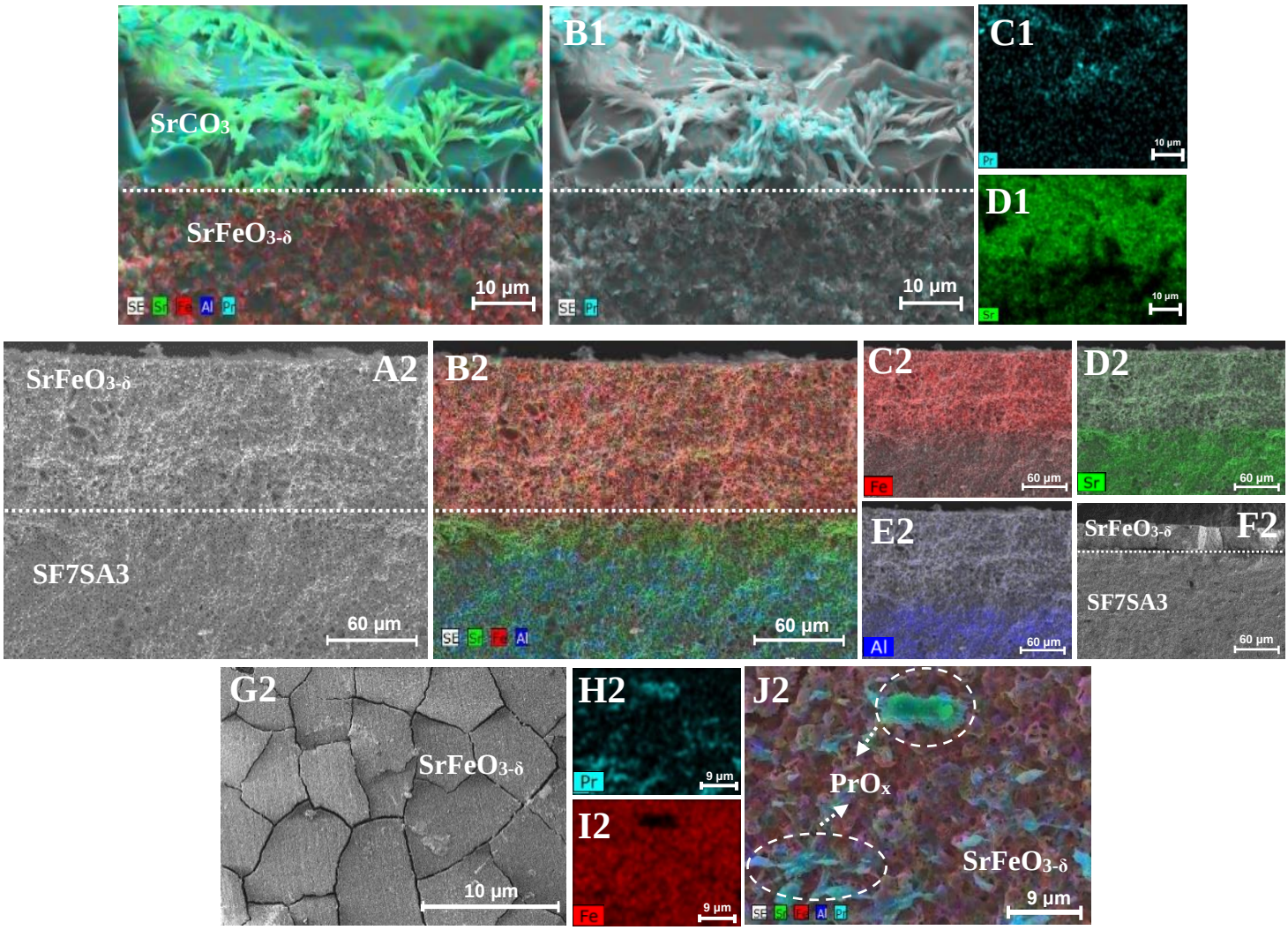

Figure 58 - SEM micrographs of SF7SA3 membrane after hydrothermal treatment with $Pr(NO_3)_3.9H_2O$ + NaOH at a temperature of (1) 150 ºC for 24 hours; (2) 100 ºC for 24 hours followed by an annealing of 900 ºC: (A1-D1, A2-E2) Cross-section of EDS maps showing the distribution of various elements, (F2) Cross-section (SEM), (G2) Surface view (SEM), (H2-I2) Surface view of EDS maps showing the distribution of various elements.

Lower hydrothermal processing temperature (100 ºC) was also tested, again resulting in a poor PrO_x modification. At the same time, the etching proceeded without the excessive formation of Sr-containing species at the surface. In fact, this result might be considered as a good iteration to reconsider the temperatures used for the simple top-down type approach (section 3.2.2.). However, many surface cracks were also observed in this case; the reasons for this are not well-understood. In general, the obtained results suggest that the microstructures promising for surface activation can be successfully achieved in different ways. However, each approach requires careful optimisation of the

processing conditions to maximize its output, which goes beyond the scope of this thesis. Another limitation is that, ideally, while testing each particular scenario for hydrothermal processing, the results must be immediately complemented by the oxygen permeation studies. However, this requires significant experimental efforts and re-focusing of the work, and results in delays in testing other parallel approaches. Therefore, in the present work, the modified membranes for oxygen permeation test were selected based on the microstructural observations and logics described above, without using auxiliary oxygen permeation results driving the research on finding optimal hydrothermal conditions.

3.3. Oxygen Permeation Studies

Figure 59 shows temperature dependences of the oxygen permeation through SF7SA3 hydrothermal modified membranes under fixed oxygen partial pressure gradients across the membrane and respective activation energies. For a better understanding of each applied treatment, Table 4 shows a description of the studied modified SF7SA3 membranes.

Table 4 - Description of the membranes used for oxygen permeation studies.

Notation	Description
Non-Modified	Non-modified SF7SA3 membrane
HT - NaOH	Hydrothermal treatment with 1M NaOH at a temperature of 150ºC for 24 hours.
HT – AA	Hydrothermal treatment with 1M NaOH at a temperature of 150ºC for 24 hours followed by an annealing of 650ºC with a posterior acetic acid treatment at the surface.
HT – MT	Hydrothermal treatment with 1M NaOH at a temperature of 150ºC for 24 hours followed by an annealing of 650ºC with a posterior mechanical removal of $SrCO_3$ layer.
HT - Pr	Hydrothermal treatment with $Pr(NO_3)_3.9H_2O$ + NaOH at a temperature of 120 ºC for 24 hours followed by an annealing of 900 ºC.

The results shown in Figure 59, unambiguously demonstrate that the first proof-of-concept for hydrothermal modification of oxygen membranes was achieved. All membranes subjected to various modifications of the hydrothermal treatment exhibit higher oxygen permeation fluxes than the non-modified membrane. The highest values were observed for the membrane with the surface cleaned by the mechanical removal of $SrCO_3$ species. On the contrary, HT-NaOH, HT-AA and HT-Pe membranes show quite similar values of the oxygen permeation fluxes. The latter suggest that in these three types of membranes, the surface blocking with $SrCO_3$ is still considerable. However, this blocking appears to be not the only limiting factor. As compared to HT-NaOH and HT-Pr membranes, the surface of HT-AA membranes contains much fewer $SrCO_3$ species, as evidenced by previous microstructural studies (Figure 46). Thus, one might expect the oxygen permeation fluxes through this membrane to be close to HT-MT, which is not the

observed case. Thus, the presence of additional surface blocking effects by species, subsequently removed by mechanical action in the case of HT-MT membrane, might be expected. The mechanical cleaning might also remove part of the etched $SrFeO_{3-\delta}$ surface layer, decreasing its thickness and possible effects related to the diffusion of oxygen in the pores.

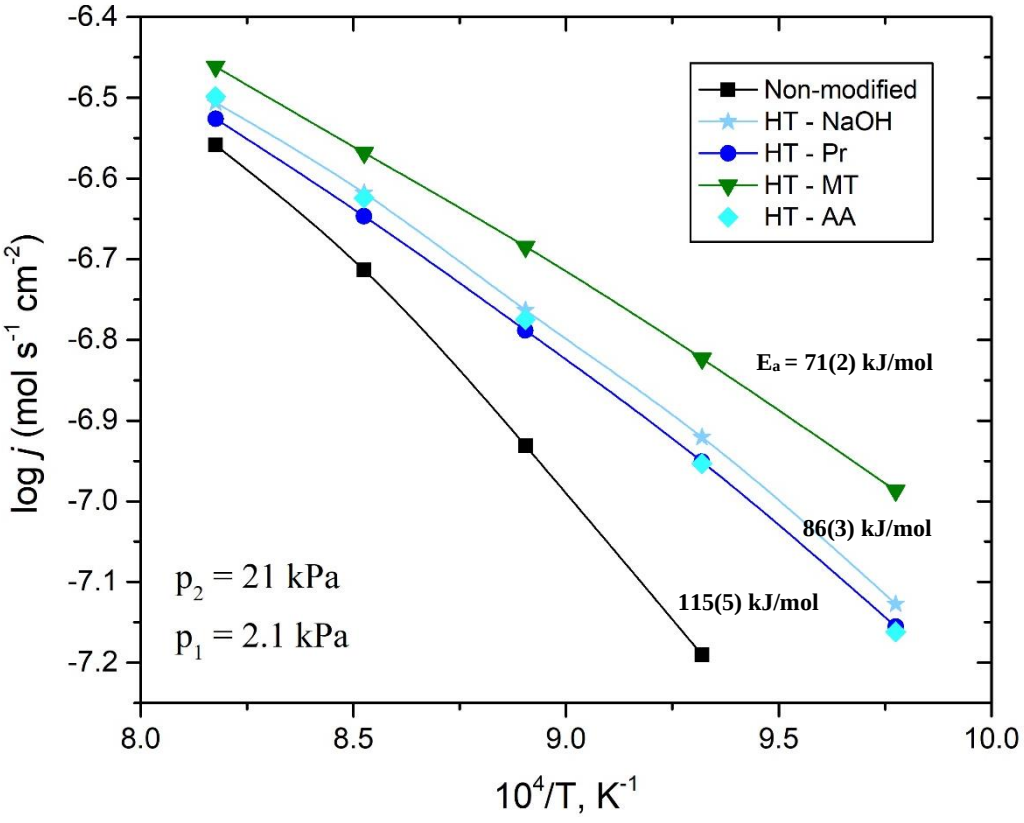

Figure 59 - Temperature dependence of the oxygen permeation through SF7SA3 hydrothermal modified membranes under fixed oxygen partial pressure gradients and respective activation energies.

The activation energies (E_a) of oxygen permeation were calculated using the Arrhenius equation:

$$j \times T = A_0 \times e^{\frac{-E_a}{RT}} \quad (19)$$

where A_0 is the pre-exponential factor and R is the universal gas constant. For E_a calculation, the equation was linearized by using logarithms.

The highest activation energy was found for non-modified membrane, while other hydrothermally-modified membranes showed lower E_a values. It is generally accepted that the activation energy of the surface exchange is typically higher than for bulk oxygen diffusion because the dissociation of oxygen molecules to form oxygen ions requires more energy than the oxygen diffusion through oxygen vacancies in the lattice. Thus, the observed results clearly confirm that the hydrothermal treatment results in surface activation of the SF7SA3 membranes towards oxygen exchange, accompanied by a decrease in E_a values, as shown in Figure 59.

In order to illustrate the dependence of oxygen permeation fluxes on the oxygen partial pressure drop, the *j* values were averaged for HT-AA, HT-Pr and HT-NaOH, showing quite similar permeation. The results are shown in Figure 60.

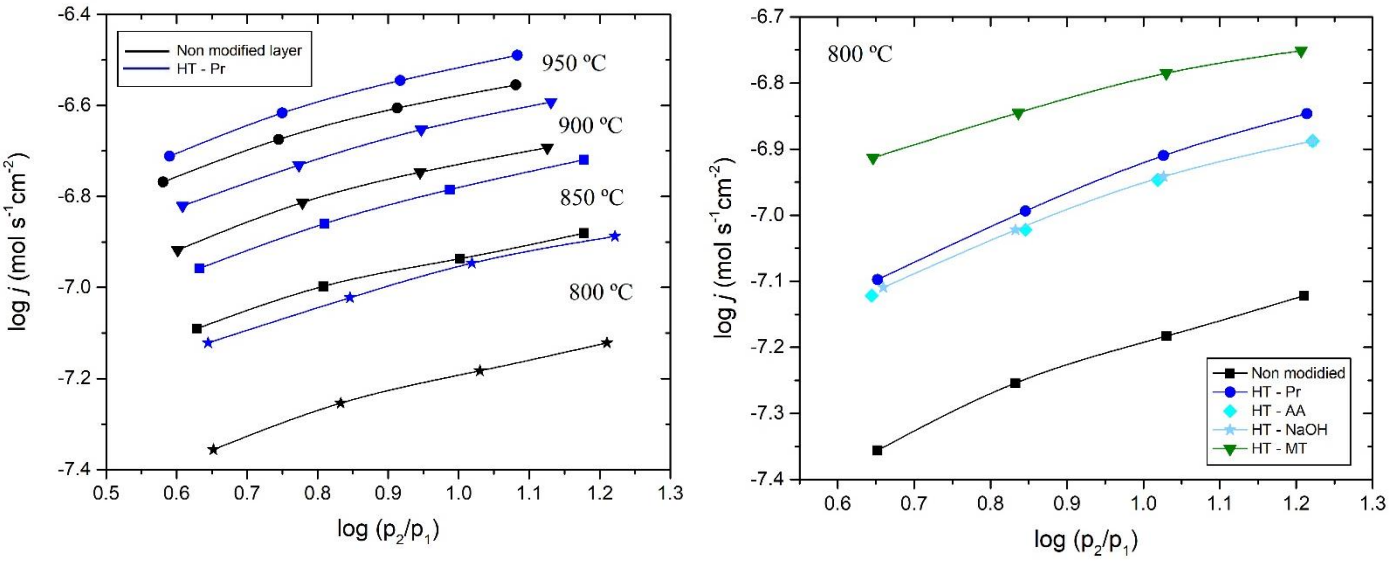

Figure 60 - Temperature dependence of the oxygen permeation through SF7SA3 hydrothermal modified membranes under fixed oxygen partial pressure gradients and respective activation energies.

It is again seen that oxygen permeation rate increases with temperature, due to thermal activation mechanism for both bulk diffusion and surface oxygen exchange. The difference between the oxygen permeation fluxes through non-modified and hydrothermally-modified membranes is progressively increasing on lowering the temperature, due to increasing role of the surface exchange. At 800 °C, the oxygen permeation fluxes through hydrothermally-activated membranes are ~1.7 times higher

than for non-modified one. The latter indicated that the proposed hydrothermal activation strategies are promising for increasing the performance of MIEC membranes. Further potential and large room for the improvements as demonstrated by even higher performance of the HT-MT membrane, also suggesting that the surface modification procedures obviously require further optimisation.

It should be noticed that the results presented in this Section, which basically include 5 samples, were obtained after long optimisation of the oxygen permeation measurement procedure, including reliable and gas-tight glass sealing. To obtain these results, around 30 measurement tests were done, with most of them showing non-reliable results due to glass cracking, partial interaction of the glass with the ceramic membrane material and even fracturing of zirconia tube in measuring cell, due to high mechanical strength and different thermal and chemical expansion behaviour of the tested SF7SA3 membrane.

3.4. Conclusions

- SF7SA3 composite was successfully synthesized by using glycine-nitrate route and corresponding dense ceramic membranes suitable for oxygen permeation studies were prepared.

- Additional characterisation of the phase composition, microstructure, electrical conductivity, and thermal and chemical expansion have been performed, confirming the composite microstructure with residual porosity and expected electrical transport and thermomechanical behaviour.

- Different top-down type and bottom-up type approaches for hydrothermal modification of SF7SA3 membrane were attempted, including etching in alkaline conditions, followed by additional acid or mechanical treatments, and deposition of PrO_x layer, possessing high catalytic activities in the processes involving oxygen.

- Detailed microstructural studies of the ceramic membranes after hydrothermal modification have confirmed the presence of desired effects, namely, the formation of etched porous $SrFeO_{3-\delta}$ layer at the surface and deposition of praseodymium oxide. However, these studies also pointed out the simultaneous formation of additional species (e.g., $SrCO_3$), decreasing the active surface area and blocking oxygen surface exchange process.

- The comparative studies of oxygen permeation through non-modified and modified membranes have provided a convincing proof-of-concept for proposed strategies of hydrothermal activation of ceramic MIEC membranes. In all cases, the modified membranes showed superior oxygen fluxes as compared to the reference. The calculated values of activation energies unambiguously confirm that this improvement was achieved due to the surface activation.

- The oxygen permeation results obtained for the membrane subjected to delicate surface cleaning to remove the surface blocking species suggest great further prospects for the proposed approach.

- Future work, in the first place, should consider the long-term tests of the modified membranes in order to reveal and circumvent any degradation effects, which might be

related to the coarsening of the surface microstructure. Detailed post-mortem structural and microstructural studies are also required.

References

[1] Julio García Fayos, “Development of Ceramic Miec Membranes for Oxygen Separation : Application in catalytic industrial processes,” Universitat Politécnica de Valéncia, 2017.

[2] S. Gupta, M. K. Mahapatra, and P. Singh, “Lanthanum chromite based perovskites for oxygen transport membrane,” *Mater. Sci. Eng. R Reports*, vol. 90, pp. 1–36, 2015, doi: 10.1016/j.mser.2015.01.001.

[3] A. Note, “Process oxygen - air separation applications,” 2006.

[4] BetaEQ, “Obtenção de oxigénio através do processo criogénico,” 2019. https://betaeq.com.br/index.php/2019/10/29/obtencão-de-oxigénio-através-do-processo-criogénico/.

[5] S. S. Hashim, A. R. Mohamed, and S. Bhatia, “Oxygen separation from air using ceramic-based membrane technology for sustainable fuel production and power generation,” *Renew. Sustain. Energy Rev.*, vol. 15, no. 2, pp. 1284–1293, 2011, doi: 10.1016/j.rser.2010.10.002.

[6] P. M. Geffroy, E. Blond, N. Richet, and T. Chartier, “Understanding and identifying the oxygen transport mechanisms through a mixed-conductor membrane,” *Chem. Eng. Sci.*, vol. 162, pp. 245–261, 2017, doi: 10.1016/j.ces.2017.01.006.

[7] Q. Jiang, S. Faraji, D. A. Slade, and S. M. Stagg-Williams, *A Review of Mixed Ionic and Electronic Conducting Ceramic Membranes as Oxygen Sources for High-Temperature Reactors*, 1st ed., vol. 14, no. 1. Elsevier B.V., 2011.

[8] X. Zhu and W. Yang, *Mixed Conducting Ceramic Membranes, Fundamentals, Materials and Applications*, 1st ed. Springer, 2017.

[9] J. Sunarso *et al.*, “Mixed ionic-electronic conducting (MIEC) ceramic-based membranes for oxygen separation,” *J. Memb. Sci.*, vol. 320, no. 1–2, pp. 13–41, 2008, doi: 10.1016/j.memsci.2008.03.074.

[10] Y. Liu, X. Tan, and K. Li, “Mixed conducting ceramics for catalytic membrane processing,” *Catal. Rev. - Sci. Eng.*, vol. 48, no. 2, pp. 145–198, 2006, doi: 10.1080/01614940600631348.

[11] K. Zhang *et al.*, “Research progress and materials selection guidelines on mixed conducting perovskite-type ceramic membranes for oxygen production,” *RSC Adv.*, vol. 1, no. 9, pp. 1661–1676, 2011, doi: 10.1039/c1ra00419k.

[12] A. A. Plazaola *et al.*, “Mixed ionic-electronic conducting membranes (MIEC) for their application in membrane reactors: A review,” *Processes*, vol. 7, no. 3, 2019, doi: 10.3390/pr7030128.

[13] P. M. Geffroy, J. Fouletier, N. Richet, and T. Chartier, “Rational selection of MIEC materials in energy production processes,” *Chem. Eng. Sci.*, vol. 87, pp. 408–433, 2013, doi: 10.1016/j.ces.2012.10.027.

[14] C. Li, J. J. Chew, A. Mahmoud, S. Liu, and J. Sunarso, “Modelling of oxygen transport through mixed ionic-electronic conducting (MIEC) ceramic-based membranes: An overview,” *J. Memb. Sci.*, vol. 567, no. May, pp. 228–260, 2018, doi: 10.1016/j.memsci.2018.09.016.

[15] H. J. M. Bouwmeester, “Dense ceramic membranes for methane conversion,” *Catal. Today*, vol. 82, no. 1–4, pp. 141–150, 2003, doi: 10.1016/S0920-5861(03)00222-0.

[16] R. H. Sampieri, *“Inorganic Membranes for Energy and Environmental Applications,”* 1st ed. New York, NY: Springer New York, 2009.

[17] X. Tan, N. Liu, B. Meng, J. Sunarso, K. Zhang, and S. Liu, “Oxygen permeation behavior of $La_{0.6}Sr_{0.4}Co_{0.8}Fe_{0.2}O_3$ hollow fibre membranes with highly concentrated CO_2 exposure,” *J. Memb. Sci.*, vol. 389, pp. 216–222, 2012, doi: 10.1016/j.memsci.2011.10.032.

[18] P. J. Gellings, H. J. M. Bouwmeester, F. Shapiro, D. C. Prepress, K. Luong, and S. Schwartz, *The CRC Handbook of Solid State Electrochemistry Library of Congr ess Cataloging-in-Publication Data*. 1997.

[19] H. J. M. Bouwmeester, H. Kruidhof, and A. J. Burggraaf, “Importance of the surface exchange kinetics as rate limiting step in oxygen permeation through mixed-conducting oxides,” *Solid State Ionics*, vol. 72, pp. 185–194, 1994, doi: 10.1016/0167-2738(94)90145-7.

[20] B. C. H. Steele, “Oxygen ion conductors and their technological applications,”

Mater. Sci. Eng. B, vol. 13, no. 2, pp. 79–87, 1992, doi: 10.1016/0921-5107(92)90146-Z.

[21] F. A. Kröger and H. J. Vink, "Relations between the Concentrations of Imperfections in Crystalline Solids," *Solid State Phys. - Adv. Res. Appl.*, vol. 3, pp. 307–435, 1956, doi: 10.1016/S0081-1947(08)60135-6.

[22] A. Shaula, "Novel Iron-Containing Materials with Fast Oxygen Ionic Transport," Universidade de Aveiro, 2006.

[23] S. Aasland, I. L. Tangen, and K. Wiik, "Oxygen permeation of $SrFe_{0.67}Co_{0.3}O_{3-d}$," *Solid State Ionics*, vol. 135, pp. 713–717, 2000, doi: 10.1016/S0167-2738(00)00389-1.

[24] H. J. M. Bouwmeester and A. J. Burggraaf, "Dense ceramic membranes for oxygen separation," *Membr. Sci. Technol.*, vol. 4, no. 10, pp. 435–528, 1996, doi: 10.1016/S0927-5193(96)80013-1.

[25] J. E. ten Elshof, H. J. M. Bouwmeester, and H. Verweij, "Oxidative coupling of methane in a mixed-conducting perovskite membrane reactor," *Appl. Catal. A, Gen.*, vol. 130, no. 2, pp. 195–212, 1995, doi: 10.1016/0926-860X(95)00098-4.

[26] M. Nilsson, "Solar-driven Hydrogen Production by the use of MIEC Membranes – A Techno-Economic Assessment," KTH School of Industrial Engineering and Management, 2012.

[27] Z. Wang, H. Liu, X. Tan, Y. Jin, and S. Liu, "Improvement of the oxygen permeation through perovskite hollow fibre membranes by surface acid-modification," *J. Memb. Sci.*, vol. 345, no. 1–2, pp. 65–73, 2009, doi: 10.1016/j.memsci.2009.08.024.

[28] F. M. Figueiredo, V. V. Kharton, A. P. Viskup, and J. R. Frade, "Surface enhanced oxygen permeation in $CaTi_{1-x}Fe_xO_{3-\delta}$ ceramic membranes," *J. Memb. Sci.*, vol. 236, no. 1–2, pp. 73–80, 2004, doi: 10.1016/j.memsci.2004.02.008.

[29] M. Riaz and M. Abdullah Butt, "Oxygen Transport Membranes and their Role in CO_2 Capture and Syngas Production," *J. Membr. Sci. Technol.*, vol. 08, no. 02, pp. 2–9, 2018, doi: 10.4172/2155-9589.1000181.

[30] Q. Jiang, K. J. Nordheden, and S. M. Stagg-Williams, "Oxygen permeation study

and improvement of $Ba_{0.5}Sr_{0.5}Co_{0.8}Fe_{0.2}O_x$ perovskite ceramic membranes," *J. Memb. Sci.*, vol. 369, no. 1–2, pp. 174–181, 2011, doi: 10.1016/j.memsci.2010.11.073.

[31] A. V. Kovalevsky, V. V. Kharton, F. Maxim, A. L. Shaula, and J. R. Frade, "Processing and characterization of $La_{0.5}Sr_{0.5}FeO_3$-supported $Sr_{1-x}Fe(Al)O_3$-$SrAl_2O_4$ composite membranes," *J. Memb. Sci.*, vol. 278, no. 1–2, pp. 162–172, 2006, doi: 10.1016/j.memsci.2005.10.052.

[32] X. Y. Wu and A. F. Ghoniem, "Mixed ionic-electronic conducting (MIEC) membranes for thermochemical reduction of CO_2: A review," *Prog. Energy Combust. Sci.*, vol. 74, pp. 1–30, 2019, doi: 10.1016/j.pecs.2019.04.003.

[33] S. Baumann, J. M. Serra, M. P. Lobera, S. Escolástico, F. Schulze-Küppers, and W. A. Meulenberg, "Ultrahigh oxygen permeation flux through supported $Ba_{0.5}Sr_{0.5}Co_{0.8}Fe_{0.2}O_{3-\delta}$ membranes," *J. Memb. Sci.*, vol. 377, no. 1–2, pp. 198–205, 2011, doi: 10.1016/j.memsci.2011.04.050.

[34] P. Lemes-Rachadel, G. S. Garcia, R. A. F. Machado, D. Hotza, and J. C. D. Da Costa, "Current developments of mixed conducting membranes on porous substrates," *Mater. Res.*, vol. 17, no. 1, pp. 242–249, 2014, doi: 10.1590/S1516-14392013005000175.

[35] A. S. Bhalla, R. Guo, and R. Roy, "The perovskite structure - A review of its role in ceramic science and technology," *Mater. Res. Innov.*, vol. 4, no. 1, pp. 3–26, 2000, doi: 10.1007/s100190000062.

[36] G. Sachinelli, "Desenvolvimento de membranas cerâmicas mistas do sistema BSCF para separação de oxigénio," Universidade Federal de Santa Catarina, 2013.

[37] Q. Ji, L. Bi, J. Zhang, H. Cao, and X. S. Zhao, "The role of oxygen vacancies of ABO_3 perovskite oxides in the oxygen reduction reaction," *Energy Environ. Sci.*, vol. 13, no. 5, pp. 1408–1428, 2020, doi: 10.1039/d0ee00092b.

[38] G. Sachinelli, P. Lemes, R. Antonio, F. Machado, and D. Hotza, "Membranas de condução mista iónica e eletrónica (MIEC): Composições, preparação e desempenho," vol. 37, no. 2, pp. 302–307, 2014, doi: 10.5935/0100-4042.20140051.

[39] S. Engels, T. Markus, M. Modigell, and L. Singheiser, “Oxygen permeation and stability investigations on MIEC membrane materials under operating conditions for power plant processes,” *J. Memb. Sci.*, vol. 370, no. 1–2, pp. 58–69, 2011, doi: 10.1016/j.memsci.2010.12.021.

[40] W. T. Mujeeb Khan, Muhammed Nawaz Tahir, Syed Farooq Adil, Hadayat Ullah Khan, M. Rafiq H. Siddiqui, Abdulrahman A. Al-warthan, “High-temperature characterization of oxygen-deficient K_2NiF_4-Type $Nd_{2-x}Sr_xNiO_{4-\delta}$ (x = 1.0-1.6) for potential SOFC/SOEC Applications,” *J. Mater. Chem. A*, p. 121, 2015, doi: 10.1039/c7ta07529d.

[41] T. Shimura, K. Suzuki, and H. Iwahara, “High temperature protonic conduction in Sr_2TiO_4-based ceramics with K_2NiF_4-type structure,” *Solid State Ionics*, vol. 104, no. 1–2, pp. 79–88, 1997, doi: 10.1016/s0167-2738(97)00394-9.

[42] E. Kravchenko *et al.*, “Impact of Oxygen Deficiency on the Electrochemical Performance of K_2NiF_4-Type $(La_{1-x}Sr_x)_2NiO_{4-\delta}$ Oxygen Electrodes,” *ChemSusChem*, vol. 10, no. 3, pp. 600–611, 2017, doi: 10.1002/cssc.201601340.

[43] H. Mao, Y. Wei, H. Gui, X. Li, Z. Zhao, and W. Xie, “First-principle investigations of K_2NiF_4-type double perovskite oxides $La_4B'B''O_8$ (B′B″ = Fe, Co, Ni),” *J. Appl. Phys.*, vol. 115, no. 21, 2014, doi: 10.1063/1.4881459.

[44] M. Mogensen, D. Lybye, N. Bonanos, P. V. Hendriksen, and F. W. Poulsen, “Factors controlling the oxide ion conductivity of fluorite and perovskite structured oxides,” *Solid State Ionics*, vol. 174, no. 1–4, pp. 279–286, 2004, doi: 10.1016/j.ssi.2004.07.036.

[45] D. Marrocchelli, P. A. Madden, S. T. Norberg, and S. Hull, “Cation composition effects on oxide conductivity in the $Zr_2Y_2O_7$-Y_3NbO_7 system,” *J. Phys. Condens. Matter*, vol. 21, no. 40, pp. 1–22, 2009, doi: 10.1088/0953-8984/21/40/405403.

[46] S. T. Norberg, I. Ahmed, S. Hull, D. Marrocchelli, and P. A. Madden, “Local structure and ionic conductivity in the $Zr_2Y_2O_7$-Y_3NbO_7 system,” *J. Phys. Condens. Matter*, vol. 21, no. 21, 2009, doi: 10.1088/0953-8984/21/21/215401.

[47] V. V. Kharton *et al.*, “Oxygen transport in $Ce_{0.8}Gd_{0.2}O_{2-\delta}$ -based composite membranes,” *Solid State Ionics*, vol. 160, no. 3–4, pp. 247–258, 2003, doi: 10.1016/S0167-2738(03)00183-8.

[48] V. P. Junior, P. L. Rachadel, M. N. Quadri, D. Hotza, and S. Y. G. González, "Enhanced LSCF oxygen deficiency through hydrothermal synthesis," *Ceram. Int.*, vol. 44, no. 17, pp. 20671–20676, 2018, doi: 10.1016/j.ceramint.2018.08.060.

[49] M. Yoshimura and K. Byrappa, "Hydrothermal processing of materials: Past, present and future," *J. Mater. Sci.*, vol. 43, no. 7, pp. 2085–2103, 2008, doi: 10.1007/s10853-007-1853-x.

[50] G. Canu and V. Buscaglia, "Hydrothermal synthesis of strontium titanate: Thermodynamic considerations, morphology control and crystallisation mechanisms," *CrystEngComm*, vol. 19, no. 28, pp. 3867–3891, 2017, doi: 10.1039/c7ce00834a.

[51] H. Herrmann and H. Bucksch, "Hydrothermal Process," *Dict. Geotech. Eng. Geotech.*, no. 1, pp. 706–706, 2014, doi: 10.1007/978-3-642-41714-6_82100.

[52] M. Diez-Garcia, J. J. Gaitero, J. S. Dolado, and C. Aymonier, "Ultra-Fast Supercritical Hydrothermal Synthesis of Tobermorite under Thermodynamically Metastable Conditions," *Angew. Chemie - Int. Ed.*, vol. 56, no. 12, pp. 3162–3167, 2017, doi: 10.1002/anie.201611858.

[53] Q. Yang *et al.*, "Metal oxide and hydroxide nanoarrays: Hydrothermal synthesis and applications as supercapacitors and nanocatalysts," *Prog. Nat. Sci. Mater. Int.*, vol. 23, no. 4, pp. 351–366, 2013, doi: 10.1016/j.pnsc.2013.06.015.

[54] V. V. Kharton *et al.*, "Processing, stability and oxygen permeability of Sr(Fe, Al)O_3-based ceramic membranes," *J. Memb. Sci.*, vol. 252, no. 1–2, pp. 215–225, 2005, doi: 10.1016/j.memsci.2004.12.018.

[55] A. V. Kovalevsky *et al.*, "Oxygen permeability and stability of asymmetric multilayer $Ba_{0.5}Sr_{0.5}Co_{0.8}Fe_{0.2}O_{3-\delta}$ ceramic membranes," *Solid State Ionics*, vol. 192, no. 1, pp. 677–681, 2011, doi: 10.1016/j.ssi.2010.05.030.

[56] C. Santos, "Membranas de Separação de CO2," Universidade de Aveiro, 2013.

[57] R. Wang *et al.*, "Experimental validation of solid oxide fuel cell polarization modeling: An LSM-YSZ/YSZ/Ni-YSZ case study," *Electrochim. Acta*, vol. 361, p. 137052, 2020, doi: 10.1016/j.electacta.2020.137052.

[58] A. A. Yaremchenko *et al.*, “Ion Transport and Thermomechanical Properties of $SrFe(Al)O_{3-\delta}$–$SrAl_2O_4$ Composite Membranes,” *J. Electrochem. Soc.*, vol. 153, no. 6, p. J50, 2006, doi: 10.1149/1.2194668.

[59] A. A. Yaremchenko, V. V. Kharton, A. A. Valente, A. L. Shaula, F. M. B. Marques, and J. Rocha, “Mixed conductivity and electrocatalytic performance of $SrFeO_{3-\delta}$-$SrAl_2O_4$ composite membranes,” *Solid State Ionics*, vol. 177, no. 26–32, pp. 2285–2289, 2006, doi: 10.1016/j.ssi.2006.03.039.

[60] V. V. Kharton *et al.*, “Oxygen transport and thermomechanical properties of $SrFe(Al)O_{3-\delta}$-$SrAl_2O_4$ composites: Microstructural effects,” *J. Solid State Electrochem.*, vol. 10, no. 8, pp. 663–673, 2006, doi: 10.1007/s10008-006-0141-z.

[61] A. A. Yaremchenko, S. M. Mikhalev, E. S. Kravchenko, and J. R. Frade, “Thermochemical expansion of mixed-conducting $(Ba,Sr)Co_{0.8}Fe_{0.2}O_{3-\delta}$ ceramics,” *J. Eur. Ceram. Soc.*, vol. 34, no. 3, pp. 703–715, 2014, doi: 10.1016/j.jeurceramsoc.2013.09.012.

[62] M. V. Patrakeev *et al.*, “Oxygen nonstoichiometry and mixed conductivity of $SrFe_{1-x}M_xO_{3-\delta}$ (M=Al, Ga): Effects of B-site doping,” *Solid State Sci.*, vol. 8, no. 5, pp. 476–487, 2006, doi: 10.1016/j.solidstatesciences.2006.01.006.

[63] K. Cai *et al.*, “Geometrically Complex Silicon Carbide Structures Fabricated by Robocasting,” *J. Am. Ceram. Soc.*, vol. 95, no. 8, pp. 2660–2666, Aug. 2012, doi: 10.1111/j.1551-2916.2012.05276.x.

[64] X. Chen, J. Yu, and S. B. Adler, “Thermal and chemical expansion of Sr-doped lanthanum cobalt oxide ($La_{1-x}Sr_xCoO_{3-\delta}$),” *Chem. Mater.*, vol. 17, no. 17, pp. 4537–4546, 2005, doi: 10.1021/cm050905h.

[65] D. Marrocchelli, N. H. Perry, and S. R. Bishop, “Understanding chemical expansion in perovskite-structured oxides,” *Phys. Chem. Chem. Phys.*, vol. 17, no. 15, pp. 10028–10039, 2015, doi: 10.1039/c4cp05885b.

[66] D. Marrocchelli, S. R. Bishop, H. L. Tuller, and B. Yildiz, “Understanding chemical expansion in non-stoichiometric oxides: Ceria and zirconia case studies,” *Adv. Funct. Mater.*, vol. 22, no. 9, pp. 1958–1965, 2012, doi: 10.1002/adfm.201102648.

[67] A. V. Kovalevsky *et al.*, “Processing and oxygen permeation studies of asymmetric multilayer $Ba_{0.5}Sr_{0.5}Co_{0.8}Fe_{0.2}O_{3-\delta}$ membranes,” *J. Memb. Sci.*, vol. 380, no. 1–2, pp. 68–80, 2011, doi: 10.1016/j.memsci.2011.06.034.

[68] K. V. Zakharchuk, A. A. Yaremchenko, and D. P. Fagg, “Electrical properties and thermal expansion of strontium aluminates,” *J. Alloys Compd.*, vol. 613, no. 3, pp. 232–237, 2014, doi: 10.1016/j.jallcom.2014.05.225.

[69] M. Pourbaix, H. Zhang, and A. Pourbaix, “Presentation of an Atlas of chemical and electrochemical equilibria in the presence of a gaseous phase,” *Mater. Sci. Forum*, vol. 251–254, pp. 143–148, 1997, doi: 10.4028/www.scientific.net/msf.251-254.143.

[70] A. Kovalevsky *et al.*, “Oxygen exchange-limited transport and surface activation of $Ba_{0.5}Sr_{0.5}Co_{0.8}Fe_{0.2}O_{3-\delta}$ capillary membranes,” *J. Memb. Sci.*, vol. 368, no. 1–2, pp. 223–232, 2011, doi: 10.1016/j.memsci.2010.11.034.

[71] J. G. Kang, B. K. Min, and Y. Sohn, “Physicochemical properties of praseodymium hydroxide and oxide nanorods,” *J. Alloys Compd.*, vol. 619, pp. 165–171, 2015, doi: 10.1016/j.jallcom.2014.09.059.